CRC/Transregio 39

"Production technologies for light metal and fiber reinforced composite based components with integrated piezoceramic sensors and actuators (PT-PIESA)"

5th Scientific Symposium

Proceedings

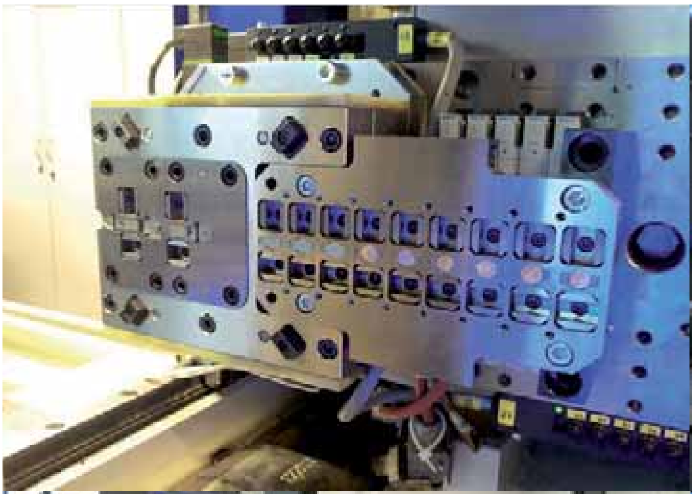

Lightweight Design by Integrating Functions

September 14 - 16, 2015
Dresden, Germany

Editor:
Prof. Dr.-Ing. Welf-Guntram Drossel

Funded by:
DFG

CRC/Transregio 39

„Production technologies for light metal and fiber reinforced composite based components with integrated piezoceramic sensors and actuators (PT-PIESA)“

5th Scientific Symposium

”Lightweight Design by Integrating Functions“

September 14 - 16, 2015
Dresden, Germany

Proceedings

Editor:

Prof. Dr.-Ing. Welf-Guntram Drossel

Funded by:

DFG

These proceedings contain the written version of the lectures of the 5th Scientific Symposium of the Collaborative Research Center/Transregio 39 PT-PIESA on September 14 - 16, 2015 in Dresden, Germany. The individual contributions of the event are published in these proceedings in the version provided by the authors without a change in content.

The organizers of the symposium thank the German Research Foundation (DFG) for its financial support of the Collaborative Research Center/Transregio 39 PT-PIESA.

Imprint

CRC/Transregio 39 - PT-PIESA

Speaker of the CRC/TR 39 PT-PIESA
Prof. Dr.-Ing. Welf-Guntram Drossel

Technische Universität Chemnitz
Mechanical Engineering
Institute for Machine Tools and Production Processes
Professorship for Adaptronics and Light-Weight Design
09107 Chemnitz
Germany

Phone: +49 (0)371 / 531-23560
Fax: +49 (0)371 / 531-23569
EMail adaptronik@mb.tu-chemnitz.de
http://www.tu-chemnitz.de/mb/adaptronik/

Managing Director of the CRC/TR 39 PT-PIESA

Technische Universität Chemnitz
Mechanical Engineering
Institute for Machine Tools and Production Processes
Professorship for Adaptronics and Light-Weight Design
09107 Chemnitz
Germany

Phone: +49 (0)371 / 531-23560
Fax: +49 (0)371 / 531-23569
Email: pt-piesa-gs@mb.tu-chemnitz.de
http://www.pt-piesa.tu-chemnitz.de

5th Scientific Symposium of the CRC/TR 39 PT-PIESA
Light-Weight Design by Function Integration

Fraunhofer IWU, Nöthnitzer Str. 44, 01187 Dresden, Germany
14th-16th September 2015
http://www.pt-piesa.tu-chemnitz.de/symposium/

Proceedings editor's names
Professor Welf-Guntram Drossel
Technische Universität Chemnitz
Mechanical Engineering Institute for Machine Tools and Production Processes
Professorship for Adaptronics and Light-Weight Design
09107 Chemnitz, Germany
http://www.tu-chemnitz.de/mb/adaptronik/
EMail adaptronik@mb.tu-chemnitz.de

Preface

Today, light-weight design is an implicit necessity and overriding goal in automotive engineering, electric mobility, machine tools, as well as for aerospace and large wind energy plants. It claims to design components and structures that are light, stiff, safe, and reliable at the same time. However, this leads to a multitude of technical and economic requirements which are inconsistent with one another. The research approach of the CRC/TR 39 is to solve the design conflict by using active light-weight structural components. The focus lies on the scientific fundamentals for the material integration of piezoceramics into high performance components of light-weight structures consisting of aluminum and polymer fiber composites.

Vision and incentive is the capability of mass production for active light-weight structural components, as this is required for the profitability of the process chain. The approach for solving this problem is to combine the hitherto separated production lines of passive component structures with the production lines of sensor-actuator modules. Hence, the material integration of piezoceramics takes place directly in the process of producing the components. Up to now, the functional bond between the mechanical component and the sensor-actuator module has been realized by joining processes or assembly techniques. This bonding is translocated to the inside of the active structural component during the production process.

Recent results are a knowledge base on design, semi-finished part production, function integration and characterization of active light-weight structural components. Precise solutions were implemented for connecting non-positive, form-closed, firmly bonded sensors and actuators consisting of piezoceramics as well as in situ characterization. The evidence of functionality of structural components with integrated sensors and actuators was provided by demonstrations. Thus, noise sensing and active noise reduction for example, was represented by different components. These components are comparable with typical structural automobile components regarding geometrical variety (radius of curvature), manufacturing process (forming, high-pressure die casting, fiber composite), and material (aluminum, fiber composite). A further goal consists in the explicit expansion of the range of applications of active light-weight structural components by improved functionality and capability of mass production. The functionality is to be reached by using new methods in design, integration, and characterization of piezoelectric converters as well as direct embedding of control electronics and evaluation electronics.

The 5th Scientific Symposium of the CRC/TR 39 is an open forum for the discussion between experts from the PT-PIESA projects and scientists from other institutions as well as experts from industry about recent research results.

Active fiber-reinforced thermoplastic composite components with embedded sensor-actuator arrays

Holeczek, K.; Starke, E.; Dannemann, M.; Modler, N.; Winkler, A.

Institute of Lightweight Engineering and Polymer Technology (ILK), Technische Universität Dresden, Holbeinstr. 3, 01307, Dresden, Germany

Abstract

The fiber- or textile-reinforced thermoplastics offer a high potential for the series production and simultaneously for the integration of additional functional elements. Using this property, a variety of smart functions like condition monitoring or measurement of the surrounding flow can be achieved. An open topic in successful application of smart functions is the assurance of the post-manufacturing position of the modules within the smart component. This problem becomes crucial, considering a module array where the position and orientation of the individual elements is essential for their correct operation. Within this paper an attempt is made to qualitatively characterize the relation between the deviation of position and angle of one of the transducers within the array and the ability to generate a directional wave. Herein, a three-dimensional parametrical model where the position and angle of one of the transducers are freely variable was developed and applied. The results reveal that when one of the transducers within the array is tilted the wave front is heavily distorted. In contrast a shift of one of the transducers case minimal distortion of the ideal wave field. The obtained results enable modification of array configuration in order to improve the wave generation characteristics.

1 Introduction

Due to their layered composition and the production procedures, the fiber- or textile-reinforced thermoplastics enable the possibility for material integration of functional elements, like sensors, actuators or electronic circuit boards. Such elements are a vital prerequisite for successful implementation of smart functions, e.g. active vibration damping, load monitoring or structural health monitoring.

State-of-the-art smart functions utilize elements, which are mainly adhesively bonded to or into the structural components [1, 2]. The associated assembly and bonding processes are, however, characterized by several labor- and time-intensive work steps. Additionally, the adhesive bonding of the function elements to the fiber-reinforced polymer structure causes a loss of deformation transfer and hence an inefficient use of sensor and actuator potentials [3]. A solution to that problem is the application of novel thermoplastic-compatible modules where their plastic carrier film is made from the same material as the matrix material of the fiber-reinforced component. Application of such modules enables a successfully transformation of the current manual production process of active textile-reinforced thermoplastic composites into an automated series-production process. A challenging issue that still needs to be solved is related to the assurance of the post-manufacturing position of the modules within the smart component [4]. This problem becomes vital, considering a module array where the position and orientation of the individual elements is essential for their correct operation. Since the assessment of misalign and misorientation influence on the operation characteristics is geometry specific, investigation of possible combinations of modules size, composite layup, and component geometry is not feasible. Therefore, an elementary configuration has been analyzed consisting of a rectangular base geometry and attached to the plate piezoelectric sensor-actuator arrays.

2 Problem definition

Embedded piezoelectric transducer arrays are suitable for radiation and reception of plate waves. This property can be used for ultrasound-based measuring tasks [5, 6], load monitoring [7] or structural health monitoring applications [8, 9]. For ultrasound measurement tasks, the plate waves are used for an efficient radiation of sound waves into the adjacent media, e.g. air or water. This effect can also be reversed in order receive sound waves.

The sound radiation and reception is based on the interaction of fluid and solid waves. Especially the bending wave, also known as the first asymmetric plate wave mode, can be efficiently used for sound radiation due to its short wavelength and high out-of-plane displacement components. Additionally, for some measurement applications it is advantageous to directionally send or receive sound waves. The first step to obtain directional ultrasound radiation is the generation of directional bending waves in the plate. This can be achieved by using transducer arrays instead of a single transducer. Through adaptation of the actuator array configuration, the mainly excited or received plate wave mode can be precisely controlled [10, 11]. Furthermore, the directivity of the plate waves can also be adjusted [12]. Depending on the size and the distance between the individual transducers, the electrical driving signal for every transducer has to be defined in order to shape the wave characteristics. On the one hand the distance between the individual transducers need to be precisely known in order to optimally drive the transducer array. On the other hand the relative position between the transducers is influenced by the limited tolerance of the manufacturing process. Since a calibration would require a labor-extensive characterization of every manufactured active component, a relation between the position and angle deviation and the ability to generate a directional wave need to be identified. This problem has been preliminarily investigated in the presented contribution using a parametrical finite element model.

3 Numerical model

A three-dimensional parametrical model consisting of two submodels: a free-free supported plate and attached to it four piezoelectric transducers (transducer array), was elaborated. The model has been created using a commercially available finite-element software [13]. The position and angle of one of the transducers are freely variable. The general overview of the developed model including the geometrical configuration and the physical interpretation of the free parameters (Δx, Δy, $\Delta \alpha$) is presented in Fig. 1.

To realistically simulate the interaction between the electrical driving signal of the transducers and the resulting plate wave, a coupled electromechanical problem has to be solved. Therefore the transducers were modelled as 3-D 20-Node Coupled-Field solid elements (SOLID 226). The elastic base structure has been meshed with 116568 quad elements of type PLANE 223 with a maximum element size 0.2 mm.

In order to capture the time and space dependent phenomena connected with the propagation of mechanical waves, a transient analysis with the time step of 2.5 µs has been performed. Herein the termination time was set to 500 µs what results in 200 load steps per one simulation. The mechanical properties of the base structure have been determined in the experimental investigations.

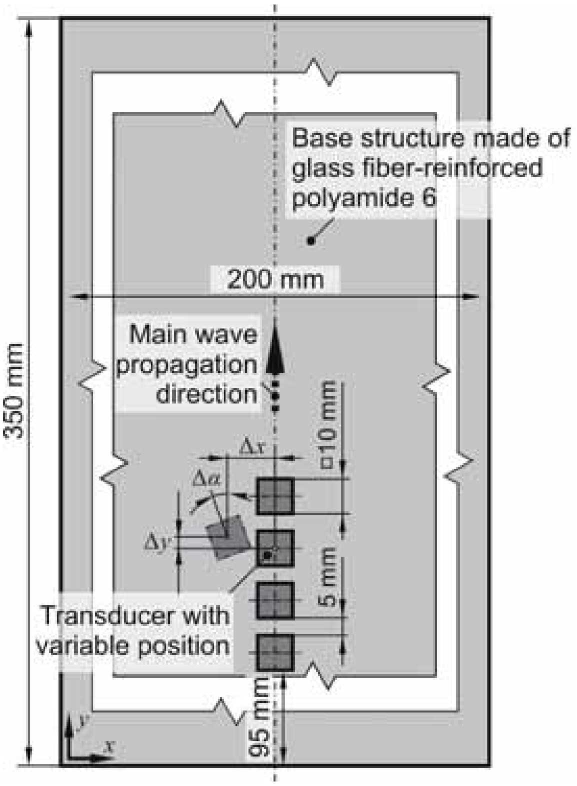

Fig. 1: *General overview of the elaborated model with geometrical interpretation of the modifiable parameters*

3.1 Identification of mechanical material parameters

The investigated material consists of glass fiber-reinforced polyamide 6 semi-finished product – TEPEX® 102-RG600(x)/47%, produced by Bond-Laminates GmbH. This composite material is characterized by a twill wave reinforcement balanced in longitudinal and transversal direction and the thickness of a single layer of 0.25 mm. In order to determine the mechanical properties 15 samples from this material with the size 25 mm x 250 mm have been manufactured. The investigated material consists of 8 individual layers thus the thickness of one sample equals to 2 mm.

The determination of the material parameters of the base structure was performed by means of standardized tensile tests using tensile testing machine (Z100, Zwick Roell AG) instrumented with a video extensometer. Since the investigated material is characterized by anisotropic properties, specimens cut under angle of 0°, 45° and 90° in relation to the longitudinal direction of the reinforcement were investigated. The mechanical material properties used in the simulation are summarized in Table 1.

Table 1: *Mechanical material parameters of the TEPEX® 102-RG600(x)/47%*

Property	*Symbol*	*Value and unit*
Young's Modulus[1]	$E_{\parallel}$	*19.83 GPa*
	$E_{\perp}$	*5.76 GPa*
Shear Modulus[2]	$G_{\#}$	*7.3 GPa*
Poisson's ratio[3]	$\nu_{\parallel\perp}$	*0.17*
Density[3]	ρ	*1.8 g/cm³*

The transducers were assumed to be made from piezoelectric ceramics based on lead zirconate titanate (type PIC181 manufactured by Physik Instrumente (PI) GmbH & Co. KG). The corresponding material parameters were assumed solely based on the manufacturer data [15] (v. Table A.1 in Appendix A) and calculated to the notation required by the applied finite element software.

3.2 Simulation setup

The transducers were driven by a sinus windowed cosine signal with 35 kHz fundamental frequency and amplitude A equaling 6 V (Fig. 2). Application of a narrow bandwidth signal with a certain number of cycles can greatly prevent wave dispersion [16].

In order to generate a directional plate wave, the transducers have to be activated in predefined moments in order to amplify the desired plate mode as well as to shape the directional characteristics of the propagating wave. The geometrical configuration together with the material properties of the base structure governs the optimal time delay which in the presented study equals 23.4 µs.

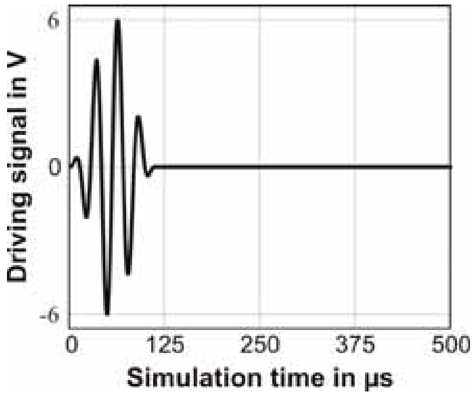

Fig. 2: *Exemplary transducer driving signal*

Following configurations have been investigated:

- optimally driven transducer array without any geometrical deviation from the ideal configuration as a reference,
- transducer array with one of the transducers moved geometrically in x-direction by 2 mm in comparison with the ideal configuration,
- transducer array with one of the transducers moved geometrically in y-direction by 2 mm in comparison with the ideal configuration,
- transducer array with one of the transducers tilted geometrically by 20° in comparison with the ideal configuration.

All deviation values were estimated based on the observations of manufacturing of similar components since the experimental data is not present at the time. Nevertheless, the model can deliver already a good insight into the phenomena that can occur in possible applications.

The time-delays of the driving signals for all the investigated configurations were set as if the information about the geometrical distortion would be not known. Such an approach matches the real application situation when the active components are not characterized individually after the manufacturing process.

4 Results and discussion

Since the obtained data is a function of time, place and analyzed configuration, a simple and informative presentation of the results is greatly limited. In order to visualize change of the wave fields due to transducer array misorientation, snapshots at the same time of the propagating wave for every analyzed configuration has been created. Subsequently, the differences between the snapshots have been calculated and taken as a measure of the influence of geometrical deviation on the performance of the transducer array to generate directional waves.

---

[1] Tested according to DIN EN ISO 527-4 Standard

[2] Determined following the procedure in DIN EN ISO 14129 Standard

[3] Provided by the manufacturer in [14]

4.1 Wave fields for the analyzed configurations

For the result presentation, the wave field for one time step namely at 20 µs has been selected based on the following criteria:

- the wave has to propagate trough some distance in order to reveal its directivity and plate mode character
- the reflections of higher plate modes – if any present – from the plate edges should not interfere with the main wave front.

In Fig. 3 the wave fields for all investigated configurations can be seen[4]. Herein, it is clearly visible that when one of the transducers is tilted geometrically (Fig. 3 D) the wave amplitude is much smaller in comparison not only with the reference case but also with configurations with geometrically shifted transducer.

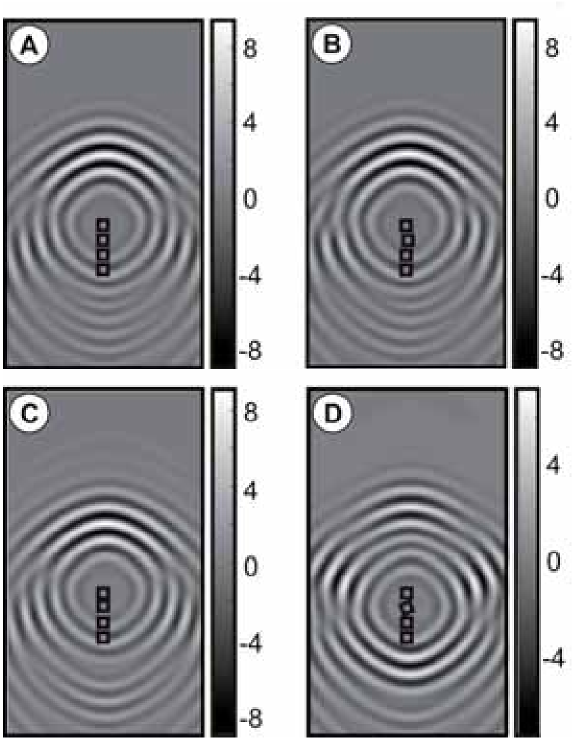

Fig. 3: *Out-of-plane displacements (in nm) of the plate wave generated by a transducer array.* ***(A)*** *For the transducer array without any geometrical deviation.* ***(B)*** *For the transducer array with one transducer moved in x-direction by 2 mm.* ***(C)*** *For the transducer array with one transducer moved in y-direction by 2 mm.* ***(D)*** *For the transducer array with one transducer tilted by 20 deg*

Although the influence of the transducer shifted in any of the analyzed directions on the wave shape seems to be marginal some difference between the cases can be noted. The shift in x-direction (Fig. 3 B) causes unsymmetrical distortion of the wave field left and right to the main wave propagation direction. In contrary, the shift in y-direction (Fig. 3 C) manifests itself in distortion of the wave field along the main wave propagation direction. In order to visualize the changes in the wave fields caused by the geometrical misorientation of one of the transducer within the array, the difference between the wave fields has been calculated with regard to the reference case.

4.2 Distortion of the wave fields

On Fig. 4 the distortion of the wave fields due to the transducer array misorientation is presented.

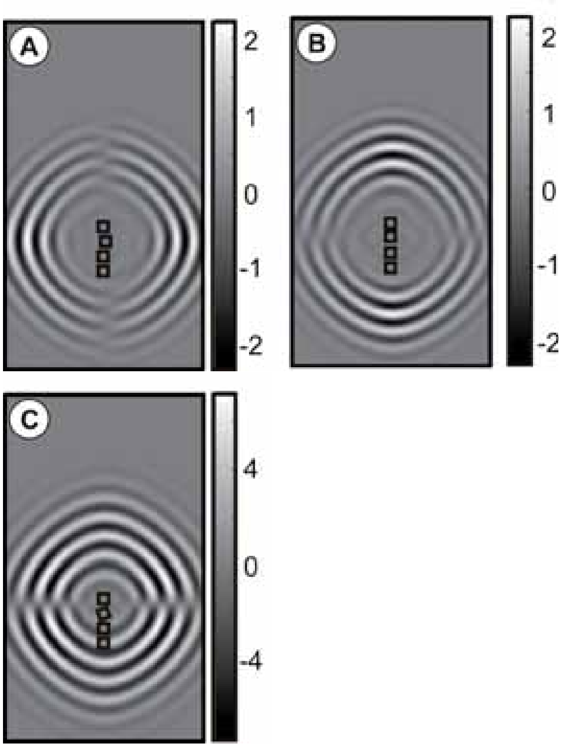

Fig. 4: *Change of the out-of-plane displacement (in nm) of the plate wave generated by a transducer array in relation to the transducer array without any geometrical deviation.* ***(A)*** *For the transducer array with one transducer moved in x-direction by 2 mm.* ***(B)*** *For the transducer array with one transducer moved in y-direction by 2 mm.* ***(C)*** *For the transducer array with one transducer tilted by 20 deg*

By analyzing the resulting wave fields it can be noted that:

- the main change of the wave field for the transducer array with one of the transducers moved geometrically in x-direction can be seen on the left and right from the main wave propagation direction (Fig. 4 A). The amplitude of the change accounts to approx. 25% of the ideal case,

---

[4] For animations refer to Table A.2

- for the transducer array with one of the transducers moved geometrically in y-direction, the biggest change of the wave field can be seen along main wave propagation direction (Fig. 4 B). The amplitude of the change accounts as in the previous case to approx. 25% of the ideal case,
- for the transducer array with one of the transducers tilted, the change of the wave field is very significant (Fig. 4 C): the amplitude of the change accounts to approx. 80% of the ideal case. This can be explained by the fact that in this configuration the wave propagation is not strictly directional.

5 Conclusions and outlook

In the contribution the influence of geometrical distortion of the transducer array on the mechanical wave generation has been studied. Herein, the reference case with optimally driven transducer array without any geometrical deviation from the ideal configuration as well as transducer array with one of the transducers moved geometrically in x-direction by 2 mm, in y-direction by 2 mm and tilted geometrically by 20° have been independently modelled and analyzed.

It is clearly visible that when one of the transducers is tilted geometrically the wave front is heavily distorted. Moreover, the change of the wave field is very significant and accounts to approx. 80% of the ideal case. The marginal influence of the transducer shift in any of the analyzed directions on the wave shape has been observed. Nevertheless, some difference between the cases can be noted. The transducer shift in x-direction causes unsymmetrical distortion of the wave field left and right to the main wave propagation direction whereas the shift in y-direction manifests itself in distortion of the wave field along the main wave propagation direction.

In the future investigations the aspects connected with the actual manufacturing distortions as well as experimental validation of the presented results are intended.

Acknowledgments

The presented work is part of the research within the context of the Collaborative Research Centre/Transregio (SFB/TR) 39 PT-PIESA, subprojects T03 and B04.

The authors are grateful to the Deutsche Forschungsgemeinschaft (DFG; *eng. German Research Foundation)* for the financial support of the SFB/TR39.

Literature

[1] *Hufenbach, W., Gude, M. u. Heber, T.: Embedding versus adhesive bonding of adapted piezoceramic modules for function-integrative thermoplastic composite structures. Composites Science and Technology 71 (2011) 8, p. 1132–1137*

[2] *Moharana, S. u. Bhalla, S.: Influence of adhesive bond layer on power and energy transduction efficiency of piezo-impedance transducer. Journal of Intelligent Material Systems and Structures, p. 247–259*

[3] *Hufenbach, W., Gude, M. u. Heber, T.: Development of novel piezoceramic modules for adaptive thermoplastic composite structures capable for series production. Sensors and Actuators A: Physical 156 (2009) 1, p. 22–27*

[4] *Kostka, P., Holeczek, K. u. Hufenbach, W.: Structure-integrated Active Damping System: Integral Strain-based Design Strategy for the Optimal Placement of Functional Elements. International Journal of Composite Materials 3 (2013) 6B, p. 53–58*

[5] *Kunadt, A., Pfeifer, G. u. Fischer, W.-J.: Ultrasound Flow Sensor Based on Arrays of Piezoelectric Transducers Integrated in a Composite. Materials Science Engineering, Symposium B6 - Hybrid Structures. Procedia Materials Science 2 (2013), p. 160–165*

[6] *Kunadt, A., Pfeifer, G. u. Fischer, W.-J.: Ultrasonic flow meter with piezoelectric transducer arrays integrated in the walls of a fiber-reinforced composite duct. IEEE 2012*

[7] *Kostka, P., Höhne, R., Maron, B., Ehlig, J. u. Hufenbach, W. A.: Multidisciplinary Analysis Concept for the Development of a Composite Adaptive Leaf Spring. International Journal of Composite Materials 3 (2013) 6B, p. 10–16*

[8] *Kostka, P., Holeczek, K. u. Hufenbach, W.: A new methodology for the determination of material damping distribution based on tuning the interference of solid waves. Engineering Structures 83 (2015) 83, p. 1–6*

[9] *Boller, C.: Next generation structural health monitoring and its integration into aircraft design. International Journal of Systems Science 31 (2010) 11, p. 1333–1349*

[10] Li, J. u. Rose, J. L.: Implementing guided wave mode control by use of a phased transducer array. Ultrasonics, Ferroelectrics, and Frequency Control, IEEE Transactions on 48 (2001) 3, p. 761–768

[11] Giurgiutiu, V.: Tuned Lamb Wave Excitation and Detection with Piezoelectric Wafer Active Sensors for Structural Health Monitoring. Journal of Intelligent Material Systems and Structures 16 (2005) 4, p. 291–305

[12] Yu, L. u. Giurgiutiu, V.: In-situ optimized PWAS phased arrays for Lamb wave structural health monitoring. Journal of Mechanics of Materials and Structures 2 (2007) 3, p. 459–487

[13] ANSYS, Inc.: ANSYS® Academic Research, Release 15.0

[14] Tepex® dynalite 102-RG600(x)/47% Roving Glass – PA 6 Consolidated Composite Laminate. Material Data Sheet, Bond-Laminates GmbH, http://bond-laminates.com/uploads/tx_lxsmatrix/MDS_102-RG600_x_-47_.pdf, 2014

[15] Material Data. Specific parameters of the standard materials, Physik Instrumente (PI) GmbH & Co. KG, http://www.piceramic.com/download/PI_Ceramic_Material_Data.pdf, 2015

[16] Su, Z. u. Ye, L.: Identification of damage using Lamb waves. From fundamentals to applications. Lecture notes in applied and computational mechanics, Bd. 48. Berlin: Springer 2009

Appendix A

***Table A.1:** Material parameters of the PIC181 lead zirconate titanate material [15]*

Property	*Symbol*	*Value and unit*
Density	ρ	*7.8 g/cm^3*
Young's Modulus	E_{11}	*122 GPa*
	E_{21}	*54 GPa*
	E_{31}	*56 GPa*
	E_{22}	*103 GPa*
	E_{23}	*54 GPa*
	E_{33}	*122 GPa*
	E_{44}	*33 GPa*
	E_{55}	*31 GPa*
	E_{66}	*33 GPa*
Permittivity in vacuum	ε_0	*8.85 x 10^{-12} F/m*
Piezoelectric stress coefficients	e_{31}	*-7.1 C/m^2*
	e_{33}	*14.4 C/m^2*
	e_{15}	*15.2 C/m^2*
Relative permittivity at constant strain	ε_{11}	*413*
	ε_{33}	*877*

***Table A.2:** Animations of the wave fields for analyzed array configurations*

http://wwwpub.zih.tu-dresden.de/~mdanne/tr39_2015_01.html	Reference. Optimally driven transducer array without any geometrical deviation from the ideal configuration
http://wwwpub.zih.tu-dresden.de/~mdanne/tr39_2015_02.html	Transducer array with one of the transducers moved geometrically in x-direction by 2 mm in comparison with the reference
http://wwwpub.zih.tu-dresden.de/~mdanne/tr39_2015_03.html	Transducer array with one of the transducers moved geometrically in y-direction by 2 mm in comparison with the reference
http://wwwpub.zih.tu-dresden.de/~mdanne/tr39_2015_04.html	Transducer array with one of the transducers tilted geometrically by 20° in comparison with the reference

Structurally integrated piezo-actuators for manipulation of structure-borne sound transfer paths of rear axles

Lochmahr, M.[1]; Hofmann, M.[1]; Drossel, W.-G.[2]; Troge, J.[2]; Zumach, S.[2]

[1]Mercedes AMG GmbH
[2]Fraunhofer-Institut für Werkzeugmaschinen und Umformtechnik

Abstract

The gear whine phenomenon of rear axles is a well-known acoustic issue especially in rear-wheel and four-wheel drive vehicles. The acoustical optimization of this problem leads to the major goal conflict: improvement of the vibrational isolation of the rear axle versus excellent driving dynamics of the vehicle. One possible solution for this issue is in focus of a research project at Fraunhofer Institute for Machine Tools and Forming Technology IWU in cooperation with Mercedes AMG GmbH. The aim is to reduce the noise contributions of the rear axle using an active vibration control system based on structurally integrated piezo-actuators on the transfer path from the axle into the vehicle.

1 The gear whine phenomenon of rear axles

The tooth mesh can be seen as the main noise source in gears. Due to the changing stiffness in the contact zone of the tooth flanks, while rolling off on another, a so-called parameter excitation occurs which causes dynamic forces in the gear mesh. Furthermore, there are geometric deviations due to the production process and designed flank modification, which additionally effects a periodical displacement excitation.

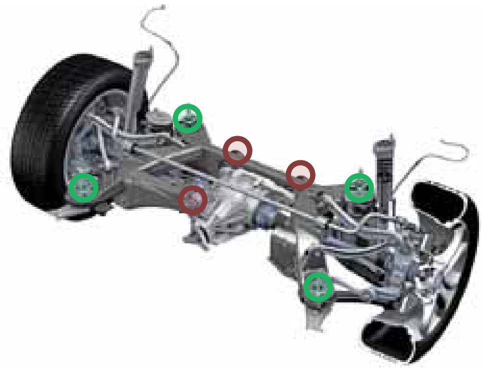

***Fig. 1:** Example rear axle assembly (red markers: mounts of differential gear box, green markers: rear sub frame mounts) Source: Daimler AG.*

The resulting dynamic forces are transferred over the shaft-bearing system into the housing structure of the differential gear box. Besides direct sound radiation of the housing due to surface velocities, structure-borne energy is transferred over the bearing system into the vehicle body.

In terms of rear axles, the excitation is higher compared to typical transmission gear boxes due to the high torque which needs to be transmitted through the complete drive train. Basically, rear axles of passenger cars are decoupled twice from the vehicle body using a rear sub frame (Fig. 1, Fig. 2). The elastomer elements between axle and frame are typically arranged as a three-point-bearing and the sub frame is coupled to the vehicle body using four elastomer mounts. In terms of a force excitation from the gear mesh, the rear axle is forced to oscillate in its flexible mounting. The resulting rigid-body motions and sensitive frequency ranges depend on the distribution of the dynamic mass and the boundary mounting conditions.

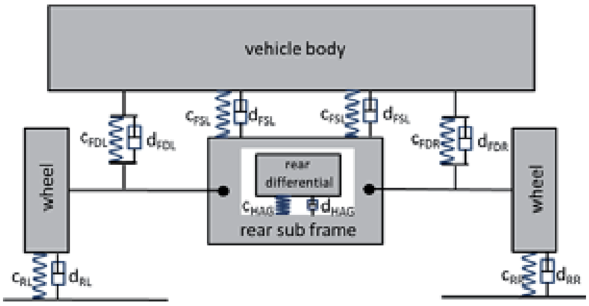

***Fig. 2:** Schematic vibration model of the rear axle and it´s double elastic mounting*

Typical operational deflection shapes are pitching, rotating, wobbling. In all cases, a significant amount of structure-borne energy is transmitted through the rear axle mounting in the sub frame. Afterwards, the structure-borne sound is transferred through the frame and its elastomer mount into the vehicle body. Structural modes of the frame can be also excited within certain frequency ranges and additionally transferred into the vehicle.

In the passenger compartment gear whine is perceived as a load and drive speed dependent tonal noise. Because of the narrowband noise characteristics, it is an annoying and unpleasant sound, which is even noticeable at low sound pressure levels. The frequencies of gear whine result from the rotation speed of the driveshaft multiplied with the number of teeth of the bevel wheel which is called the first gear mesh order. The first order is the dominant one in most cases. Sometimes also the harmonics like 2nd, 3rd and 4th order contributes to the overall sound pressure level [1]. In most cases, the whining noise is not present in all operating modes of the vehicle, instead there are often just a few speed ranges where the gear noise is dominating the interior noise.

2 Transfer path of rear axle noise to the driver´s ear

For analyzing the noise phenomenon, measurements have been carried out on different test vehicles under changing driving conditions. Beside the measurement of sound pressure level at different positions in the passenger compartment, acceleration signals in front of and after each mounting positions in three dimensions as well as the rotations speed of the drive shaft have been recorded. From comparison of the overall sound pressure level and the extracted 1st and 2nd gear mesh orders at different rotation speeds, the critical operation modes from acoustical point of view could be identified. For example, Fig. 3 shows a measurement of a vehicle under partly load conditions. Between 1800 and 1900 rpm the 1st gear mesh order is dominating the overall level, which can be perceived as a distinct gear whine noise inside the car.

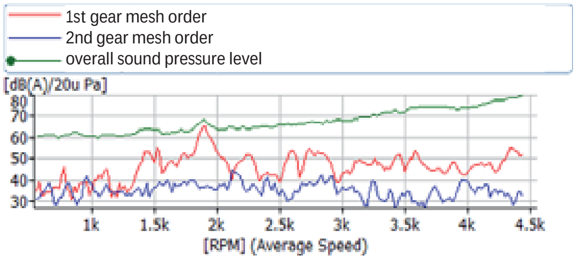

Fig. 3: *Overall sound pressure level at driver's ear and 1st and 2nd gear mesh order over rotation speed of the drive shaft*

All critical frequencies and corresponding rpm-ranges for the interior noise could be identified in this way. In a further step, the responsible rigid-body motion of the rear axle has been calculated and animated based on measured acceleration signals using a simple structure model. The relevant operational vibrations are wobbling and rotating modes of the rear axle body in its mounting points. Fig. 4 shows an example rigid-body motion of the rear axle at 540 Hz, which corresponds to a driving speed of 80 km/h. Major deformations can be detected at the front mount and the left rear mount, which is due to a wobbling mode. It is obvious, that depending on the rigid-body motion of the differential gear housing, the structure-borne energy transfer into the sub frame can significantly vary between the different mounting positions and spatial directions.

Fig. 4: *Measured rigid-body motion of the rear axle at 80 km/h*

The occurring operational deflection shapes are forced oscillation excited by the dynamic components of the redirected moment within the rear axle differential.

3 Vibration reduction by structurally integrated piezo-actuators

An active vibration control system (AVC) is based on the idea to compensate disturbing vibration by inducing an additional vibration with opposite phase (180° phase shift). For generation of the compensating vibration, different actuator types can be used depending on the required force level, acceleration level and the interesting frequency range. Actuators based on piezo ceramics have been used for several practical applications yet, in order to reduce unrequested vibration. The main advantage is the high force level which can be generated with less space and weight compared to other actuator types. The achievable displacements are comparable low. For AVC in the middle and high frequency range, where in most cases force excitations are needed, piezo-actuators in form of patches or stacks are most suitable. In the last years, various active fiber composite actuators based on piezoelectric ceramic materials have been developed. Relevant types are for example ›Active Fiber Composites‹ (AFC) [2], ›Macro Fiber Composite‹ (MFC) [3], DuraAct–patch transducer (DuraAct) [4] und ›Multilayer piezo composites‹ [5]. There are several commercial products available at the market yet. They can be used with actuator or sensor functionality as well. A connection to the structure is usually established by gluing the actuator on the surface. In terms of AVC-application, an alternative approach has been developed within the SFB/TRR 39 PT-PIESA, which is the direct integration of the actuator in a metal structure e.g. between two metal sheets. The production process consists of an automated application of adhesive and piezo module on a metal sheet, placing of a top layer metal sheet and forming of the complete composite, while the adhesive is still viscous. In this way, it is possible to manufacture complex, three-dimensionally shaped piezo-metal-composites with structurally integrated actuator/sensor functionality (Fig. 5).

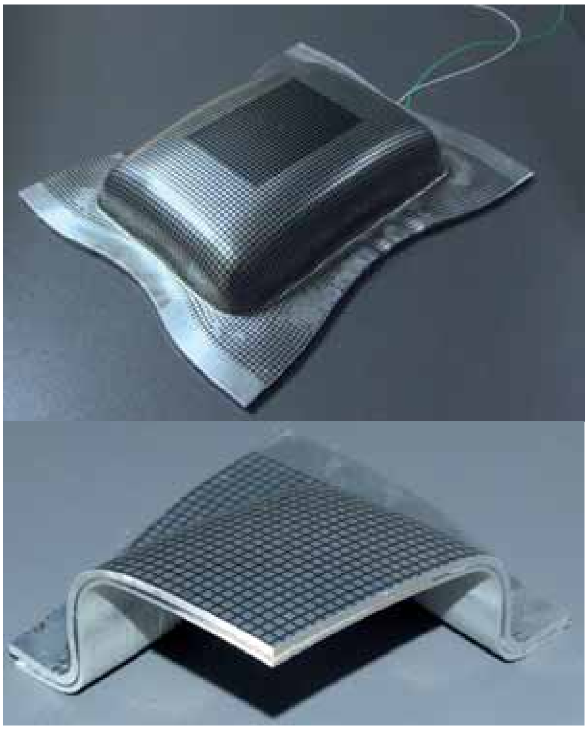

***Fig. 5:** Example of a three-dimensionally shaped structure with integrated actuator/sensor functionality*

The main advantages of this technique are:

- actuator can be placed directly in the force flow
- actuator countracts the material deformation not only on the surfaces rather directly in the material
- actuator counteracts the material deformation not only on the surface rather directly in the material
- actuator modules directly protected against external influences (moisture, dirt, salt etc.)

Besides AVC, there are different applications where structurally integrated piezo-actuators can be used: e.g. active noise control (ANC), structural health monitoring or sound generation.

4 Solutions for noise reduction of rear axles

There are several primary and secondary measures to lower gear noise inside a car, which in most cases influences other functionalities and leads to major goal conflicts. The most efficient way is to lower the excitation from the gear mesh, which is the structure-borne sound source (primary measure). From experience, a significant reduction of the gear excitation often causes a worse durability behavior in combination with lower system effectiveness. In addition, the production costs for an acoustical optimized gear is much higher due to high demands on production accuracy in terms of micro geometry and surface quality. A second way for gear noise reduction is the optimization of the transfer path into the passenger compartment, which are so called secondary measures. The three mounts of the differential gear box seem to be most suitable since they are the direct connection to the sub frame. Lowering the stiffness would improve the vibration isolation significantly. But the vibrational behavior of the whole drive train (engine, gear box, drive shaft, rear axle) will be negatively influenced. Because of the high excitation of the engine, the drive train is forced to torsional motions. Lowering the stiffness of the differential housing will shift eigenmodes to lower frequencies, where the main torsional engine vibrations occur. This will lead to a worse ride comfort inside the car due to torsional deflection shapes of the drive train. The third possibility for gear noise reduction is the improvement of the isolation of the rear sub frame mounts by changing to lower stiffness. This will also affect the driving dynamics significantly because movements of the rear axle relatively to the car body will be increased. In terms of high performance vehicles, the driving dynamics is a major selling point. That´s why it is not an option to change the stiffness characteristics of the rear sub frame mounts [6]. Because of the presented goal conflicts in the acoustical development process of high performance cars, active systems for vibration reduction come into consideration. There are different approaches, which needs to be analyzed in detail with view on the application on a rear axle. First possible configuration could be an actuator, which is mounted directly on the differential gear housing to interact with the rigid-body motion. Because of the high dynamic mass, which is moving, the force level of such an actuator will be quite high, which makes it inefficient. Second way could be a direct force input into the connection points to the vehicle body. This will be most effective because it is closest to the receiver position inside the car. Since, there are 4 mounting positons with each 3 degree of freedom, a quite complex active system consisting of several actuators needs to be setup. Furthermore, the control algorithm will be also quite complex, because there will be additional crosstalk between the excitation points which needs to be taken into account.

Based on these basic considerations, influencing the structure-borne energy flow over the rear sub frame seems to be the most promising approach [7]. In this configuration, an actuator is placed on a point on the rear sub frame, where the energy flow can be influenced in a best way (Fig. 6).

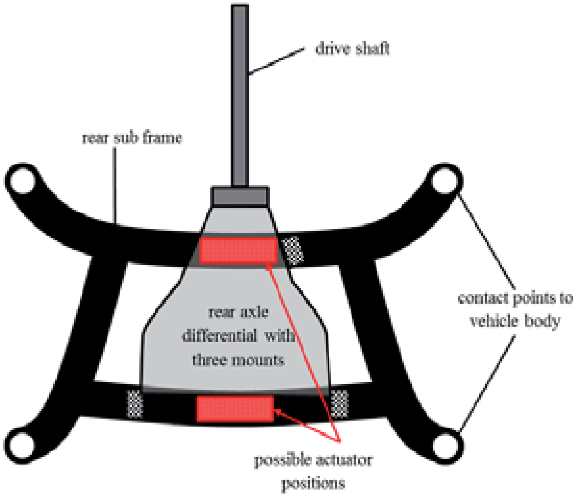

Fig. 6: *Example positions of piezo-actuators for an AVC-system on a rear axle*

The required force level on the rear sub frame, behind the differential mounts, will be much lower compared to a direct interaction with the moving gear housing. Furthermore, there will be no negative influence on other functionalities like mentioned before.

5 Simulation model for rear axle noise

In order to reduce the structure-borne energy, which is transmitted through the rear sub frame mounts into the vehicle, the actuator needs to be placed on a position on the frame, where it can influence the force flow ideally in all 4 mounting positions in the dominant directions.

Fig. 7: *FE simulation model of the rear axle*

A FEM simulation model has been set up, in order to find the optimal actuator position for an AVC-System. It consists of the rear axle components, which influence the rigid-body motion of the axle body and the structure-borne energy transfer in the vehicle (Fig. 7). These are the rear sub frame, the gear housing, the drive shaft and all mounts on axle and vehicle side. For simplification and reduction of calculation time, the excitation from the gear mesh is not included in the model. Instead, the acceleration signals, which have been measured in the full vehicle tests, are applied to the rear axle mounting positions to simulate the operational deflection shape within the calculation model. This gives a sufficient accurate simulation of the operational vibrations as well as the operational force input through the rear sub frame mounts which is the relevant transfer path for lowering gear noise contributions in the passenger compartment.

Fig. 8 shows the simulated rigid-body motion of the rear axle at 80 km/h which is similar to the measured mode shown in Fig. 4.

Fig. 8: *Simulated rigid-body motion of the rear axle at 80 km/h*

In a next step, the model is used to calculate transfer functions from possible excitation points to the contact point at the vehicle body. High sensitivity in the TFs corresponds to high potential for influencing the force flow into the car structure. Using a point net on the rear sub frame, the TFs from a normal excitation at a driving point to the three dimensional force reactions at 4 mounts are calculated. Because of the high stiffness of the sub frame mounts and the low accelerations which has been measured on the car body side, a force dominated energy transfer can be assumed. That´s why a force to force transfer function should give the relevant information about influencing the energy flow.

As a result, 12 TFs for each excitation points are calculated. This leads to a three-dimensional n x 12 x f matrix $[\underline{H}_{nm^{xyz}}]$ of transfer functions, where n is the number of the driving points, m is the number of rear axle mount ($m = 1,2,3,4$), x, y, z are the spatial direction and the third dimension of the matrix is frequency (1).

$$diag(\underline{F}_1, \underline{F}_2, \dots, \underline{F}_n) \cdot \left\lfloor \underline{\mathrm{H}}_{nm^{xyz}} \right\rfloor = \begin{bmatrix} \underline{F}_{11x} & \underline{F}_{11y} & \underline{F}_{11z} & \underline{F}_{12x} & \cdots & \underline{F}_{14z} \\ \underline{F}_{21x} & \underline{F}_{21y} & \underline{F}_{21z} & \underline{F}_{22x} & \cdots & \underline{F}_{24z} \\ \vdots & \vdots & \vdots & \vdots & \dots & \vdots \\ \underline{F}_{n1x} & \underline{F}_{n1y} & \underline{F}_{n1z} & \underline{F}_{n2x} & \cdots & \underline{F}_{n4z} \end{bmatrix} \quad (1)$$

A subsequent analysis of the matrix will show the most promising driving point. This will be done by looking for the row with the highest force sensitivities in a certain frequency. For different modes of the rear axle at different frequencies, diverse sensitive driving points may be identified.

A second analysis method, which could give promising results, is the evaluation of structural intensity (STI) which is a parameter for energy transfer within a structure. STI is defined as a scalar product of the force, which is acting on a surface element, and the occurring velocity. Compared to the acoustical intensity, the scalar value pressure needs to be replaced by the stress tensor [8], [9]. The STI-analysis, as a tool for visualization of energy transfer, will be investigated later in the project. It will show the positions on the rear sub frame with highest structural energy flow. Following, the ability for noise reductions of these possible driving positions for an actuator is analyzed in the simulation model.

6 Rear axle test bench

For verification of the simulation, full vehicle measurements are not suitable because the excitation effects and transfer paths cannot be separated. Furthermore, it is very difficult to directly measure operational forces on a driving vehicle. For that reasons, a rear axle test bench has been set up. It consists of the complete rear axle assembly except break components and wheels. For defined boundary conditions at the rear axle mounts, a “blocked force” configuration has been used.

Fig. 9: *Rear axle test bench with shaker excitation*

Instead of the car body, the axle is rigidly mounted on a vibration fundament (Fig. 9). As already mentioned in section 5, it can be assumed, that the structure-borne energy transfer is force-dominated. That’s why, the force deviation to the real boundary conditions in the car will be minimal in this setup. In addition, the boundary conditions are comparable with the simulation model. To measure operational forces, three-dimensional force transducers are connected between rear sub frame mounts and fundament. The excitation of the gear mesh is not induced by rotating gears but rather simulated by exciting the rigid-body motion of the differential gear housing using a shaker. If the measured accelerations before the differential mounts are similar to the measured ones on the test bench, it can be assumed, that the structure-borne energy transfer in to the sub frame is also on a comparable level.

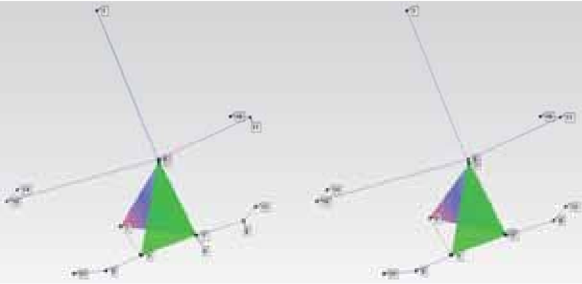

Fig. 10: *Comparison of operational deflection shape of the rear axle at approx. 100 km/h, left: rear axle test bench, right: full vehicle test on roller test bench*

Fig. 10 shows a comparison of the operational deflection shape at a vehicle speed of approx. 100 km/h which has been reproduced on the test bench and measured in a full vehicle on a roller test bench. In appearance, the two deflection shapes are nearly equal which could be also confirmed by calculation of the Modal Assurance Criterion (MAC), which shows the correlation between two shapes. The calculated value is MAC = 0.91 which implies a very good correlation.

The test bench with the reproduced deflection shapes can now be used to test possible actuator positions for an active vibration control system, which has been derived from a simulation. The force reduction at the sub frame mounts will show the effectiveness of the varying excitation positions and will give an indication for an operational force reduction in a vehicle.

7 Further investigations

Based on the simulation and the investigations on the rear axle test bench, one or two actuator positions with high potential for noise reduction will be determined. Following, these excitation points need to be tested with a piezo patch actuator in order to analyze the required force and the effectiveness of the system.

Later on in the project, the production process for an integration of the piezo-actuator in the sub frame will be developed and implemented in order to build prototype parts and carry out test on a full vehicle under driving conditions.

8 Conclusion

The integration of a piezo based actuator in a sub frame of a rear axle seems to be a promising approach to significantly reduce gear noise of the rear differential in the passenger compartment of a car. In addition, it could be a reasonable alternative to the known primary and secondary measures for gear noise reduction and will also solve major goal conflicts in the development process. In terms of costs and complexity, an AVC-system for rear axle has a considerable advantage because new significant possible savings can be generated, e.g.:

- reduction of production costs for acoustically optimized gears → higher excitation of low gear qualities could be compensated by AVC-system
- reducing mass on rear axle components and vehicle body → worse acoustical behavior could be compensated by the AVC-system

The final concept of an AVC-system for rear axle noise including actuator, production process, control algorithm, high voltage amplifier needs to be analyzed in detail and compared in terms of estimated costs in a series production and potential savings on a full vehicle.

Literature

[1] Linke, H.: Stirnradverzahnung, Berechnung - Werkstoffe – Fertigung. 2nd edition, Carl Hanser Verlag München Wien, 2010.

[2] Bent, A. A.: Active Fiber Composites for Structural Actuation. Dissertation, Massachusetts Institute of Technology, 1997.

[3] Wilkie, W. K.; Bryant, R. G.; High, J. W.; Fox, R. L.; Hellbaum, R. F.; Jalink, A.; Little, B. D.; Mirick, P. H.: Low-cost piezocomposite actuator for structural control applications. In: Jacobs, J. H. (Hrsg.): Smart structures and materials 2000: Industrial and Commercial Applications of Smart Structures Technologies. Proc. SPIE 3991, S. 323-334.

[4] Wierach, P.: Entwicklung multifunktionaler Werkstoffsysteme mit piezokeramischen Folien im Leitprojekt Adaptronik: Active systems for dynamic markets – Adaptronic Congress. Göttingen 2003.

[5] Wierach, P.: Low Profile Piezo Actuators Based on Multilayer Technology: 17th International Conference on Adaptive Systems and Structures 2006.

[6] Lochmahr, M.; Hofmann M.; Albers, A.; Behrendt, M.: Interdisziplinäre Validierung von Elastomerlagern der Hinterachse bei Performancefahrzeugen. 10th Conference Dynamisches Gesamtsystemverhalten von Fahrzeugantrieben, Ludwigsburg, 2015.

[7] Eulert, S.; Bräunig, J.; Lührs, G.; Bucht, A.; Kunze, H.: Reduction of the inner vehicle noise level by active vibration damping of the rear axle drive. Conference Getriebe in Fahrzeugen 2011 : Effizienzsteigerung im Antrieb. Düsseldorf : VDI-Verl., 2011, S. 477-488. (VDI-Berichte 2130).

[8] Cremer, L.; Heckl, M.: Structure-Borne Sound. 2nd edition, Springer. Berlin 1996.

[9] Kuhl, S.: Gezielte Leitung von Körperschall unter Zuhilfenahme der Strukturintensitätsrechnung. Dissertation, TU Darmstadt, 2009.

Novel poling method for active fibre-reinforced polyurethane composites

Eßlinger, S.; Geller, S.; Hohlfeld, K.; Gebhardt, S.; Michaelis, A.; Gude, M.; Schönecker, A.; Neumeister, P.

Fraunhofer-Institut für Keramische Technologien und Systeme IKTS, Dresden

Abstract

Fibre-reinforced composites are considered to meet current and future challenges of function integrated lightweight components. Questions regarding condition or structural health monitoring with integrated piezoelectric transducers are gaining importance. For series applications of composite structures with sensor function, appropriate production technologies are required. Based on the development and production of piezoceramic components, the process-integrated embedding of novel piezoelectric elements in fibre-reinforced polyurethane composites is described. However, in order to achieve an active structure, the piezoceramic components embedded in the composites must be poled. This obstacle is overcome by a poling process that is conducted during the uncured stage of the polyurethane matrix. The new method was experimentally verified. Additionally, a first performance evaluation of sensing properties was done.

1 Introduction

The production of piezoceramic transducers and their integration into composite structures are connected with time and cost consuming processing steps. Therefore, as part of the research activities within the Collaborative Research Centre/Transregio (CRC/TR) 39 (subproject B6) a novel Multi Fibre Injection technology has been developed, which enables high-volume production of composite structures with integrated sensor elements based on fibre-reinforced polyurethane composites [1]. The method is particularly characterized by the process-integrated manufacturing and embedding of sensor elements, thus combining the following production steps: sensor manufacturing, composite manufacturing and sensor integration. As piezoceramic starting components, free-flowing semi-finished products, such as pearls or short fibres, based on lead zirconate titanate (PZT) are used. They can be obtained, for example, from fibre production residues, or manufactured by an adapted fibre spinning process, developed in subproject A1 of the CRC/TR 39.

Using a specially developed MFI processing unit the sensor assembly is realized fully automated by placing a lower electrode onto the mould and subsequently applying the piezoceramic components on this electrode, creating the piezoelectric functional layer [Fig. 1]

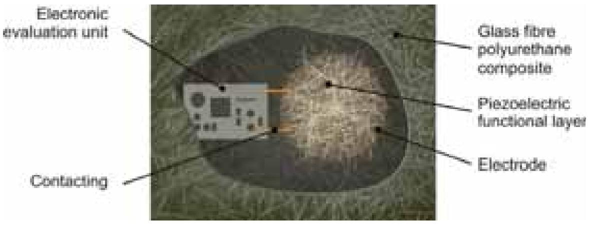

Fig. 1: *Schematic of a fibre-reinforced polyurethane composite with integrated sensor elements*

With placing the upper electrode onto that layer, the sensor assembly is finished. For completely embedding the sensor in the fibre-polyurethane composite, the sensor assembly must be impregnated by the expanding matrix in thickness direction. Therefore, porous electrodes like metal wire meshes are required. During expansion and curing of the fibre-polyurethane mixture, the formation of polymeric layers between electrodes and piezoelectric functional layer may result, which affect the poling behavior of the sensor.

The influence of such insulation layers on the poling characteristics has been studied in [2]. To improve poling of the embedded sensors, an online poling procedure is introduced, which specifically takes advantage of the electric conductivity of the uncured polyurethane matrix, allowing charges to get to the surface of the PZT components.

2 Materials and processing technology

2.1 PZT pearls

PZT pearls of about 1200 µm in diameter are used as active phase to build up the active polyurethane composites (Fig. 2). The PZT pearls are fabricated by a discontinuous spinning method based on a phase inversion process [3]. PZT powder (SONOX® P505, CeramTec GmbH, Germany) is dispersed in a binder solution to form a homogeneous ceramic slurry. It consists of 75 wt.-% PZT powder, 22.3 wt.-% N-Methylpyrrolidone as solvent, 2.3 wt.-% polysulfone as binder and 0.4 wt.-% dispersing agent. The slurry is filled into a cartridge and extruded through a nozzle with 0.41 mm in diameter by means of gas pressure. It is then dropped into a aqueous precipitation bath, which is a non-solvent with regard to the polysulfone binder. Therefore, the binder coagulates by an exchange reaction between solvent and non-solvent, leading into a rigid green body. The distance between nozzle and precipitation bath surface is adjusted to 12 mm to achieve approximately spherical component geometry. The resulting pearls are dried for four hours at 80°C and subsequently sintered for two hours at 1160°C.

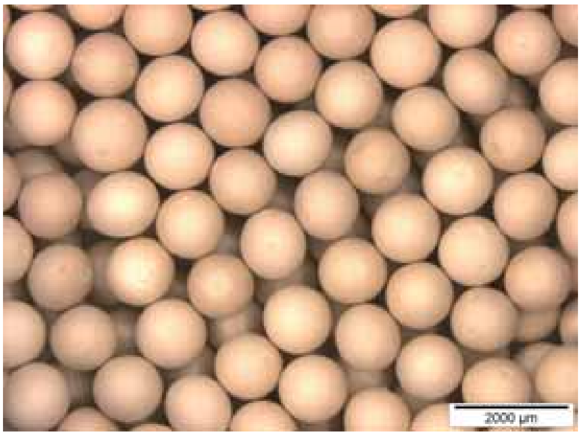

Fig. 2: *PZT pearls with 1200 µm diameter*

2.2 Composite materials and processing

Overall subject of the presented research is the development of active fibre-reinforced polyurethane composites. These are manufactured using a spray coat method, which is characterized by the processing of expandable polyurethane (PUR) in conjunction with a long fibre reinforcement made of glass. Both starting components of the polyurethane - polyol and isocyanate - are mixed in a high-pressure mixing head using the counterflow injection mixing method. The expansion of the polyurethane is realized by the chemical reaction of water and isocyanate. The expansion behavior and the free rise density are determined by the proportion of water in the A-component (Polyol) and the mixing ratio of the two PUR components. The degree of expansion and hence the resulting density of the composite can be influenced by the volume of the mould cavity, respectively the filling degree. In Table 1 the processing data of the used matrix system are summarized.

Table 1: *Processing parameters of used polyurethane matrix material*

Property	***Polyol***	***Isocyanate***
Density [g/cm³]	*1.07*	*1.23*
Viscosity [mPas]	*1600*	*220*
Mixing ratio [per weight]	*100*	*215*
	Mixture	
Starting time [s]	*85*	
Free rise density [g/cm³]	*0.125*	

As reinforcing component, glass fibres specified for cutting processes are used. The assembled rovings have a total linear density of 4800 tex and a linear density of the strands of 90 tex. The rovings are fed to a special cutting unit directly above the mixing head and cut in defined lengths from 12.5 to 100 mm. The chopped fibres are discharged simultaneously with the PUR matrix into an open mould. During the discharge, both the fibre mass content and the fibre length can be varied and thus adapted to the local component stress. After closing the mould, the glass fibre-polyurethane mixture cures in the closed cavity and can be demoulded after a few minutes. Due to the high variability of the process both in terms of the used matrix systems with different degrees of expansion, and with respect to the varying fibre mass content and fibre lengths a wide range of mechanical properties of the composites can be realized.

3 Sample manufacture

3.1 Processing conditions

For the online-poling studies, a sheet die with dimensions of 650 x 650 mm^2 was used; the thickness of the samples to be manufactured was chosen to be 4 mm. The sensor assembly was done manually on the lower mould cavity. Subsequently, the sensor has been back-foamed fully automated with the fibre-polyurethane mixture by means of a robot-guided mixing head spreading the material all over the cavity on a pre-programmed path. All processing conditions (e.g. spraying path, mould temperature) and composite specification have been kept constant during the investigations. After curing, the test specimens were cut out of the composite plates.

3.2 Online poling

Piezoelectric ceramics must be poled to activate the sensing or actuation properties of the material. Even small layers of dielectric matrix material reduce the applied electric field at the embedded piezoelectric components. In order to overcome this problem, different approaches are documented in literature. These include using a very high electric poling field and high temperatures, increasing the contact area between electrode and piezoceramic by sanding or grinding the sample, additional additives such as carbon, semiconductor powder or metal powder to increase the electrical conductivity [4], or electrophoretic orientation of the particles [5]. All approaches have significant disadvantages, such as low piezoelectric performance, high losses or additional process steps in fabrication. In [6], a method is described where the matrix polymer is partially cured until its resistance is in the range of the resistance of PZT, and then poling is conducted.

In this work, a different poling method was developed, tested and verified. Therefore, the process step of poling is implemented into the production process of polyurethane composites. The lower electrode (copper mesh) is positioned onto the heated mould, the PZT pearls filled in as monolayer (see figure 3), and the second electrode mesh placed on top.

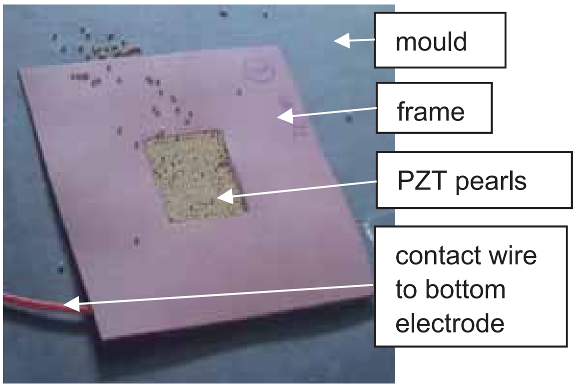

Fig. 3: *PZT pearls in a frame on the bottom electrode mesh in the mould*

Then, the polyurethane is sprayed onto these layers and the mould is closed. After the start time t_{start}, an electric voltage is applied to the electrodes. No additional process steps or additives are needed, saving process time and costs. Figure 4 shows the schematic structure of the online poling of a sample.

Fig. 4: *Schematic structure of a sample (copper electrodes and PZT pearls in polyurethane matrix) and current flow through poling*

Because the polyurethane is uncured or only partially cured, its resistance is relatively low. A current can flow between the electrodes, allowing charges to get to the surface of the PZT even without direct contact of PZT and electrode mesh. The resistance of the polyurethane, which rises with grade of curing, determines the flowing current.

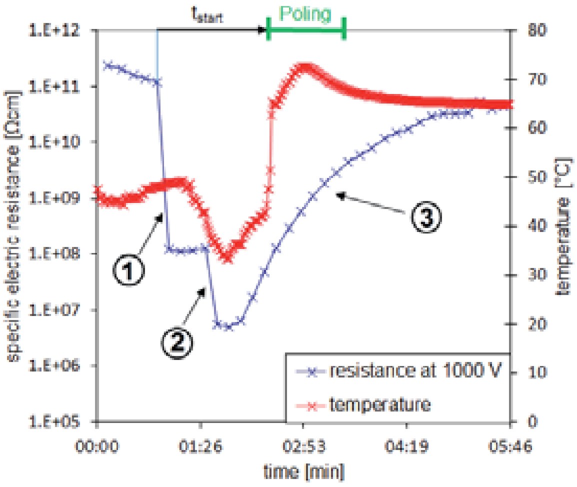

Fig. 5: *Specific electric resistance and temperature over time in the mould during the manufacturing process: 1) spraying of the polyurethane 2) closing of the mould 3) successive curing*

Figure 5 shows the specific electric resistance and temperature over process time. The measurement was conducted with 1000 V measurement voltage to simulate conditions for a poling process. Resistance falls first with spraying of the polyurethane and again with closing of the mould. With ongoing curing of the polyurethane, resistance is rising. Temperature is also influenced by spraying of the polyurethane and closure of the mould. During curing, there is a sharp increase with a peak at about 3 min of process time, caused by the exothermic curing reaction, supporting the poling process additionally by increased temperatures [7,8].

The effective electric poling field between the electrodes was 2 kV/mm and 3.3 kV/mm, and applied for 60 s with different start times t_{start} at which the electric field was turned on.

Few experiments failed due to different damage mechanisms (figure 6) that caused short circuits during poling:

Fig. 6: *Bypass wire (left) and electrical breakdown (right) resulting in unpoled samples*

- No additional insulation of the upper electrode against earth
- small wires of electrode mesh causing a bypass
- Gas bubbles causing electrical breakdown

4 Performance evaluation

To evaluate the poled samples, the piezoelectric charge coefficient d_{33}^* was determined. In a special test set-up (figure 7), a force F is applied to the sample and the response charge Q is measured by using a charge amplifier circuit. The applied forces are in the range of 100 – 140 N.

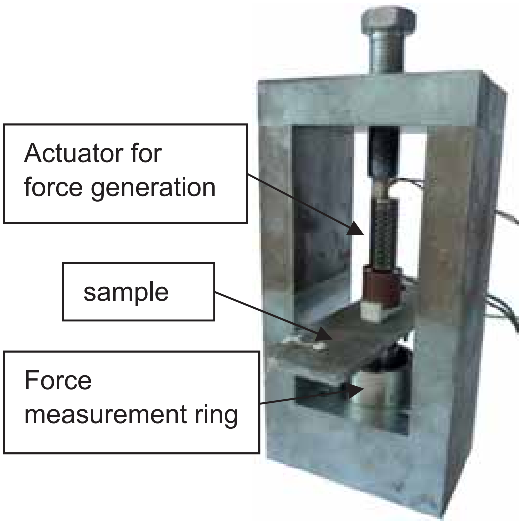

Fig. 7: *Test set-up for determination of the piezo-electric charge coefficient* d_{33}^*

The effective charge coefficient d_{33}^* can be calculated as follows:

$$d_{33}^* = \frac{Q}{F} \qquad (1)$$

The results are shown in figure 8.

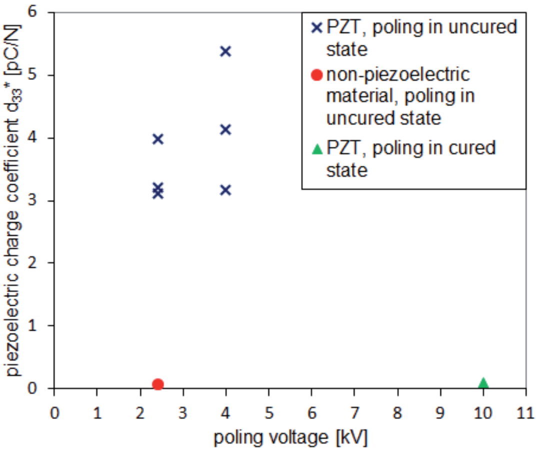

Fig. 8: *Piezoelectric charge coefficient over poling voltage*

For poling the samples in an uncured state of the polyurethane, charge coefficients of 3 - 4 pC/N were achieved with a poling voltage of 2.4 kV, coefficients of 3 - 5.5 pC/N were achieved with 4 kV. To compare the results, a sample was poled after curing. Here, higher electric fields can be applied since the electric resistance and dielectric strength is very high. A charge coefficient of 0.1 pC/N was calculated. In addition, a sample filled with non-piezoelectric pearls instead of PZT was fabricated and poled with 2.4 kV. The resulting noisy response signal was very low and lead to a charge coefficient of 0.08 pC/N. This experiment verifies that the measured signals for PZT-filled samples come from piezoelectric activity.

5 Conclusions

In this contribution, a new process for manufacturing active fibre-reinforced polyurethane composites is described. Adding PZT pearls that act as active component and glass fibres with polyurethane as matrix material, composites are manufactured in a serial process environment. Since poling of the PZT components proved to be an obstacle in the process, special focus is laid on a novel poling method that takes advantage of the electrical conductivity of polyurethane in an uncured or partially cured state. The effective charge coefficient d_{33}^* proves piezoelectric activity with

3 – 5.5 pC/N, which is assumed to meet sensing requirements of lightweight structures.

Further experiments will focus on variation of the poling conditions (electric field amplitude, poling time, start time) in relation to components (copper mesh electrodes, glass fibre content in the polyurethane, PZT component shape) and sample structure.

Acknowledgement

This research is supported by the Deutsche Forschungsgemeinschaft (DFG) in context of the Collaborative Research Centre/Transregio 39 PT-PIESA, subprojects A01, B06 and C03.

Literature

[1] Weder, A.; Geller, S.; Heinig, A.; Tyczynski, T.; Hufenbach, W.; Fischer, W.-J.: A novel technology for the high-volume production of intelligent composite structures with integrated piezoceramic sensors and electronic components. In: Sensors and Actuators A: Physical, 202, 2013, p. 106-110.

[2] Geller, S.; Neumeister, P.; Gude, M.; Tyczynski, T.: Studies on the polarisation behaviour of novel piezoelectric sensor modules, In: Sensors and Actuators A: Physical 218, 2014, p. 162-166.

[3] Hohlfeld, K.; Gebhardt, S.; Schönecker, A.; Michaelis, A.: PZT components derived from polysulphone spinning process. In: Advances in Applied Ceramics 2015; Vol. 114(4), 2015, p. 231-237.

[4] Sa-Gong, G.; Safari, A.; Jang, S. J.; Newnham, R. Poling flexible piezoelectric composites. In: Ferroelectrics Letters Section 5 (5), 1986, pp. 131–142.

[5] van den Ende, D. A.; Maier, R. A.; van Neer, P. L. M. J.; van der Zwaag, S.; Randall, C. A.; Groen, W. A.Sa-Gong, G.; Safari, A.; Jang, S. J.; Newnham, R.: Modeling and characterization of dielectrophoretically structured piezoelectric composites using piezoceramic particle inclusions with high aspect ratios. In: J. Appl. Phys. 2013, 113 (3).

[6] Ainger, F. W.; Garner, G. M.; Goosey, M. T.; Seth, P. N. A.: Improvements in and relating to piezoelectric composites. Applied for by Marconi Gec Ltd, GB; Plessey Co Ltd, GB; Plessey Co Plc, GB. App. no. 8812508, 1992, Patent no. GB000002219129B.

[7] Kounga, A.; Granzow, T.; Aulbach, E.; Hinterstein, M.; Roedel, J.: High temperature poling of ferroelectrics. In: J. Appl. Phys. 104, 2008, 024116.

[8] Marsilius, M.: Schaltverhalten ferro-elektrisch-ferroelastischer Materialien. Dissertation, Technische Universität Darmstadt, Darmstadt, 2011.

Integration of thermoplastic-compatible piezoceramic modules (TPM) in fibre-reinforced polyurethane composites

Gude, M.; Geller, S.; Weber, T.

[1]Technische Universität Dresden, Institute of Lightweight Engineering and Polymer Technology

Abstract

The development of functional elements which are tailored to processes is of increasingly significant importance to generate function integrated components. The thermoplastic-compatible piezoceramic modules under development are suitable for adhesive-free integration into fibre-reinforced polyurethane structures. The novel module design and the roll-to-roll manufacturing process could be adapted in a wide range of carrier film with the focus on a optimally prepared boundary layer. The paper includes experimental studies based on investigations on the boundary layer behavior between matrix-system and carrier film with the aim of an optimal module layout for the integration as sensor or actor. Finally the operation of the functional elements integrated within the manufacturing process would be validated by component testing.

1 Introduction

The most recent production and application method of existing functional modules and adaptive components is characterized by manual adhesive bonding. A common feature of existing patch transducers such as the Macro Fibre Composite (MFC), DuraAct, and Shape Fiber Composite (SFC) is that they are based on thermosetting carrier films (primarily polyimides) which represent the outer surface in contact with the composite structure. Current applications require modules to be manually bonded to the composite structure using an additional adhesive. The module manufacturing process also continues to require significant manual effort and the adhesive mounting of module components.

Furthermore, the manual effort involved in the manufacturing makes the integration of existing modules expensive and disadvantageous for high-volume applications in sectors such as the automotive industry. A transition from this assembly-oriented approach to technology-oriented actuator integration could initiate high-volume production of intelligent lightweight structures.

The development of active composite structures for wider fields of applications and new markets is being supported by the design of novel piezoceramic modules and associated process technologies which are specifically tailored to fibre-reinforced composite structures and their respective manufacturing processes.

This papers deals with the manufacturing and integration of novel thermoplastic-compatible piezoceramic modules (TPM) within fibre-reinforced polyurethane composites. This technology is predestined for the integration of such functional elements due to their specific advantages such as moderate processing conditions and superior adhesion properties.

2 Design and manufacture of TPM

To realize a high volume manufacturing process, a high degree of automation becomes necessary. Therefore a tailored manufacturing process was developed based on the roll-to-roll technology [1].

The novel thermoplastic-compatible piezo-ceramic modules (TPM) contain of thermoplastic carrier films, which are especially adapted for integration within the production process of fibre-reinforced composite. Actually a polyamide 6 (PA6) foil is in use, where PA6 is a representative of common technical polymers. The experimental integration studies within this paper focus on PA6 foil material.

Fig. 1 a) shows the TPM manufacturing process that starts with the electrode application. This takes place by an adapted additive technology like screen printing, which allows electrode thicknesses between 5 to 10 µm [2]. The first step is followed by the assembly and converting process of the TPM using an adapted hot-pressing technology. This part is focusing on the exact positioning of the piezoactive core between the functionalized foils by means of web positioning. In subsequent steps, the TPM are contacted and polarized in order to achieve the required piezoelectric properties and thus to ensure the functionality of the TPM.

Within this paper the experimental studies center on the integration of such TPM in composite foam structures.

3 Materials and processing technology

Within subproject B6 of the CRC/TR 39, research is focused on integration of TPM into fibre-reinforced polyurethane composites. For the investigations presented in this contribution, the long fibre injection (LFI) process is used for manufacturing glass fibre-reinforced polyurethane composite structures with integrated TPM. The LFI spray coat method is characterized by processing of reactive two-component polyurethane (PUR) systems in conjunction with long glass fibre reinforcement [3, 4]. Generally the used PUR material is expandable which enables production of lightweight components with very low densities. The two starting components of the polyurethane - polyol and isocyanate - are mixed in a high-pressure mixing head using the counterflow injection mixing method. Thereby short cycle times and thus capability for high volume production are provided. As reinforcing component, glass fibre rovings are fed to a cutting unit above the mixing head and chopped to defined lengths between 12.5 and 100 mm. Both the PUR matrix and the chopped fibres are discharged simultaneously into an open mould by means of a handling robot. During discharge both the fibre length and the fibre mass content can be locally varied and thus adapted to the component stress.

When the spraying operation is finished, the mould it is closed and the fibre-polyurethane mixture cures within a few minutes. Due to the versatility of the polyurethane matrix systems with regard to resulting densities as well as high process variability in terms of fibre length and fibre mass content LFI composite components with a wide range of mechanical properties can be realized. Furthermore, taking advantage of the good adhesion properties of polyurethanes, thermoplastic films can be directly back-foamed in the LFI process. This is used for example in the production of high quality exterior components of passenger and commercial vehicles [5 – 8].

4 Integration studies

4.1 Sample manufacture

The composite structures are manufactured using the automated long fibre injection (LFI) process and a sheet die with dimensions of 650 x 650 x 5 mm. For the investigations presented, the TPM to be integrated is placed centric onto the lower mould just before the manufacturing process and subsequently back-foamed with the glass fibre-polyurethane mixture (Fig. 1b)). Composite samples of 3 specifications with varying amount of PUR and resulting densities at constant fibre mass content have been prepared. Since the dimensions of the cavity have been kept constant through all the investigations, the density is defined by the amount of the discharged PUR and glass fibres, resulting in different degrees of expansion. The fibre length has been set 25 mm for all samples.

The aim of this adapted process is a direct, non-destructive integration of the functional piezo module within a highly automated manufacturing process of structural parts.

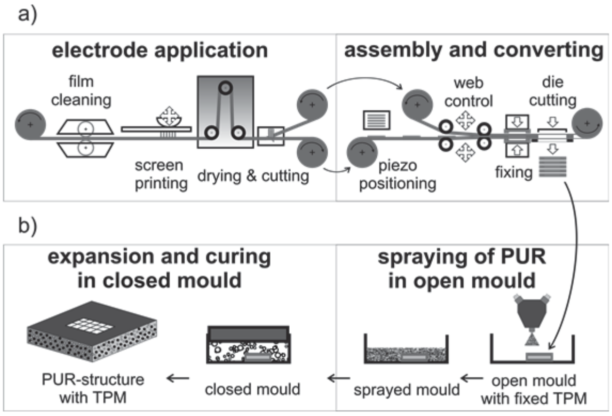

Fig. 1: *Scheme of the TPM manufacturing (a) and the adapted LFI process (b)*

4.2 Quality assurance

Prior to the functional testing of the back-foamed TPM, investigations with regard to their structural integrity as well as the boundary layer between the TPM and the composite structure have been carried out. Thus, the TPM have been analyzed before and after embedding by means of X-ray technique in order to detect any damage as a result of the manufacturing process. In corresponding integration studies, different processing conditions with respect to glass content and amount of matrix as well as resulting expansion pressures and reaction temperatures were used. The analysis of process-related stresses shows maximum cavity pressures of 2.9 bar and maximum temperatures of 100 °C. Due to these moderate processing conditions, no damage to the TPM could be detected in the X-ray studies (Fig. 2).

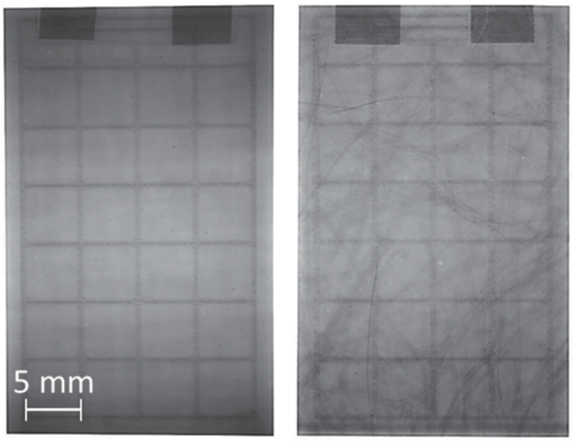

***Fig. 2:** X-ray scan of an integrated TPM before (left) and after embedding (right)*

The boundary layer between TPM and composite is analysed by means of light microscopy. In Fig. 3 a corresponding cross-section is illustrated were both the fibre composite with cellular matrix and filament cross-sections as well as the structure of the TPM with thermoplastic carrier films and piezoceramic functional layer are clearly visible. In the area of the boundary layer a compact connection of the thermoplastic films without air inclusions can be seen, which is necessary for a good adhesion.

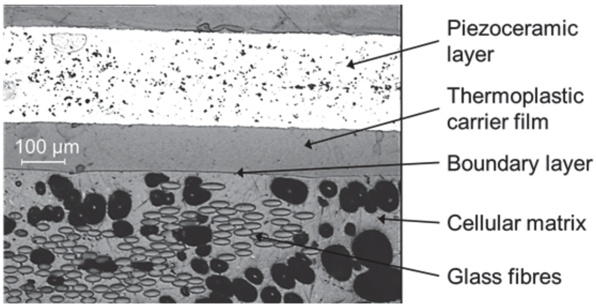

***Fig. 3:** Micrograph of the boundary layer between glass fibre-reinforced polyurethane composite and back-foamed TPM*

4.3 Proof of functionality

Laser Scanning Vibrometry

In order to proof the functionality of the TPM and its coupling to the composite structure, the characteristic resonance frequencies of the samples have been determined using a laser scanning vibrometer (LSV) (type PSV-400 produced by Polytec). The laser scanning vibrometry enables contactless measurement which helps to avoid distorting the mechanical properties of the investigated object, for example caused by the additional mass of typically used vibration sensors. The excitation of the plates was realized by the back-foamed TPM. A harmonic chirp voltage signal from 0 V to 360 V was applied to the TPM in a frequency range of 0.01 kHz to 0.2 kHz with a resolution of 0.25 Hz. The LSV has been positioned normal to the analysed plate because of the direct proportionality of the LSV output signal to the velocity of the targeted surface along the laser beam direction. For the scanning of the surface a pattern of 11 x 11 discrete measuring points was used. The plates have been hung vertically using thin and light ropes.

In Fig. 4 the determined spectrum of the surface velocities in dependency of the excitation frequency is illustrated. The peaks for the resonance frequencies are clearly recognizable.

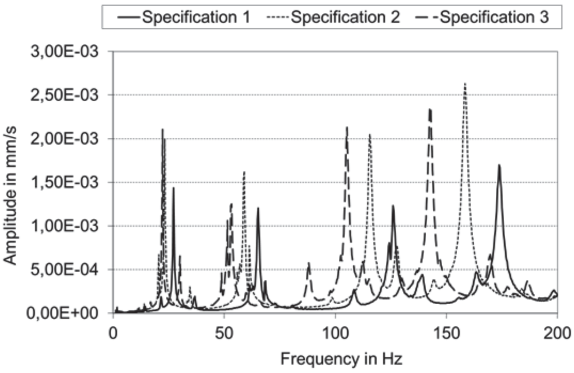

***Fig. 4:** Determined spectrum of surface velocities for different composite specifications*

Due to the clear curve progression a coupling of the TPM to the structure is given. Furthermore, the shift of the resonance frequencies to higher values corresponds to the specification of the investigated samples. Hence, functionality and excitation of the TPM as well as coupling to the composite structure could be proven.

Optical deformation analysis

In order to underline the previous investigations an optical deformation analysis of the sample with embedded TPM was realized. The examinations are performed with a test setup including function generator, amplifier and Digital-Image-Correlation (DIC) -System (5M-ARAMIS-system). Fig. 5 a) shows the embedded sample prepared for the DIC with the typical stochastic pattern. The TPM was driven with a triangle signal with an amplitude of 180 V and an offset of 180 V at a frequency of 100 mHz. The strain field (Fig.5 b)) shows the characteristic performance of the structural part with embedded TPM at maximum voltage in y-direction.

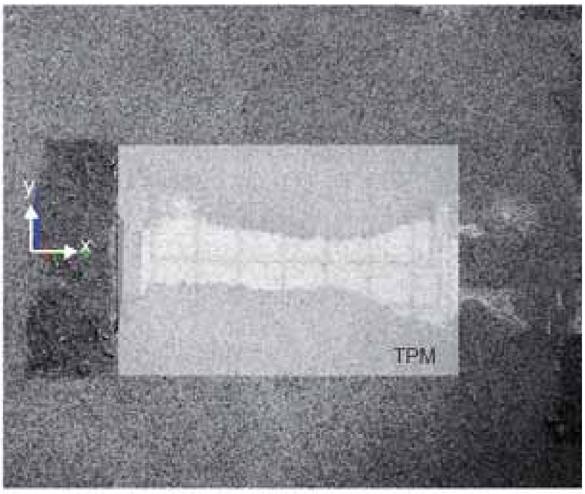

a) Embedded sample

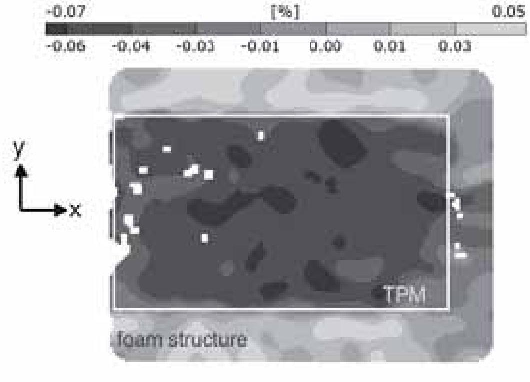

b) Strain field in y-direction

Fig. 5: *Image of the embedded sample (a) and the appropriate strain field (b)*

Due to the use of a TPM with d_{31}-characteristic the module contracts with negative strain in x- and y-direction.

The strain behaviour of the bordering structure gives inference to the coupling of the embedded module. At the surface of the module the compression zone is clearly detected. And also the elongation of the bordering foam structure can be detected in a good manner.

Fig. 6 shows the quantitative values of the emerging material behaviour under contracting. The strain values of both areas are in the same range. Due to this a good coupling between the functional module and the structural material can be assumed.

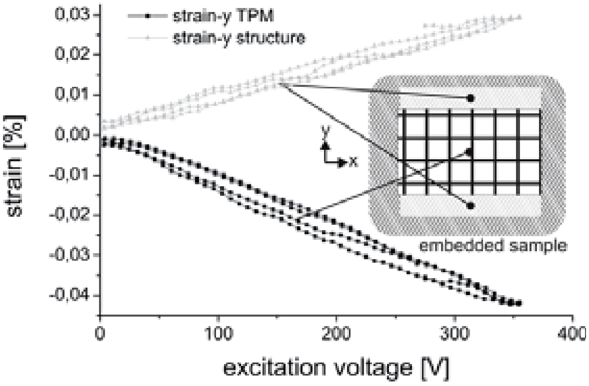

Fig. 6: *Quantitative performance of different areas of the embedded sample*

5 Conclusions

Using the long fibre injection process, piezoceramic modules with thermoplastic carrier films have been integrated into fibre-reinforced polyurethane composites. Due to moderate processing conditions, gentle embedding of the TPM without damage to the piezoceramic functional layer is provided, which could be verified by X-ray analysis and microscopy. Further, the boundary layer between thermoplastic films and thermoset composite does not show any indication of delamination, e.g. caused be the cellular matrix or unwetted fibres. Thus, the adhesion as well as coupling of the module to the composite structure is given which could be shown in initial studies on the functional capability. By means of laser scanning vibrometry and digital image correlation (ARAMIS), the transmission of excitations from the piezoelectric module to the composite structure has been proven.

Acknowledgement

This research is supported by the Deutsche Forschungsgemeinschaft (DFG) in context of the Collaborative Research Centre/Transregio 39 PT-PIESA, subproject A05 and B06.

Literature

[1] *T. Heber, M. Gude, W. Hufenbach, Production process adapted design of thermoplatic compatible piezoceramic modules, Composites: Part A 59 (2014) 70-77*

[2] *Hufenbach, W.; Gude, M.; Geiger M, Schmidt M., Neugebauer S.: Auslegung und Fertigung von thermoplastverbund-kompatiblen Piezokeramik-Modulen für adaptive Leichtbaustrukturen 17. Symposium Verbundwerkstoffe und Werkstoffverbunde; Wiley-Vch; 2009*

[3] *Frehsdorf, W.; Söchtig, W.: High Requirements – Low Investment Costs. Kunststoffe plast europe, Vol. 91 (2001), Issue 3, p. 23-25*

[4] *Renkl, J.; Söchtig, W.: LFI-PUR - The Process for High-Quality, Long-Glass-Fiber-Reinforced Polyurethane Parts. In: 5th Annual SPE Automotive Composites Conference 2005, Troy, USA, 12.-14. September 2005, on CD*

[5] *Häberle, H.; Mohr, R.: Kühlerblende in Hochglanz-Optik. In: Kunststoffe im Automobilbau. Düsseldorf: VDI Verlag, 2008, p. 221-247*

[6] *Rosenberger, J.: Class-A Folie PUR hinterschäumt für Nutzfahrzeug-Außenteile. In: PUR 2009. Düsseldorf: VDI Verlag, 2009, p. 21-32*

[7] *Rau, H.; Bachsteffel, J.: PUR-Verbundbauteil mit hochwertiger Oberfläche für Innen- und Außenanwendung. In: Kunststoffe im Automobilbau. Düsseldorf: VDI Verlag, 2004, p. 229-243*

[8] *Stratton, D.; Platte, P.; Rocco, D.: A Modular Automotive Roof System Design Concept Based on Polyurethane Composite Technology. In: 6th Annual SPE Automotive Composites Conference 2006, Troy, USA, 12.-14. September 2006, p. 475-491*

Smart machine elements by rotary swaging - Manufacturing and Applications

Krech, M.; Groche, P.

Institute for Production Engineering and Forming Machines (PtU) TU Darmstadt

Abstract

This contribution presents a two-stage rotary swaging process, which allows integration of functional elements for load and condition monitoring of hollow tubular machine parts. The forming process is adjusted in order to guarantee a damage-free integration of the fragile functional elements. An effective utilization of the sensory compound requires the elements to lie in the path of forces which is ensured by a pretension. In order to set up the targeted pretensions, the integrated sensory elements itself can be utilized during the forming process. Two monitoring applications illustrate the coupling quality of the manufactured smart machine elements.

1 Introduction

There is a high demand for smart, sensing and actuating, networked machine elements with additional benefits. By ongoing miniaturization of sensors, electronic components and networking technologies, the possibilities for highly integrated structures with supplemental intelligence are arising. Two major problems in the design phase of load bearing systems are uncertain, fluctuating stress collectives in the utilization and quality defects in a globalized production. As a result, systems have to be oversized in order to avoid rare, but nevertheless dangerous or costly dysfunctions.

Smart machine elements can help to reduce this uncertainty by monitoring and logging their stresses and provide information about their conditions. Thus it is possible to estimate the remaining lifetime and control maintenance intervals of the intelligent parts. [1]

A widespread application of smart machine elements requires a cost efficient production which can potentially be accomplished by upgrading existing processes. A promising approach is to combining the joining operation of functional elements with the forming operation of the work piece. Examples can be found in micro-extrusion of piezoelectric fibres [2], deep drawing of Piezo-Metal-Composites [3], and joining by rotary swaging [4-6].

In general, these combined forming processes are characterized by a low demand of joining elements and offer the possibility to achieve a compact coupling of the load bearing structure and the functional element. Unused cavities that are no longer available for other processes after forming can be utilized during a simultaneous joining and forming process. The products resulting from this operation are characterized by a high robustness against external influences since the integrated elements are placed on a protected side of the product.

In this contribution, the manufacturing process of function integrated machine elements by a two-stage rotary swaging process is presented and two different kinds of monitoring applications are given. In a first application, the sensory abilities of the functional elements are used to measure axial loads. A second application illustrates the use of integrated piezo elements for “Structural Health Monitoring” applications.

2 Sensory machine parts by means of rotary swaging

Rotary swaging is an incremental cold forming technique where the net shape of a part is reached in many small forming steps. Four oscillating tools reduce the diameter of a tubular work piece with alternating strokes. A rotation between the tools and the work piece enables a high circularity tolerance of the produced axial symmetric parts. Rotary swaging is often highlighted for its possibility to offer a large-scale production of lightweight machine parts like hollow shafts or shock absorbers. Because of the high material usage, this forming method is cost and resource efficient. In this forming method, compressive stresses elevate the formability of the material with added advantages of cold work hardening and homogeneous grain structure. As a result, high static and fatigue strengths of the work pieces can be achieved. [7-9]

The investigated sensory machine parts in this contribution consist of an aluminium tube and a functional element, which is placed inside the tube in the path of forces. For this, the creation of an undercut is necessary. A mandrel is used to reduce the tube diameter in the area where the functional element is placed subsequently. By this, a preform is created out of the semi-finished tube (Fig. 1a). In the next step, the functional element is inserted into the tube and is placed against the contact area. End caps are used on both sides of the functional element to protect them from high radial forming forces and to help setting-up a pretension.

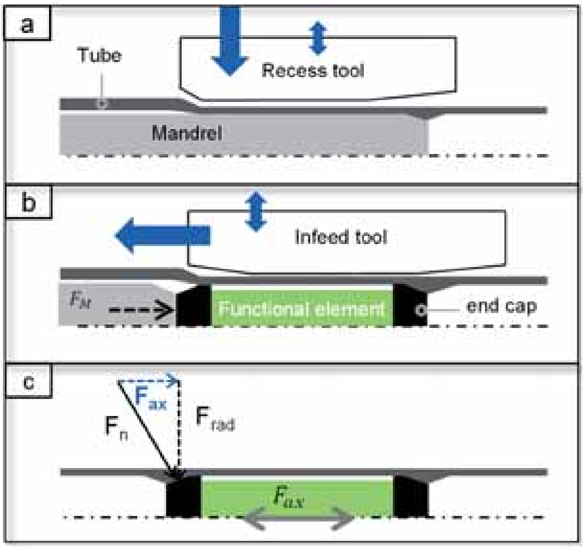

Fig. 1: Schematic of the two-stage rotary swaging process

The forming process is continued with an infeed swaging tool (Fig. 1b). The material flow leads to an adaption of the tubes inner contour to the given chamfer of the end cap. Thus, axial force components are acting on the inner parts during the tool strokes. This leads to compressive stresses in the functional element and tensile stresses in the corresponding region of the tube. After the radial and axial spring-back of the formed tube, a pretension $F_{pretension}$ remains in the functional element.

The damage-free integration and generation of a pretension places several demands on the geometry of the preform and the end caps, the material combination, as well as the process parameters. The interface between the tube and the functional element, in this case realized by the end caps, needs to have a specific chamfer or curvature, in order to generate axial forces through the material flow of the tube. In [6] different end cap angles and preforms are investigated experimentally. It is shown that only an appreciable material displacement offers the possibility to create a pretension. On the one hand, no pretension will occur, if the angle of the inner shoulder, which is adjusting in an unblocked material flow, is smaller than the end cap angle. On the other hand, too small chamfer angles lead to high unwanted opposing frictional forces, which also prevent the generation of a noticeable pretension.

The axial forces which occur during forming are not supposed to exceed the load capacity of the sensitive elements during any time of the process. Otherwise there is a risk of damage to the functional element or depolarization in case of a piezo stack actuator. In Fig. 2, a characteristic force curve, recorded by a strain-gauge based sensor element, is illustrated. A small telemetry unit is attached to the end of the rotating work piece and connected to the internal sensor element in a half bridge circuit.

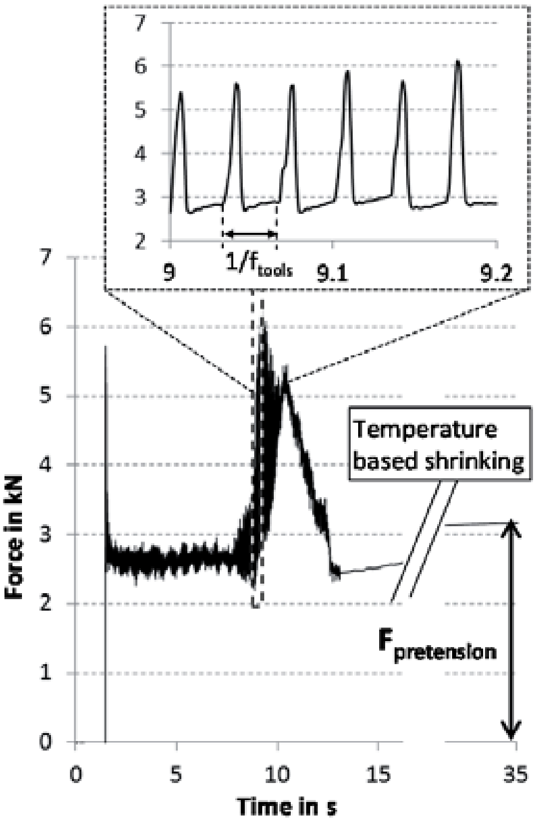

Fig. 2: Exemplary axial force curve of the joining process

A mandrel force is applied and released in second 2 and 13, respectively. This ensures an exact positioning and pre-compression of the functional element. A global peak of the force curve arises between second 8 and 12, when the material flow adapts the geometry of the left end caps chamfer. The single tool strokes of the forming process are manifesting as force peaks.

They are occurring in the same frequency as the tool movement and illustrate the incremental character of this forming process.

At the end of the forming process a shrinking of the deformation-heated tube material is observed, which leads to an additional rise of the pretension. The strain-gauges are adapted to the thermal expansion coefficient of the sensor element and are therefore compensated for an apparent thermal expansion. After equalization of temperatures the remaining pretension in this case is 3.2 kN, while the maximum force reaches just above 6 kN.

A different design of smart machine elements examined in this contribution makes use of a piezo stack actuator. The stiffness and external dimensions of the short-circuited piezo are the same as the drilled aluminum strain-gauge element. Even though the manufacturer states a maximum load capacity of 16 kN, [10], an adaption of the end cap geometry is necessary in order to join the brittle and sensitive piezo ceramics in the above described way.

Damaging bending moment can, inter alia, occur because of imperfect alignments, warped semi-finished parts and the asymmetrical tool strokes. The curvature of the flat end caps (Fig. 1) also leads to a concave contact zone which results in a high edge pressure of the piezo ceramic actuators. This may lead to chipped off edges and cracks, which has to be avoided. For a damage-free integration, stiffer end caps and a spherical headpiece were used to reduce bending moments and edge pressure (Fig. 3). Another advantage is the higher transmission behaviour, which is useful for active applications.

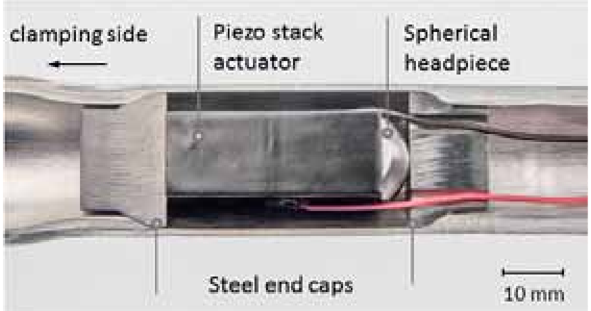

***Fig. 3:** View cut of an integrated stack actuator with spherical headpiece*

3 Utilization of integrated functional elements during the production

The usage of the sensory faculty can be helpful in order to monitor manufacturing processes. While measurement of external machine parameters does not allow an evaluation of the internal stress state, the sensors itself can be used to gain this information online. Possible quality inaccuracies of the semi-finished parts may lead to an inadequate pretension or bending stresses inside the sensor element. Even in subsequent processing steps, it is possible to monitor forces, bending moments and torque through the work piece itself. An integrated process monitoring can permit a higher sensitivity for work piece defects and is able to allow an uninterruptible logging of loads during the complete production process. For this, it is necessary to equip the hollow work pieces with electronic devices and an energy supply. This generates an enclosed unit which is robust against any kinds of environmental influences during the production process.

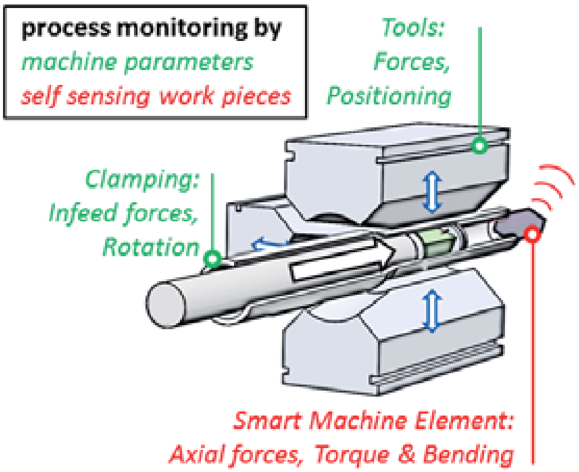

***Fig. 4:** Possibility for Process Monitoring by machine parameters and self-sensing work pieces*

4 Utilization of integrated smart machine parts for load and structural health monitoring

4.1 Performance of axially loaded sensory rods

A monitoring of the structural loads is required in many fields of mechanical engineering. Within the scope of the collaborative research center 805 „Control of Uncertainty in Load-Carrying Structures in Mechanical Engineering“, a demonstrator consisting of several tetrahedron rod structures is designed. The reliability of this modular, active spring-damper-system relies on the stability of its skeletal truss structure. The presented smart rods are used to monitor the distinct bar forces during assembly and usage of the system. For this, the accuracy and linearity of the sensor has to be assured at any time. It is obvious that the pretension inside the sensor element decreases by tensile bar forces, while compressive bar forces increase the pretension. The distribution of forces emerges from the stiffness ratios of the tube and the internal elements. In this case, a high stiffness ratio is given by a cubic sensor element and a small wall thickness. In order to minimize parasitic bending influences, flexible end caps are introduced.

In the compression-tensile machine Zwick Allround-Line 100 kN, axial tension and compression forces are applied (Fig. 5). Two opposite strain-gauges on the cubic sensor element are summed up in order to obtain the axial strains acting on the rod.

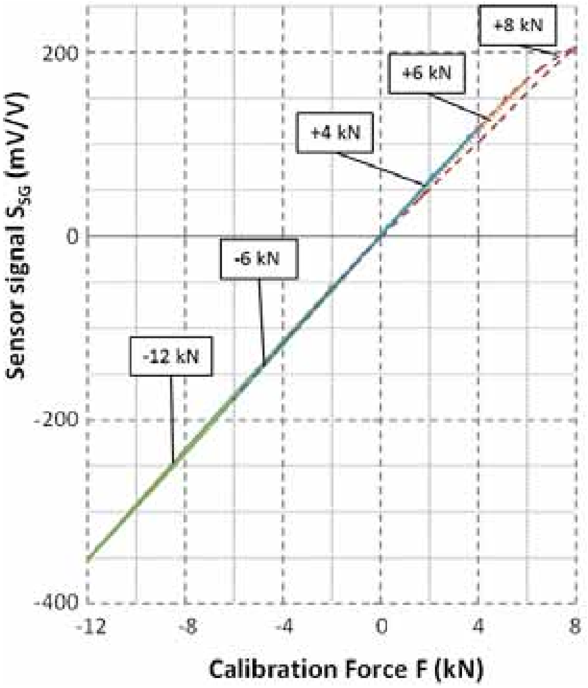

Fig. 5: Calibration curves of a strain-gauge based sensory rod

It can be stated that there is a high linearity up to 6 kN in both, compression and tensile region. With an increase in tension, the pretension of the sensor is reduced significantly, resulting in a hysteresis in the tensile region from about +6 kN. The +8 kN curve shows a smaller slope at high tensile forces which indicates that the sensor is increasingly removed out of the path of forces.

The given sensor design can be used reliably in the range of +6 kN up to at least -12 kN. The limitation under compression load is the plastification of the internal elements or a buckling of the rod itself. In order to achieve a higher usability in tensile regions, it is also possible to adapt the stiffness ratios, which leads to smaller sensitivities, but higher operational ranges.

4.2 Structural Health Monitoring

The possibility to utilize the presented function integrated machine elements for monitoring its state is demonstrated with the electromechanical impedance method [11]. For this purpose, a rotary swaged rod with an integrated piezo stack actuator and spherical headpieces (Fig 3) is used. The piezo is stimulated at varying frequencies and the occurring coupled electro-mechanical impedance course is determined as a function of the excitation frequencies. The pretension of the integrated piezo stack actuator leads to a high-quality coupling between the functional material and the metallic structure. Damages in the structure can therefore be identified by changes in the impedance signature (Fig. 6).

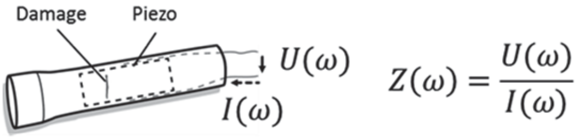

Fig. 6: Structural Health Monitoring by coupled electro-mechanical impedance method

For this investigation a high precision impedance analyzer Wayne Kerr 65120B with an AC drive level of 1 V is used. The impedance signature is determined with a free and unstressed rod at the beginning (see Fig. 7). An intentional crack of around 8 x 1 mm² is induced in the aluminum tube. The signature pattern of the damaged rod shows a distinct deviation to the initial state in the frequency range of 45 - 55 kHz.

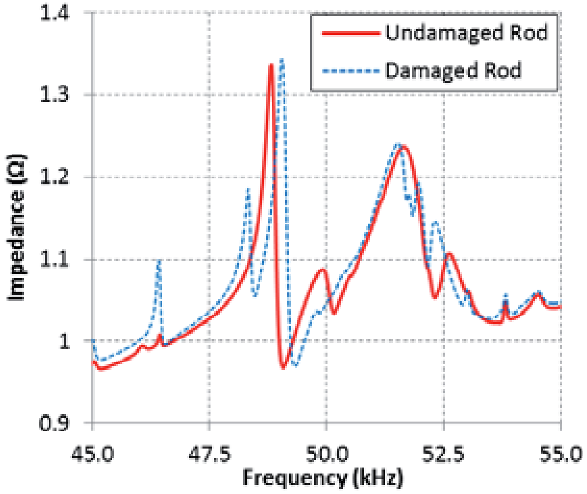

Fig. 7: Impedance curves of an undamaged and damaged rod

Because of the high excitation frequency, even small changes in the structure affect specific regions of the impedance curve of the coupled electro-mechanical system. This can help to identify forthcoming failures at an early stage or to adjust maintenance intervals according to the actual condition of a machine element.

5 Conclusions

In this paper, the manufacturing process of smart machine parts by rotary swaging is illustrated and different applications are demonstrated. It is shown that the integration of the functional elements comes with extended requirements for the forming process. Not only the tolerances of the work pieces net-shape have to be achieved, but also the desired pretension of the elements needs to be adjusted. Thereby the load capacity of the functional element must not be exceeding at any time of the process. For this purpose, the possibilities of monitoring axial forces during the process and detecting process failures are illustrated. The manufactured smart structures can offer many advantages to different fields of application. Compared to differentially built smart components, the presented highly integrated structures require less elements, less process or assembly steps and provide a high environmental protection. The first presented use case is a sensory rod which is able to sense axial forces in a wide range due to its pretension. The limitations of use in this case are nonlinearities which occur when the pretension drops significantly due to tensile rod forces. The possibility to utilize function integrated machine elements for methods of “Structural Health Monitoring” is presented by illustrating the high sensitivity of the different electro-mechanical impedance curves which are affected by the structure’s state.

6 Acknowledgements

The investigations presented in this paper were carried out within the research project B4: ‘‘Integration of Functional Materials’’ of the Collaborative Research Centre 805 ‘‘Control of Uncertainties in Load-Carrying Structures in Mechanical Engineering’’ (CRC 805). The authors would like to thank the German Research Foundation (Deutsche Forschungsgemeinschaft DFG) for funding this research.

Literature

[1] *Denkena, B.; Mörke, T.; Krüger, M;, Schmidt, J.; Boujnah, H.; Meyer, J. et al.: Development and first applications of gentelligent components over their lifecycle. In: CIRP Journal of Manufacturing Science and Technology 7, 2014, p. 139–150*

[2] *Drossel, W.-G.; Hensel, S.; Nestler, M.; Lachmann, L.; Schubert, A.; Müller, M.; Müller, B.: Experimental and numerical study on shaping of aluminum sheets with integrated piezoceramic fibers. In: Journal of Materials Processing Technology 214, 2014, p. 217–228*

[3] *Drossel, W.-G.; Hensel, S.; Nestler, M.; Lachmann, L.: Evaluation of Actuator, Sensor, and Fatigue Performance of Piezo-Metal-Composites. In: IEEE Sensors J. 14, 2014, p. 2129–2137*

[4] *Groche, P.; Türk, M.: Smart structures assembly through incremental forming. In: CIRP Annals - Manufacturing Technology 1, 2011, p. 21–24*

[5] *Groche, P.; Brenneis, M.: Manufacturing and use of novel sensoric fasteners for monitoring forming processes. In: Measurement 53, 2014, p. 136–144*

[6] *Groche, P.; Krech, M.: Integration of functions through rotary swaging – New possibilities for the monitoring of states and loads in tubular machine elements. In: New Developments in Forging Technology, Fellbach 2015*

[7] *Dietrich, A.; Schuiki, M.; Haberer Ch.; Eichlseder, W.: Einfluss der Umformung und der Wärmebehandlung auf die Lebensdauer rundgekneteter Getriebewellen. In: 26. Jahrestreffen der Kaltmassivumformer, Düsseldorf, 2011*

[8] *Grupp, P.: Neueste Entwicklungen für Leichtbauinnovationen in der Getriebeproduktion. In: 4th International Conference on Accuracy in Forming Technology, Chemnitz, 2012*

[9] *Müller, F.: Endkonturnahe Formgebung von Aluminium Teilen durch Rundkneten. In: Umformen von Aluminium im Automobilbau, Bad Nauheim, 1999*

[10] *Datasheet, Piezomechanik GmbH, Piezo Stack Actuator PSt 150/14x14/40, http://www.piezomechanik.com, 28.07.2015*

[11] *Park, G.; Inman, D.; Sohn, H.; Farrar, C.R.; Inman, D.J.: Overview of Piezoelectric Impedance-Based Health Monitoring and Path Forward. In: The Shock and Vibration Digest, v.35, no.6, 2003, p.451-463*

Local pre-curing of an adhesive for the fabrication of shaped piezo-metal-compounds

Drossel, W.-G.[1]; Müller, R.[1]; Ihlemann, J.[2]; Rudolph, M.[2]; Hensel, S.[1]; Nestler, M.[1]

[1]Fraunhofer Institute for Machine Tools and Forming Technology IWU, Chemnitz
[2]Department of Solid Mechanics, Faculty of Mechanical Engineering, Chemnitz University of Technology

Abstract

In this contribution experimental and simulative aspects of a novel method for the production of piezo-metal-compounds are presented in order to enhance the series capability of their former manufacturing process. These compounds are sandwich constructions with a piezomodule between two aluminum sheets. Until recently a still liquid adhesive surrounded the piezomodule to protect it from damage during forming of the compound and an already solidified adhesive in the outer regions assured the patch fixation. Now the studied novel method employs only one adhesive which takes over both functions at the same time. In order to assure this double function a local pre-curing is pursued. The paper focuses on the local activation of the curing reaction of adhesives using higher temperatures. Hence, a device with a heating and a cooling zone was employed to adjust different temperature fields within one bonded sandwich sheet. Finally, sandwich compounds with partially cured and partially liquid areas of adhesive are manufactured. Moreover, a thermo-chemically coupled continuum mechanical model for adhesives is implemented into ANSYS® and allows for finite element analysis of this spatially graded curing with its heat flow caused by both, local activation and exothermal reaction heat. Hence, alternative production strategies can be evaluated at an early stage of the process development.

1 Introduction

Aluminum sandwich parts with integrated piezomodules offer a high lightweight potential and a sensor and actuator functionality. They can be used for health monitoring or a reduction of acoustic noise, see for instance [1]. State of the art production method is the subsequent application of piezomodules on formed sheet metal parts. However, this subsequent application is characterized by a low potential for automation, a low level of protection for the piezomodule against external mechanical and chemical influences as well as high costs. Consequently, a new process chain was developed. The integration of piezomodules in aluminum based sandwich parts by bonding was already presented in earlier studies [1, 2]. Such sandwiches exhibit a good formability, ensured by an uncured liquid adhesive, surrounding the piezomodule and allowing a relative movement between piezomodule and sheet metal. A second, faster curing adhesive was used to provide a fixed connection between the two sheet metals in the outer area [2]. Fig. 1 depicts the application of a piezomodule (here a Macro-Fiber-Composite) and the two adhesives on the basic sheet.

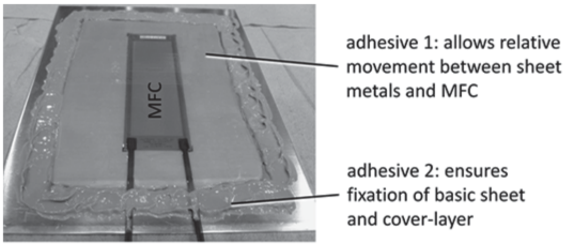

Fig. 1: *Manufacturing of a sandwich compound with integrated Macro-Fiber-Composite (MFC). Two different adhesives are required to ensure the formability of the compound without a leakage of adhesive [2].*

Aiming on higher levels of automation during the manufacturing of the semifinished part, the authors propose a substitution of the two adhesives by only one adhesive and a local pre-curing strategy. The new process chain is depicted in Fig. 2. At first the sandwich is build up with only one adhesive between basic sheet and cover sheet. Before the forming operation, the adhesive is locally cured, e.g. with a thermal treatment, in the outer regions. After forming, curing of the whole compound takes place.

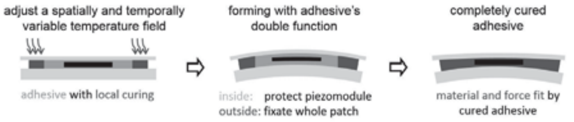

Fig. 2: *Principle manufacturing process for piezo-metal-compounds via spatially and temporally variable temperature field.*

An accelerated curing of adhesives was already presented in [3], where an induction heating device was used to shorten the curing time of a room-temperature curing paste adhesive. A grading of joints was performed in [4], in order to improve the joint strength using an induction heater. A method for a local and fast heat input is presented in [5], where a laser beam is employed. It is used for bonding plastic materials. Within this paper the local hardening of adhesive is used to ensure the double function of the adhesive as shown in Fig. 2. In the following sections experiments as well as modeling and simulation aspects are presented, providing the base for a better understanding of this complex manufacturing process.

2 Experiments

Experiments were performed aiming on a local pre-curing of the adhesive. Hence, a tool-setup enabling water-cooled and electrically heated areas was constructed and experimentally installed in a material testing machine (Fig. 3).

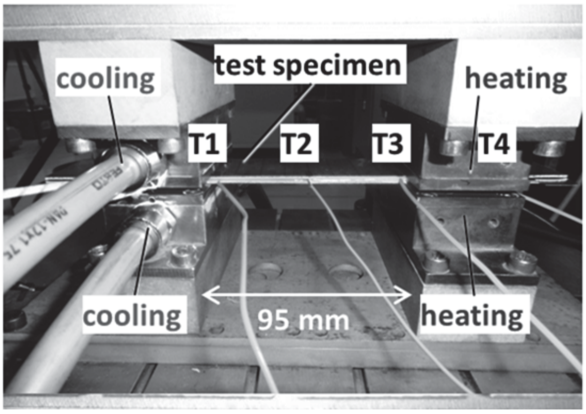

Fig. 3: *Tool-setup for local heating and cooling. Water cooled elements are on the left and electrically heated elements on the right side. The distance between heating and cooling areas is 47 or 95 mm. Temperature sensors are integrated in the adhesive layer at different positions (T1…T4).*

The water-temperature is adjusted at 20±2 °C with an industrial water cooler device. The heating elements (Fig. 3, right) are electrically heated with flexible tubular heating elements. They allow for a uniform surface temperature in a range of 30 °C to 450 °C. Cooling and heating elements have the same dimensions of 80 mm x 45 mm and are placed below and above the test specimens in order to ensure a uniform temperature field. The distance between heating and cooling elements is 47 mm or 95 mm. The specimens consist of two aluminum sheet metals (EN AW 5083) with dimensions of 240 mm x 40 mm x 1.5 mm. Between the aluminum sheets is an adhesive layer with a thickness of 0.5 mm. Manufacturing of the specimen takes place with application of adhesive on the basic sheet, the integration of 0.5 mm spacers in the border area and the application of the cover sheet metal. Inside the testing machine the sandwich material is pressed to the required thickness of 3.5 mm in total. Fig. 4 shows the basic aluminum sheet with an adhesive bead and the cover sheet before application. On the cover sheet the areas for cooling (left side), heating (right side) and in between the area with the highest temperature gradient are marked for a specimen with a tool distance of 47 mm. These samples are designed for a later peel test, which is performed to experimentally test the mechanical properties dependent on the adhesive curing progress.

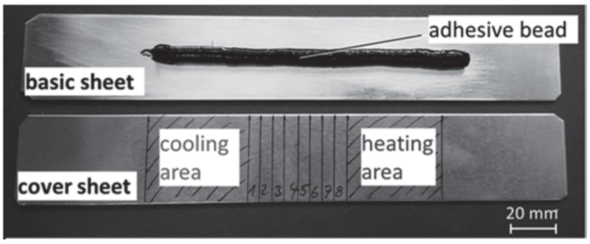

Fig. 4: *Aluminum sheet with adhesive bead (upper part) and cover sheet (lower part) before assembling the sandwich compound. On the cover sheet the areas for cooling (left side) and heating (right side) are marked. The specimen is prepared for a tool distance of 47 mm.*

Different adhesives were tested for an evaluation of their feasibility for the local curing process. The three two-component adhesives SikaFast 5215, 3M DP410 and Adchem Acralock 1015 were chosen, which offer high viscosity, high shear strength and working times between 5 and 15 minutes, according to the manufacturer's data sheets. The first two have already shown good results in earlier studies without a local heating [2]. Furthermore, the one-component adhesive Henkel Teroson 1510 was chosen. In contrast to typical one-component structural adhesives, Teroson 1510 offers a significantly faster curing mechanism and the curing reaction takes place below 100 °C [6]. In case of the two-component adhesives locally higher temperatures are used to accelerate the curing reaction. In [7] is stated that the following time temperature correlation holds: a temperature increase of about 10 K leads to bisection of working and hardening time. This effect is used to obtain a cured adhesive at the one side and a liquid adhesive at the other side of the specimen. Using the described test setup at first a constant temperature of the heating elements was adjusted. This temperature was varied between 40 °C and 70 °C. In case of the one-component adhesive Teroson 1510 the heating temperature was adjusted to 95 °C according to the manufacturer's instructions [6]. Then for each adhesive the minimal required curing time was experimentally investigated using the peel test. For each chosen temperature of the heating elements a quasi-static temperature distribution was achieved within the sandwich material. In the area of heating and cooling the temperatures of heating and cooling elements have also been reached within the adhesive layer. The area between the elements shows a linear temperature gradient. Fig. 5 depicts a time-temperature curve for the adhesive Acralock 1015 and a configuration with a heating temperature of 70 °C and a cooling temperature of 20 °C with a tool distance of 47 mm.

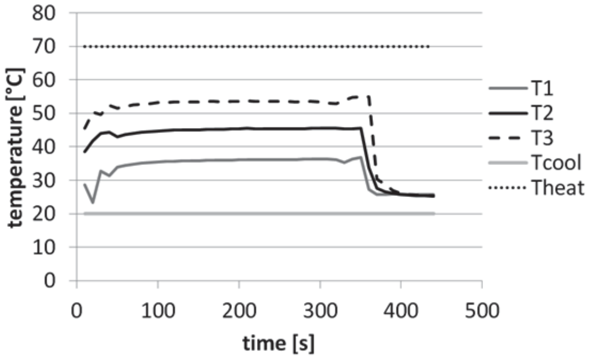

***Fig. 5:** Time-temperature curve for hardening of Acralock 1015 with a heating temperature of 70 °C and a cooling temperature of 20 °C. T1…T3 are the temperatures of the three sensors with locations: near cooling area (T1), middle (T2) and near heating area (T3). The position of the sensors is shown in Fig. 2.*

The three sensors in the adhesive layer show a fast increase of temperature at the beginning and a constant temperature until the specimen is removed. The tool temperatures stay constant. Immediately after the local heat treatment the specimen was manually proven in a peel test. The cover sheet was peeled up until an angle of 90° to the basic sheet was reached. With the peel test the minimal required curing time was experimentally investigated. It is defined as time, when the adhesive can withstand the mechanical loads of the peel test only in the zone of heating. If the curing time is longer than required, the peel test stops at an earlier stage in the graded zone. Fig. 6 shows a sandwich specimen after the peel test. Therein the 90°-bending test of the cover sheet led to a delamination up to the heating zone, which indicates that the minimal required curing time was met. This condition is characterized by a fixed connection between the two sheet metals in the heating zone in contrast to the cooling and the graded zone, where the adhesive was still in a liquid state.

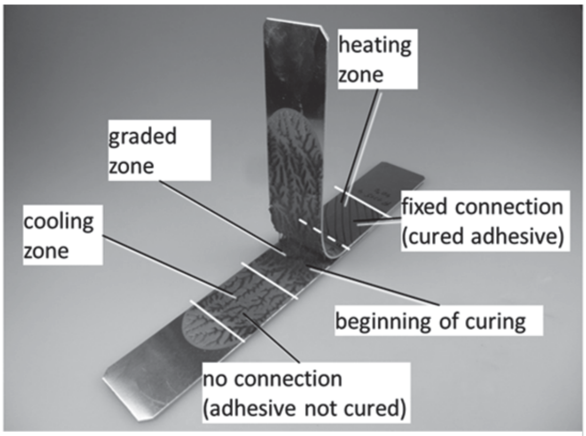

***Fig. 6:** Specimen after peel test: Temperature gradient leads to locally different curing states resulting in a characteristic peel test behavior.*

The peel test provides information about a process window for forming. When the minimal curing time is reached, a forming of the piezo-metal-compound is possible, because the specimen is fixed in the heated zone and liquid in the area, where the integrated piezomodule is located. In case of two-component adhesives additionally an upper time-limit is given by the working time. The process window for the forming operation lays between minimal required curing time and the working time. An advantage of the one-component system is, that no upper time limit exists, because the curing does not continue at room temperature. Fig. 7 shows the results for upper and lower time limits for the tested adhesives at different temperatures. Dependent on the type of adhesive and the temperature, significant differences in the process windows were found.

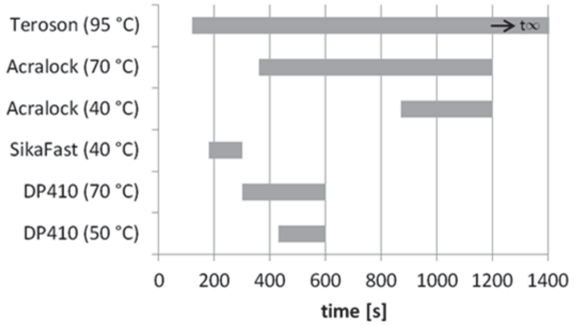

Fig. 7: *Experimentally investigated process windows for forming with locally pre-cured adhesive (fixation of outer region, liquid adhesive inside)*

In case of the SikaFast 5215 the process window for a possible forming operation lies in a range of 180 s to 300 s, when the heating temperature is 40 °C. The adhesive Acralock 1015 offers a process window from 360 s to 1200 s with a local heating temperature of 70 °C. The largest process window is given by the one-component adhesive Teroson 1510. A local heating with a temperature of 95 °C for 120 s allows a local curing in the heating zone. The sandwich can be used for forming for a longer time, because the viscous adhesive does not cure without further external heating. The peel test offers good information about the mechanical properties of the adhesive. It does not offer information on the exact degree of cure, which would allow for a better process design. Therefore different numerical models are developed and applied.

3 Modeling and numerical simulation

The experimental investigation of process windows for different time and temperature configurations is a time consuming task for all chosen adhesives and possible process parameters. With a numerical simulation of the peel test, including a simplified model for the degree of cure (DoC), process windows for time and temperature based on the curing progress of the adhesive were identified. In a previous study the curing behavior of the adhesive 3M DP410 was investigated [8]. Therein the DoC was deduced from Differential Scanning Calorimetry (DSC) dependent on time for several isothermal experiments. The present study uses an approximation of the DoC retrieved by a least-squares model-fit. To use this method in the grading simulations the prerequisite of isothermal conditions have to be fulfilled, which is nearly the case for the specimen type of the experimental section above (the temperature field varies in space but rarely in time after reaching balance conditions). With the model approach

$$q_i(t) = C_i\left[1-\exp\left(t/p_i\right)\right] \tag{1}$$

the DoC is described in a simplified way. The coefficients C_i, p_i were identified within the model-fit. A DoC value below 1.0 indicates an incomplete chemical reaction. However, for the transfer of mechanical loads also lower values for the DoC are sufficient. With the peel test experiments (parameters temperature and time) presented above a value of $q = 0.6$ was deduced and defined as threshold which indicates a sufficient stiffness amount. Fig. 8 shows the experimental results together with the fitted model for the simplified DoC for six different temperatures.

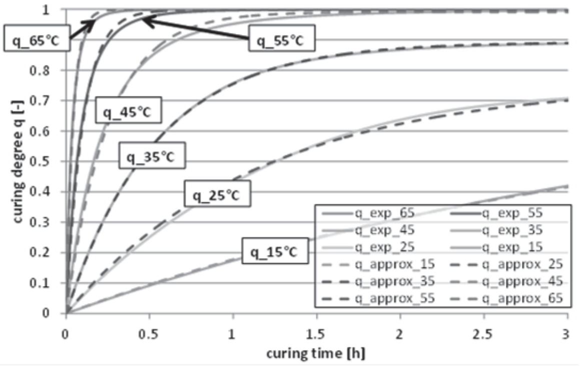

Fig. 8: *Experimentally determined degree of cure (DoC) and result of the model fit*

The fitted simplified curing model was then implemented within simulations of the graded peel specimen using the programming language APDL in ANSYS®. The half-symmetric model geometry (symmetry plane x-z) consists of thermal volume elements (SOLID70). Heat source on the left and heat sink on the right side of the peel specimen geometry are applied with constant temperature boundary conditions. The adhesive-filled gap between upper and lower sheet metal is modelled geometrically exact due to usage of solid elements (four elements along gap width of 0.5 mm, z-direction). Fig. 9 a shows the simulated time-temperature-profile for five nodal points situated at the peel-specimen center in the adhesive gap in case of a heat source temperature of 70 °C for the adhesive 3M DP 410. The resulting temperature distribution is depicted in Fig. 9 b. Within Fig. 9 c the resulting simplified DoC is depicted. With the model the change of the curing distribution is monitored. Starting at the heat source, with increasing time the zones with equal DoC values are moving towards the heat sink. Hereby, the values are rising until the simplified DoC maximum reaches the heat sink (area between source and sink completely cured).

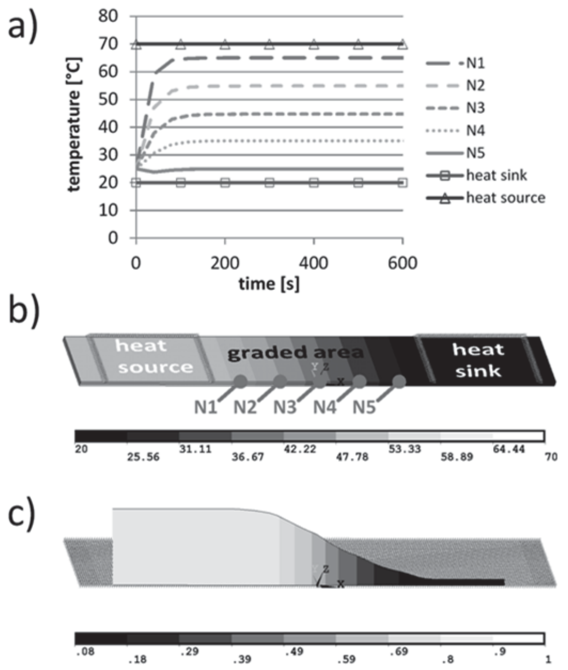

Fig. 9: *a) Simulated temperature-time-profile for five nodal points situated at the peel-specimen center in the adhesive gap (3M DP 410); b) Temperature distribution half-symmetric peel test specimen; c) Curing degree 17 min after start of curing – path plot between heat source and sink*

Within the model the distance between source and moving DoC zone is identified over the curing time. The simulations for four different heat source temperatures $T=$(40, 50, 60, 70) °C were stopped when a curing time of 1 h was reached. With regard to a later shaping process of piezo-metal-composites, higher grading times are not reasonable. Fig. 10 gives the movement of the front with DoC values of about 0.60 over the curing time.

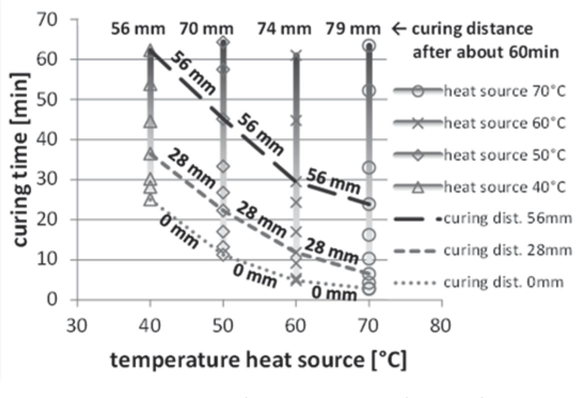

Fig. 10: *Movement of the degree of cure front with values of about 0.60. Distance measurement starts from the border between heat source and graded area.*

As a result, the graded area between cured adhesive condition (transmission of downholder pressure) and the liquid adhesive zone (enabling formability of MFC) can clearly be identified. This approach allows to set appropriate process parameters dependent on the heat source temperature and the part geometry.

Moreover, in order to obtain the ability to also simulate the processes of gelation and curing for geometries, where the exothermal reaction heat cannot be neglected, the material model from [8] was extended towards this end. From the continuum mechanical view, the 1st Law of thermodynamics (energy conservation), has to be evaluated and the thermo-mechanically coupled problem was implemented into a finite element environment (ANSYS®). Thus, the calculation of three-dimensional, inhomogeneous and transient processes becomes possible. One can denote this 1st Law of thermodynamics in terms of enthalpy and reduce it by a number of simplifications (e.g. constant pressure, no stresses, no further heat sources, nearly homogenous process within the specimen volume) which holds for the DSC experiment. Thus, the following relation between reaction enthalpy rate $\dot{h}$ and the total heat flux over the specimen's surface (term containing the integral), which equals the measured DSC signal P_{DSC} can be found:

$$m\dot{h} = -\int_A \underline{q}\cdot\underline{n}\cdot dA = P_{DSC} \qquad (2)$$

Inserting the DoC's definition from [8] (quotient of currently converted $\dot{h}(t)$ and maximum possible reaction enthalpy H_u)

$$\dot{q}(t) = \frac{\dot{h}(t)}{H_u} \qquad (3)$$

and rewriting the mass m in terms of density $\tilde{\rho}$ together with the ratio of current and reference volume (third invariant of the deformation gradient $\underline{F}$), the heat generation rate per unit volume $\ddot{q}$ required by ANSYS® is given by:

$$\ddot{q} = \tilde{\rho}\dot{q}H_u(\det\underline{\underline{F}})^{-1} \qquad (4)$$

With the help of this equation one can calculate the exothermal reaction heat out of known deformations (in terms of the deformation gradient $\underline{F}$) and the rate of the DoC $\dot{q}$ (model from [8]) for each integration point and time step. This is conducted within the USERMAT user subroutine which is used for the implementation of the material model together with the coupled field element SOLID226 (20-nodes hexaeder). After solving the mechanical part of the problem, the heat generation was obtained elementwise within the APDL-macro. After the first time step this values are used as elementwise boundary conditions to influence the heat equation and adopt the thermal problem to the exothermal reaction heat. A loop over all time steps followed to solve a first academic example with a self-accelerated reaction due to the chemical reaction heat and heat transport from the specimen's core to the surface. Fig. 11 depicts the problem sketch, FE model and solution at a representtative point in time for the inhomogeneous distribution of both temperature and DoC.

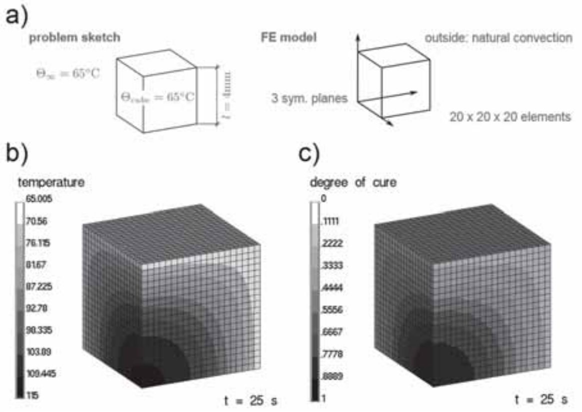

Fig. 11: *Academic example for exothermally accelerated chemical reaction due to self heating: a) problem sketch and FE model; b) temperature distribution; c) Degree of Cure (DoC)*

After an appropriate adhesive system is chosen a completely characterized model can be adopted to it, which finally allows for the simulation of the local hardening process for more complex geometries.

4 Conclusion and outlook

Experimental studies have shown that a local pre-curing of adhesive is possible using a defined temperature field. With a peel test it was proven, that different mechanical properties inside the investigated sandwich material were reached. These properties are required for the manufacturing of piezo-metal-compounds, where basic sheet and cover layer has to be fixed in the outer area whereas the adhesive surrounding the piezomodule has to be in a viscous condition at the same time. Numerical modelling of the test setup allows the investigation of the time dependent temperature field of the specimen. Additionally, a simplified model (approximation for isothermal processes) links the calculated temperature field to a degree of cure distribution within the specimen, which allows for a numerically supported identification of process windows. For more complex geometries with inhomogeneous and unneglectable transient effects, a continuum mechanical model for adhesives was extended to simulate thermo-mechanically coupled processes. Based on the numerically determined process windows, piezo-metal-compounds will be manufactured and shaped with one adhesive and a local pre-curing in future.

Acknowledgement

This research is supported by the Deutsche Forschungsgemeinschaft (DFG) in context of the Collaborative Research Centre/Transregio 39 PT-PIESA, subprojects B01 and C07.

Literature

[1] Nestler, M.; Drossel, W.-G.; Hensel, S.; Müller, R.: Fabrication method for series production of sheet metal parts with integrated piezoelectric transducers. Proc. Technol. 15 (2014), p. 494-502

[2] Nestler, M.; Hensel, S.; Drossel, W.-G.; Müller, R.: Requirements for a process chain for manufacturing of piezoceramic-aluminum sandwiches. Mater. Sci. Forum Vol. 825-826 (2015), p. 377-384

[3] Tay, T. E.; Fink, B. K.; McKnight, S. H.; Yarlagadda, S.; Gillespie, J. W.: Accelerated Curing of Adhesives in Bonded Joints by Induction Heating. J. Compos. Mater. Vol. 33, 17(1999), p. 1643-1664

[4] Carbas, R. J. C.; da Silva L. F. M.; Critchlow, G. W.: Adhesively bonded functionally graded joints by induction heating. Int. J. Adhes. Adhes. 48(2014), p. 110-118

[5] Moritzer, E.; Friedrich, N.: Laserdurchstrahlkleben von opaken Kunststoffen – schnell und zuverlässig. In: ATZ/MTZ-Fachbuch Leichtbau-Techn. im Automobilbau, Springer, Wiesbaden, D, 2014, p. 95-100

[6] Henkel: Technical Data Sheet Teroson PU 1510, 2014

[7] Weicon: Technisches Datenblatt Easy-Mix PU 240, 2015

[8] Landgraf, R.; Rudolph, M.; Scherzer, R.; Ihlemann, J.: Modelling and simulation of adhesive curing processes in bonded piezo metal composites. Computational Mechanics, 54(2), 2014, p. 547-565

Investigations on laser based joining of novel thermoplastic compatible piezoceramic modules

Stein, S.[1,3]; Roth, S.[1]; Modler, N.[2]; Gude, M.[2]; Tony Weber, T.[2]; Winkler, A.[2]

[1]Bayerisches Laserzentrum Erlangen, Konrad-Zuse-Straße 2-6, 91052 Erlangen, Germany
[2]Institute of Lightweight Engineering and Polymer Technology (ILK), Technische Universität Dresden, Holbeinstr. 3, 01307 Dresden, Germany
[3]Erlangen Graduate School in Advanced Optical Technologies (SAOT), Friedrich-Alexander-Universität Erlangen-Nürnberg, Paul-Gordan-Str. 6, 91052 Erlangen, Germany

Abstract

Active noise reduction, structural health monitoring and energy harvesting are potential applications of piezo actuators, particularly in automotive and aeronautic applications. Since piezoceramic modules are commonly produced and soldered manually, low reproducibility and high cycle times are the result. This restrictions in manufacturing prevent a widespread application of smart materials, resulting in a demand of novel manufacturing and joining methods, which can be automatable. Thus, a joining method was recently introduced, which is based on the melting of a spherical CuSn12 braze preform and is referred to as laser droplet joining (LDJ). This paper presents the manufacturing of novel thermoplastic compatible piezoceramic modules for the integration in fiber-reinforced thermoplastic composites and the utilization of LDJ for joining these modules.

1 Introduction

In the last years, composite assemblies with actuator functionalities became focus of interest for automotive and aerospace industry [1–3]. Such smart structures are defined as a system consisting of a passive structural component and additional functional elements e.g. sensors, actuators or electronic devices.

These smart structures can be manufactured by integrating e.g. piezoelectric actuators into fiber-reinforced plastic (FRP) structures, which would provide functionalities like structural health monitoring, active vibration damping or sensor applications and therefore are key to lightweight construction. The state of the art is the attachment of such actuators after the manufacturing process to the structural parts. In this context, the main restrictions are process time and costs. Furthermore, the attachment of actuators in a downstream process e.g. by gluing, results in design restrictions, preventing the placement of the actuator at the position of highest yield for the desired functionality. Hence, a direct integration of piezoelectric sensors and actuators during the manufacturing of composite structures proposes significant advances regarding the state of the art technologies. This paper focuses on the process chain from manufacturing of thermoplastic compatible piezoceramic modules (TPMs) over the electrical joining and the subsequent integration of TPMs into the composite part. For electrical contacting, a laser droplet based joining method (LDJ) is applied, which was described in [4–6]. The LDJ process is capable of joining Cu conductors with solder pads or foils with thicknesses below 20 µm without damaging foil, metallization layer or substrate, respectively. The filler material used is CuSn12 with a solidus temperature of 830 °C and a liquidus temperature of 1000 °C [7]. Thus, the braze joint can withstand the thermal processing temperatures during the integration into fiber-reinforced thermoplastic composite structures which reaching up to 380 °C.

2 TPM design, manufacturing and electrical joining

In regard to the realization of additional functionalities in fiber-reinforced thermoplastic composites, new piezoceramic module designs are required. Due to the high processing temperatures, the integration of commercial piezoelectric modules is not possible. In this context, novel thermoplastic compatible piezoceramic modules (TPMs) are developed, consisting of two thermoplastic carrier films, metalized with an electrode structure and a piezoelectric layer in between (fig. 1). Additionally, contacting interfaces are implemented into these modules to realize the electrical contact between the electrode structures and external conductor wires.

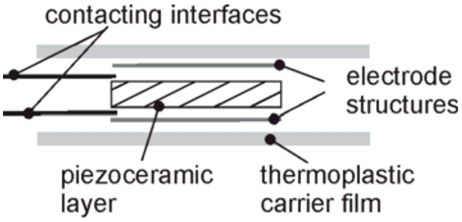

Fig. 1: *Schematic of a thermoplastic compatible piezoceramic module (TPM)*

In regard to the operation direction of the piezoceramic modules, the use of different piezoelectric layers, e. g. thin PZT wafers or piezofiber composites, is expedient. For the realization of a high volume production, an adapted manufacturing process for TPMs is developed. It bases on a roll-to-roll process (see fig. 2).

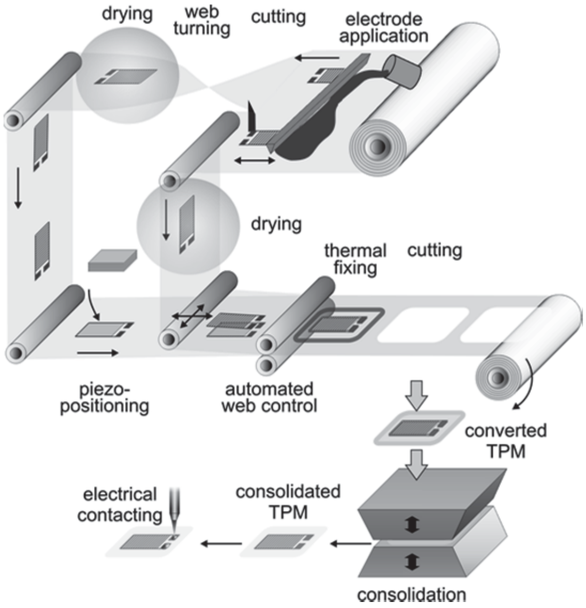

Fig. 2: *TPM manufacturing process*

Thereby, electrode structures are printed to the thermoplastic carrier film webs via screen printing in the first processing step. Afterwards the ink is dried, the webs are cut and the piezoelectric layer is inserted between the two webs. The electrode structures have to be aligned congruently to each other. This process step is monitored by an optical control system to ensure proper alignment. After the assembly of thermoplastic films and piezoelectric layer, the TPM are thermally fixed, cut and transferred into a hot press, where the consolidation of the TPM by the use of temperature and pressure takes place. The resulting modules will be subsequently electrically contacted by LDJ and polarized by applying an electric field.

Since the described TPMs are designed for material homogeneous integration into structural composite parts, a processing into PA6 composite structures would require process parameters of 250 °C to 270 °C and pressures of minimum 5 bar. The extension of the material range towards polymers with higher melting temperatures e.g. polyphenylene sulfide (PPS), requires processing temperatures of about 320 °C and even 380°C for polyetheretherketone (PEEK). Those processing parameters can't be withstood by standard Sn96.5Ag3Cu0.5 lead free solders due to the low melting temperature of 219 °C [8]. Thus, a novel joining method is necessary for the electrical contacting of TPMs. In this context, the LDJ method, which is based on the melting of spherical CuSn12 braze preforms, is applied. The joining process can be divided into four different phases. First the braze preform is inserted into the capillary where it is irradiated by a laser pulse. The laser pulse thoroughly melts the braze preform, which is subsequently ejected from the capillary via inert gas overpressure. After a flight phase, the molten droplet wets the electrode structure of the piezoceramic and the copper wire, resulting in a firm joint.

3 Experimental investigations

3.1 TPM manufacturing

In regard to the contacting area for the electrical joining, different TPM configurations were investigated. The first group of specimen is manufactured with free interfaces, since the contacting interfaces are placed outside to the thermoplastic carrier films (fig. 3 a). Furthermore, a second configuration of TPM with cutouts in the thermoplastic carrier films, directly above the embedded conducting interfaces (see fig. 3b, was manufactured. Thus, the influence of soldering positions can be investigated.

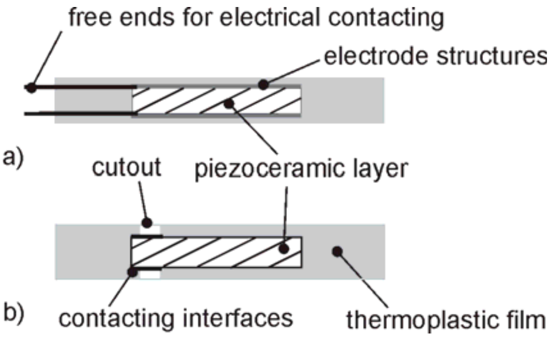

Fig. 3: *Investigated configuration of contacting areas:*
a) *TPM with free contacting interfaces,*
b) *TPM with cutout.*

The influence of the material system and interface thickness to the brazeability was investigated by using different interface materials and dimensions. Selected configurations include silver foils or copper foils. In table 1 configurations and foil thicknesses of the used contacting interface materials are listed.

***Table 1:** Specimen configurations*

Specimen nomenclature	*Interface*	*Free/ Cutout*	*Thickness [mm]*
AgF-0.035	*Silver-foil*	*Free*	*0.035*
AgF-0.015	*Silver-foil*	*Free*	*0.015*
CuF	*Copper foil*	*Free*	*0.035*
AgC-0.035	*Silver-foil*	*Cutout*	*0.035*
AgC-0.015	*Silver-foil*	*Cutout*	*0.015*
CuC	*Copper foil*	*Cutout*	*0.035*

The cutouts are machined using a punching tool with a diameter of 3 mm before assembling the TPM. During the positioning of the piezoceramic layer, the interfaces are also inserted between the thermoplastic carrier films and the ceramic layer in a single processing step. Afterwards the modules are consolidated in a laboratory press applying a temperature of 250 °C and a pressure of 5 bar for a dwell time of 10 s. Figure 4 shows exemplary module configurations and respective contacting areas.

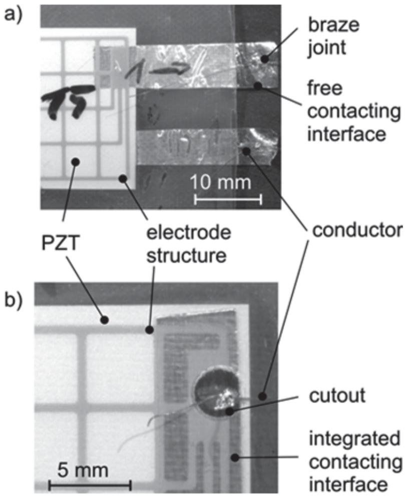

***Fig. 4:** Details of exemplary investigated TPM configurations: **a)** TPM with free contacting interfaces; **b)** TPM with cutout.*

3.2 Laser droplet joining process

For LDJ, a fiber laser with a wavelength of 1070 nm, a maximum optical output power of 200 W and a collimated beam diameter of 6.9 mm is used for melting the braze preform. It is focused by a lens of focal length $f = 50$ mm which results in a theoretical spot diameter of 10.9 µm. Nevertheless, the setup is operated with a focal offset of 11 mm in order to broaden the intensity distribution. Further, a nitrogen feed attached to a pressure regulator provides a defined nitrogen overpressure which is being monitored in situ by a pressure sensor. In order to assess the time temperature evolution during the joining process, a Type K thermocouple of NiCr/NiAl alloy was used. The sample rate was 200 Hz. The time response according to datasheet was 0.1 sec. The measured results are shown in table 2:

***Table 2:** Time dependent temperature in the liquidus region of CuSn12 braze material*

T [°C]	*t [ms]*
345.0	*0*
1097.6	*5*
1000.0	*10*
942.2	*15*
886.5	*20*
836.1	*25*
787.7	*30*

It can be assumed, that diffusion at the Ag-Cu interface will be significant if the temperatures are above the melting temperature of silver, since diffusion in liquids is magnitudes larger than in solids. Yet the time interval of significant heat at the joining interface is approximately 30 ms according to the thermocouple measurements. After cooling below 787 °C, the materials will be in solid state, so it can be assumed that diffusion will reduce significantly.

3.3 Diffusion

Diffusion is defined as mass transport by atom movement. In literature several diffusion mechanisms are known e.g. vacancy diffusion, self diffusion or interstitial diffusion. Most of the diffusion mechanisms can be characterized by the magnitude of the observed diffusion coefficient. The formula used for describing uni-dimensional concentration gradients in the scope of this paper is proposed by [9] and [10] in slightly modified form:

$$C(x,t) = C_2 + \frac{C_1 + C_2}{2}\left[1 \pm erf\left(\frac{x}{2\sqrt{D \cdot t}}\right)\right] \qquad (1)$$

Whereas C_2 is the concentration in weight percentage (wt%) of element 2, which is in the described case silver (Ag). C_1 means the concentration of copper (Cu) in percent by weight, x is the coordinate, *D* the diffusion coefficient and *t* the residence time. Using equation 1, the concentration profiles for different residence times (t_i) are calculated. Exemplary analytical results are shown in fig. 5.

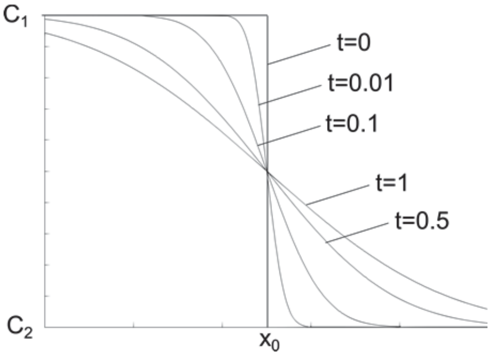

Fig. 5: *Analytical solution of the diffusion equation for different residence times.*

In order to evaluate the concentration distribution in the joining area, the element distribution has been measured using EDX analysis. Therefore, polished cross sections of joints on 15 µm and 35 µm Ag-foils have been analyzed by EDX linescans. Subsequently, the element distribution has sbeen analyzed using a sum of least squares fit, which enables a statement regarding residence time and diffusion coefficients occurring during laser droplet joining.

3.4 Performance test using digital image correlation

The manufactured TPMs were polarized by applying an electric field of 2 kV/mm during a dwell time of 5 minutes. After 24 hours the specimen were investigated in regard to the strain hysteresis by applying a sawtooth excitation signal using an input voltage of 0 V to 360 V and frequency of 0.01 Hz. Due to the changing electric field, the deformation of the TPMs piezoceramic layer can be detected by high resolution optical measuring methods. In the presented paper the measuring system ARAMIS (GOM GmbH) is used to detect the cyclic deformation of the TPMs. It is based on a contact less optical 3-D deformation measurement system. By the use of two cameras the position and deformation of characteristic patterns (facets), which means the deformation behavior of the specimen according to applied loads, can be detected. Applying this technique, the evaluation of the 2-D and 3-D deformation of the specimen can be calculated using the ARAMIS software.

4 Results and discussion

4.1 Diffusion

All joints have been generated using a laser pulse power of 145 W and a nitrogen pressure of 120 mbar against ambient pressure. For the joining experiments a capillary made of zirconia toughened aluminum oxide (ZTA) has been used. The machining head was placed 1 mm above the joining area. For the evaluation of the element distribution as preliminary consideration, argon was neglected, since it will superimpose with silver in the element spectrum due to its electron shell configuration, which will result in large errors. Furthermore, gold is not evaluated in the EDX spectra, since it has been used for sputtering to increase the conductivity and thus the resolution of the acquired data. Nevertheless, omitting gold will not lead to large errors, since gold is applied uniformly on the specimen and thus will not influence the distribution of the other elements. Argon can't be expected in significant amounts either, since the measurements are carried out in vacuum of 8.66 µPa. All elements were evaluated in a way, that the individual share of each element concentration adds up to 100 wt%. In this context, fig. 6 shows an exemplary micrograph of an investigated specimen consisting of Ag foil (15 µm) and CuSn12 braze. On each specimen five EDX line scans have been evaluated to quantify the element distribution (fig. 6).

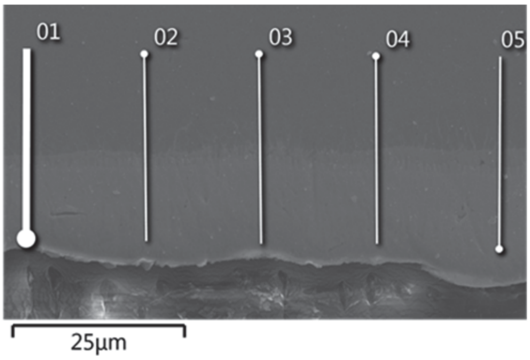

Fig. 6: *Exemplary micrograph of an investigated specimen consisting of Ag-foil (15 µm) and CuSn12 braze joint. The lines indicate, where the EDX-line-scans have been acquired.*

By fitting equation (1) to the copper concentration using the sum of least squares method it is possible to quantify values for the diffusion coefficient *D* and for the residence time *t*. Fig. 7 shows the copper distribution after LDJ for joints on a 35 µm Ag-foil (A) and on a 15 µm Ag-foil (B) and the respective fit.

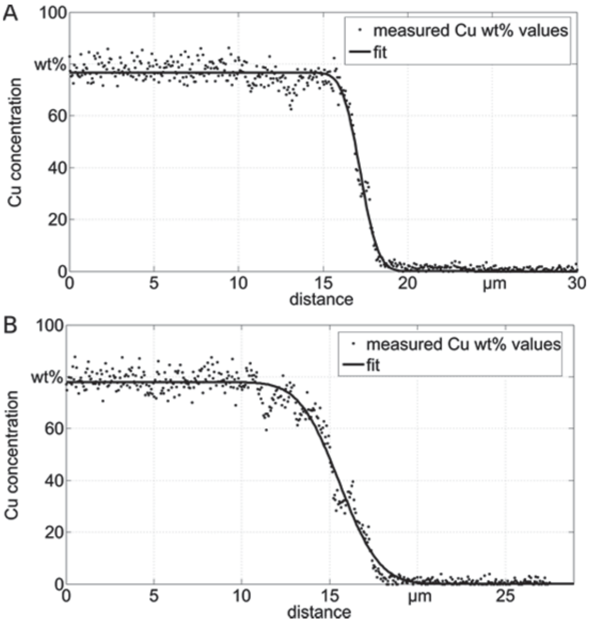

Fig. 7: Discrete measured values of Cu and the respective fit on a 35 µm foil ***(A)*** *and a 15 µm foil* ***(B).***

Since in the described case it is difficult to estimate the precise residence times, due to the delay of the used thermocouple, the product of diffusion coefficient and residence time *Dt* was evaluated. The results are shown in table 3.

Table 3: *Results of the analytical evaluation of the diffusion zone on a 15 and 35 µm Ag foil using sum of least squares fitting to determine Dt.*

	σ_{fit} ***[wt%]***	***Dt*** ***[µm²]***	c_0 ***[%]***
15 µm Ag foil			
Mean (n=5)	*3.88*	*1.51*	*77.75*
σ		*0.71*	*1.13*
35 µm Ag foil			
Mean (n=5)	*4.68*	*3.95*	*75.95*
σ		*5.26*	*1.86*

In table 3 σ_{fit} represents the standard deviation of the fit in respects to the discrete measured values. The deviation is higher for the 35 µm Ag foil. Furthermore, it can be seen that for larger thicknesses of Ag foils the product *Dt* is larger. This indicates enhanced diffusion processes when joining on thicker foils. Nevertheless also the standard deviation of *Dt* is significantly higher, thus it can be assumed that the diffusion face between CuSn13 braze and Ag is less uniform than on a 15 µm foil. The maximum concentration of copper is in both cases above 75% with low standard deviations. Taking into consideration the thermocouple measurements which indicate a time period of 30 ms in the liquidus region of the CuSn12 braze material and using this assumption as residence time *t*, the diffusion coefficient *D* can be calculated to $5.03\ 10^{-7}$ cm²/s in case of the 15 µm Ag foil, respectively $1.317 \cdot 10^{-6}$ cm²/s for the 35 µm Ag foil.

4.2 Strain analysis

By using the ARAMIS system the voltage dependent strain in x- and y-direction of TPM were analyzed. Fig. 8 shows exemplarily determined strains in x-direction of the investigated specimen. In regard to the different TPM configurations, the results of the deformation behavior differ slightly.

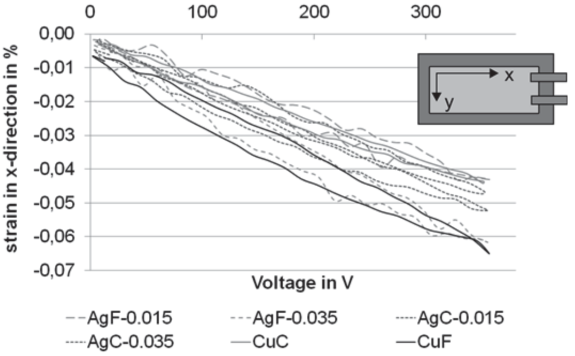

Fig. 8: *Strain hysteresis of the investigated TPM (strain in x-direction)*

The differences can be caused by deviations in the PZT material but also by the different contacting areas of the electrodes and interfaces. It is obvious that the configurations with copper foils reach relatively high strains. These foils are coated by a conductive adhesive, which enables an optimal contact between the electrode structure and the interface. The silver foils enable only a loose contact, caused by external pressure due to the embedding in the thermoplastic carrier films of the TPM. Significant differences between the configurations “free” or “cutout” are not clearly detectable.

5 Conclusions

Thermoplastic compatible piezoceramic modules are developed for the material homogeneous integration into fiber-reinforced thermoplastic composites. This paper shows the manufacturing of these novel piezoelectric transducers as well as the electrical contacting by laser droplet joining. Therefore, exemplary specimens are produced. Cross sections of the joining area have been evaluated by EDX line scans in order to enable a statement on the formation of diffusion zones. It can be stated, that for thicker Ag foils the diffusion zones are less uniform and thus foils of 15 µm thickness seem to be favorable as an interface for joining. Furthermore, cyclic tests of prototypic laser joined TPM show that there is only a marginal influence of different contacting interfaces and joining areas.

6 Acknowledgement

This research is supported by the Deutsche Forschungsgemeinschaft (DFG) in context of the Collaborative Research Centre/Transregio 39 PT-PIESA, subproject A04, A05 and B04.

Literature

[1] *Giurgiutiu, V.: Structural health monitoring with piezoelectric wafer active sensors. Amsterdam, Boston 2008.*

[2] *Preumont, A.: Vibration control of active structures an introduction. Dordrecht, Boston 2002.*

[3] *Aridogan, U.; Basdogan, I.: A review of active vibration and noise suppression of plate-like structures with piezoelectric transducers. In: Journal of Intelligent Material Systems and Structures 26 (2015) 12, S. 1455–76.*

[4] *Stein, S.; Heberle, J.; Gürtler, F. J.; Cvecek, K.; Roth, S.; Schmidt, M.: Influences of Nozzle Material on Laser Droplet Brazing Joints with Cu89Sn11 Preforms. 8th International Conference on Laser Assisted Net Shape Engineering LANE 2014. In: Physics Procedia (2014) 56, S. 709–19.*

[5] *Quentin, U.; Heberle, J.; Held, C.; Schmidt, M.: Laser Droplet Brazing for Electrical Contacting of Composite Materials with Integrated Active Elements. In: Procedia Materials Science 2 (2013), S. 181–88.*

[6] *Stein, S. Heberle, J.; Hugger, F.; Roth, S.; Schmidt, M.: Düsenbasiertes Laserstrahl-Löten mit Formteilen zur hochtemperaturfesten Kontaktierung piezokeramischer Substrate. LEF 2014. In: Laser in der Elektronikproduktion & Feinwerktechnik Tagungsband: LEF 2014 2014.*

[7] *Deutsches Kupfer-Institut Berlin, West: DKI Werkstoff-Datenblätter - CuSn12.*

[8] *Albert, F.; Pfeiffer, C.; Michael Schmidt; Manfred Geiger; Markus Flössel; Alexander Michaelis: Laser Soldering and Laser Droplet Joining for Mechanical and Electrical Contacting of LTCC/PZT Laminates. In: JLMN-Journal of Laser Micro/Nanoengineering Vol. 6, No. 1, 2011 (2011) Vol. 6 No. 1.*

[9] *Oettel, H.; Schumann, H.: Metallografie. Mit einer Einführung in die Keramografie, 15., überarb. und erw. Aufl. Weinheim, 2011.*

[10] *Sarafianos, N.: An analytical method of calculating variable diffusion coefficients. In: Journal of Materials Science 21 (1986) 7, S. 2283–88.*

Determination of the critical strain of thin Plasma CVD insulation layers using the barrel compression test

Müller, B.[1]; Jahn, S. F.[1]; Peter, S.[2]; Schubert, A.[1,3]

[1]Professorship Micromanufacturing Technology, TU Chemnitz, Germany
[2]Professorship of Technical Physics, TU Chemnitz, Germany
[3]Fraunhofer IWU, Chemnitz, Germany

Abstract

The direct integration of active piezoceramic fibers into sheet metal is a new approach for the manufacturing of smart aluminum sheets with sensing and actuating functionalities. The active piezoceramic fibers are electrically insulated with an a-SiCN:H Plasma CVD layer to prevent short-circuits with the sheet metal. Joining of the fibers and the aluminum substrate can be done with an interference- and form-fit generating forming process. To ensure the functionality of the smart sheet the insulation layer has to withstand the deformations during the joining process.

This paper presents a new method to specify the critical strain of both a-SiCN:H and diamond-like carbon (a-C:H) layers on aluminum substrates. The last one is a thin film material with a wide area of application, and it was initially tested as mechanically stiff insulator, too.

The occurrence of cracks or a delamination of the thin layers were determined in dependence of the degree of deformation of the coated substrate. Cylindrical samples were coated with a-SiCN:H or a-C:H and then compressed with a precision forming press. By measuring the geometrical dimensions of the samples after upsetting, the strain within the thin layer was calculated. Cracks and delamination were investigated by optical microscopy. Additionally, profilometric measurements were conducted to characterize the shape and surface of the substrates as well as the thickness and mechanical stresses of the deposited layers. The critical strains determined by the new method are compared with the results of a two-point bending test.

1 Introduction

Within the collaborative research center PT-PIESA the direct integration of active piezoceramic fibers into aluminum sheets is one approach for the generation of light-metal based components with integrated piezosensors [1, 2]. Therefore microcavities are structured into the surface of aluminum sheets by a micro forming process. Depending on the module variant, either the cavities or the piezoceramic fibers are electrically insulated with an a-SiCN:H coating [3]. In further process steps prefabricated batches of 10 piezoceramic fibers are placed in the cavities. With a second forming process, which generates an interference- and form-lock, the fibers are fixed in the cavities. During this process step, a punch is pressed onto the top of the webs. The webs were plastically deformed, which leads to a reduction of the web height. During the joining process the web-material flows sideways and clamps the fibers. Here the insulating coating is also involved in the forming process and has to withstand the deformation without damages to maintain its insulating function. The process is depicted in Fig. 1.

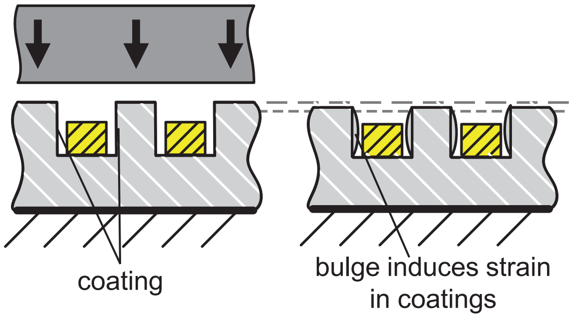

Fig. 1: *Joining by forming process, before joining (left); while joining (right)*

On the right the deformation of the web is visible. The strain that occurs during this deformation is transferred into the a-SiCN:H coating. Within this paper, cylindrical samples are coated with insulating layers and then compressed to simulate the joining by forming process.

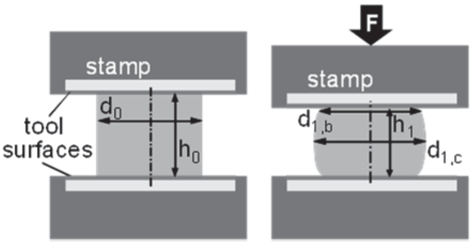

Fig. 2: *Schematic of the compression test*

The cylindrical sample, schematically shown in Fig. 2 undergoes nearly the same plastic deformation as the webs of the microstructure. By knowing the punch stroke and the geometrical parameters of the sample before and after the test, the film strains ε_h (resulting from axial compression) and ε_d (from increasing the diameter d_0 to $d_{1,c}$ at the center of the barrel) can be calculated. The precision forming press PUMA 600 kN (Hegewald&Peschke) allows it to set-up the punch stroke in steps of one micron. By varying the punch stroke, both the adhesion and the ductility of the coatings may be characterized from the detection of transverse and longitudinal cracks.

The two-point bending test originally was developed to characterize optical fibers [4] but in meantime also is used e.g. to detect crack growth in flexible thin-film technology [5]. Here the method was used to analyze crack growth in thin film on metallic substrate under pure tensile stress (see Fig. 3).

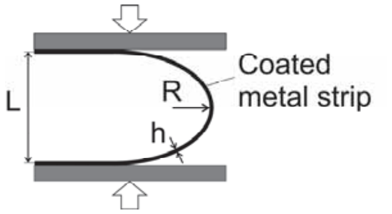

Fig. 3: *Schematic of the two-point bending test*

2 Experimental procedure

2.1 Sample preparation

Cylindrical samples were machined on a precision turning machine from a rod of EN-AW 5083 aluminum. The nominal dimensions of the samples were $d_0 = 5.0$ mm in diameter and $h_0 = 7.5$ mm in height. To ensure that the film deposition and the profilometric and microscopic measurements are carried out at the same sample orientation, a small flat was machined onto the lateral surface of the aluminum cylinders. Fig. 4 shows the dimensions and a photograph of a sample.

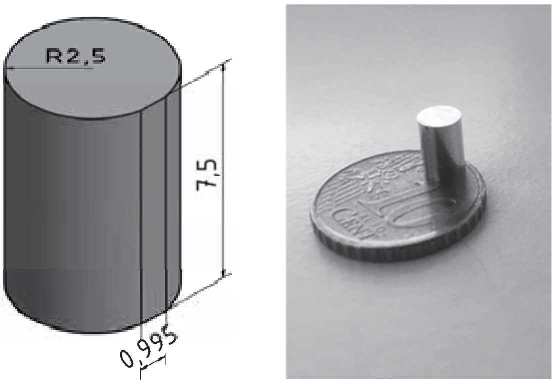

Fig. 4: *Dimensions (left) and photograph of a cylindrical aluminum sample (right)*

The lateral surface of the samples was finished using a diamond tool to reach a low roughness of Rz = 1 µm.

For the comparative two-point bending test, pieces (length 60 mm, width 13 mm) of commercial feeler gauge tape (HOREX) with thickness $h = 0.10$ mm were used as substrates.

2.2 Compression test

The barrel compression test allows it to generate at the same time compressive (ε_h) and tensile (ε_d) strains in the coating. By using a precision forming machine a very precise and reproducible shaping of the samples is possible. During the compression tests forming oil was used as lubrication. Thus, the compressed barrels showed only a very small bulge: e.g. for a sample compressed from $h_0 = 7.518$ mm to $h_1 = 7.279$ mm the bulge showed a radius of $R = 278$ mm. Hence, the calculated arc length is only 0.2 µm larger than h_1. That means, the deformed samples still are cylinders and the strains may be calculated in the following simple way.

The sum of the forming degrees φ of each direction in a coordinate system is 0. This leads to

$$\varphi_z = \varphi_x + \varphi_y \tag{1}$$

For a cylindrical sample the z-coordinate is the sample height. The forming degrees therefore can be written as

$$\varphi_z = \varphi_h = ln\frac{h_1}{h_0} \tag{2}$$

and

$$\varphi_x + \varphi_y = \varphi_d = 2 \cdot ln\frac{d_{1,c}}{d_0} \quad (3).$$

The strain from increase in circumference of the cylinder amounts

$$\varepsilon_d = \frac{d_{1,c} - d_0}{d_0} \qquad (4)$$

From (4) the center diameter after compression test can be expressed as

$$d_{1,c} = d_0 \cdot (\varepsilon_d + 1) \qquad (5)$$

By inserting equations (5), (2) and (3) into equation (1) the relation between sample height and radial strain is (6 and 7)

$$ln\frac{h_1}{h_0} = 2 \cdot ln(\varepsilon_d + 1) \qquad (6)$$

$$h_1 = \frac{h_0}{(\varepsilon_d + 1)^2} \qquad (7)$$

For the change in height Δh_{max}

$$\Delta h_{max} = h_0 - h_1 \qquad (8)$$

one finally obtains

$$\Delta h_{max} = h_0 - \frac{h_0}{(\varepsilon_d + 1)^2} \qquad (9)$$

For a given strain ε_d, Δh_{max} is the punch stroke, which has to be driven by the forming machine. Before the test series, a stiffness correction for the used tool was done. The elastic deformation of the tool and the forming press (on average 50 µm) was added to the punch stroke.

2.3 Two-point bending test

In two-point bending, the maximum tensile stress is generated at the outer side (in the coating) in the center of the sample. For pure elastic deformation of the substrate, the strain at this point may be calculated from the thickness *h* of the sample and the distance *L* of the neutral axis [4].

$$\varepsilon_{elast.} = \frac{1.2 \cdot h}{L} \qquad (10)$$

In the used experimental setup, the distance *L* is adjusted with a micrometer screw. To check the validity of equation (10) for the metallic substrates, we determined the bending radii $R_{meas.}$ as a function of *L* (utilizing digital optical microscope Keyence) and calculated the actual tensile strain based on the beam theory:

$$\varepsilon_{meas.} = \frac{h}{2 \cdot R_{meas}} \qquad (11)$$

Figure 5 shows the dependence of the minimum bending radius at center on L as well as the slope of the strains $\varepsilon_{elast.}(L)$ and $\varepsilon_{meas.}(L)$ calculated from equations (10) and (11), respectively. Due to partial plastic behavior of the metal strip, the real strain exceeds the values calculated from elastic theory (10). Therefore, $\varepsilon_{meas.}(L)$ was used to control the strain in thin films.

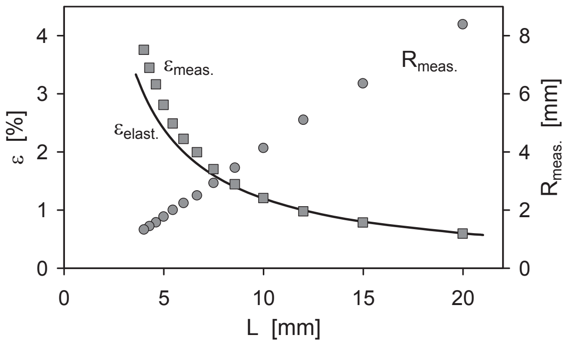

Fig. 5: *Measured bending radii and calculated from this actual strain $\varepsilon_{meas.}$ in comparison to ε_{elast} as a function of the distance of neutral axis L (cf. Fig. 3)*

2.4 Coating of the samples

The films were deposited in a Plasma CVD system MicroSys400 (Roth&Rau) utilizing a capacitively coupled 13.56 MHz RF discharge (for more details see [3]). Hydrogenated silicon carbonitride films were deposited from trimethylsilane SiH(CH3)3 (3MS) in mixtures with nitrogen, hydrogen and argon. For the a-SiCN:H deposition experiments presented, a gas mixture of 10 sccm 3MS, 100 sccm (N2 + H2) and 20 sccm Ar was used. In a test series, 2 µm thick a-SiCN:H films were deposited at a pressure of 10 Pa and the N2 and H2 flow rates were exchanged in steps. These films cover a range of compositions between a-SiC:H (nitrogen-free film) up to a nitrogen-rich a-SiCN:H.

For a C:H deposition the precursor acetylene (flow rate 160 sccm) was used and the pressure during deposition was varied between 2 Pa and 10 Pa.

All deposition experiments were performed at a RF power of 60 W and film thicknesses were controlled by adjusting the deposition time.

2.5 Characterization

For all samples the initial diameter and height were measured using a micrometer. Each sample was used for only one compression test. After the tests, the samples were cleaned in ethanol and the dimensions were measured again. Then, the samples were examined for film cracks under the optical microscope. Measurements of the bulge radii were performed using the profilometer.

3 Results and discussion

Out of the samples, which were deposited at varying the N_2 flow rate, at first three of each type were compressed without lubricant to an intended strain ε_d of both 1 % and 1.5 %. Further on, samples coated without and with maximum N_2 flow rate were compressed with lubricant in fine increments. Analyzing the sample´s surface by optical microscopy, most notable are the few but large cracks surrounding the sample in transversal direction (see Fig.6). On the other hand, the cracks proceeding parallel to the sample axis are very narrow and mainly start at the transversal cracks.

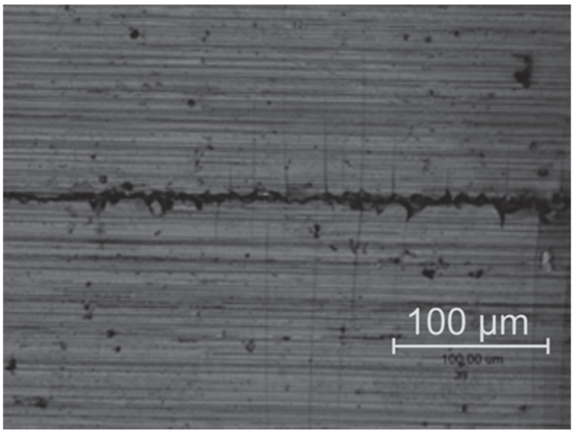

Fig. 6: *Spalling of a-SiCN:H film material along transversal cracks and fine cracks in longitudinal direction*

The adhesive failure of a-SiCN:H results from the compressive stress generated by reducing the sample height. The number of transversal cracks per mm sample height shows a better correlation to the maximum strain during compression than the remanent strain measured after the test. From Fig. 7 it is apparent, that cracks are initiated at a compressive strain of about 2 %, independent on the N_2 flow rate and hence the a-SiCN:H film composition.

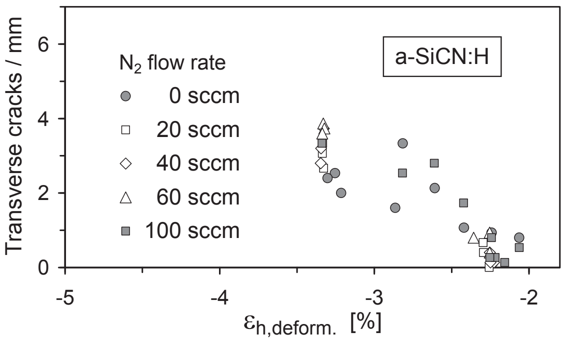

Fig. 7: *Transverse cracks per mm in a-SiCN:H films deposited at different N_2 flow rates as a function of the longitudinal strain during compression*

At the same strain value the a-C:H films start to spall along transversal cracks (see Fig. 8).

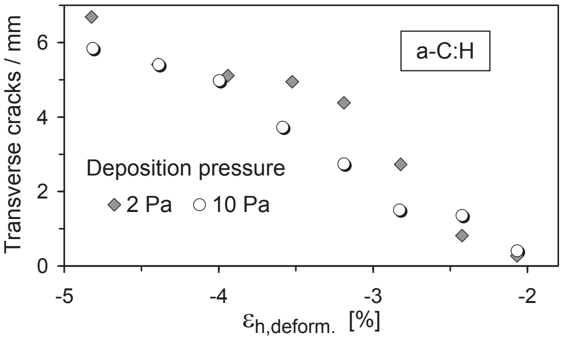

Fig. 8: *Transverse cracks per mm in a-C:H films deposited at 2 Pa and 10 Pa as a function of the longitudinal strain during compression*

Even though, the a-C:H films were analyzed to higher strain values, the graphs in Fig. 7 and Fig. 8 are similar.

The observed distribution of the crack number in dependence of the strain should not result from the precision of the compression test. The high accuracy in force and punch stroke adjustment as well as the correction for elastic deformation of the tool and the forming press are responsible for a good agreement of the intended strain values and the actual strains (see Fig. 9).

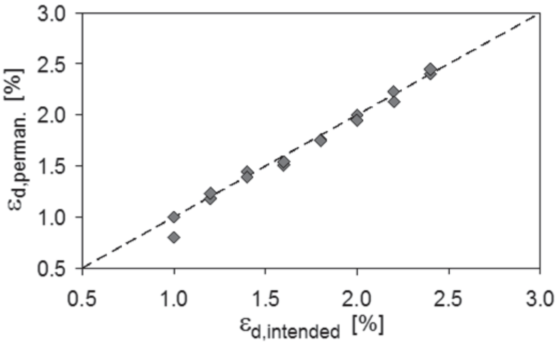

Fig. 9: *Comparison of intended and implemented values of the longitudinal strain in one test series*

Profilometric measurements were performed to identify possibly the reasons for the localized occurrence of transversal cracks. The initial surface of the aluminum cylinders is characterized by a low kinematic roughness (see Fig. 10). As you can see from Fig. 10, the surface roughness is significantly increased both after lubricated and unlubricated compression. In addition, the effect is the same for coated and uncoated aluminum cylinders. It can be assumed, that the local distribution of adhesive film failure is correlated with the position of sharp peaks built up in the surface profile, since they cause strain localization.

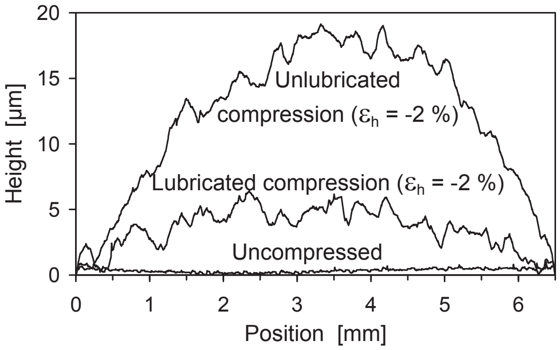

***Fig. 10:** Lateral surface profiles of samples compressed to 2 % permanent decrease in height under lubricated and unlubricated conditions in comparison to an initial cylinder surface profile*

This known surface roughening effect has a close correlation with specimen size, grain size, crystallographic texture and crystal structure and thus needs to be taken into account in micro forming system design [6].

For example, during uniaxial tensile loading of polished titanium substrates coated with diamond-like carbon it was observed [7], that the strained samples reveal a much rougher surface. It was concluded that the increased surface roughness arises from grain rotation by anisotropic plastic deformation of Ti grains upon uniaxial loading [7].

A plastic deformation induced surface roughening mechanism was also investigated for aluminum specimens with grain sizes varying from tens of microns to millimeters [8]. The experiments showed that plastic deformation roughens a free surface mainly by introducing slip bands within individual grains and relative rotation among grains. It was concluded, that the deformation induced RMS roughness is proportional to the magnitude of plastic deformation and the average grain size in the sample [8].

The fine, longitudinal cracks in Fig. 6 indicate cohesive film failure under tensile strain (increase in cylinder circumference) in the compression test. The two-point bending test generates only this mode of failure. Up to a critical strain (“ductility”) the films were crack-free. Then parallel oriented, fine cracks appear with increasing density.

It should be noted, that both types of Plasma CVD films have compressive stresses in the as-deposited state. Measurements based on the curvature of single-crystalline silicon substrates yielded very similar values of (-0.8 ± 0.1) GPa for all a-SiCN:H films and higher stress for a-C:H deposited at low pressure (deposition at 2 Pa: -2.3 GPa; deposition at 10 Pa: -1.3 GPa).

From the results in Fig. 11, the a-SiCN:H films may be strained up to about 1.3 % without cohesive failure. Again, no clear influence of the nitrogen flow rate on the mechanical strength of the films was found.

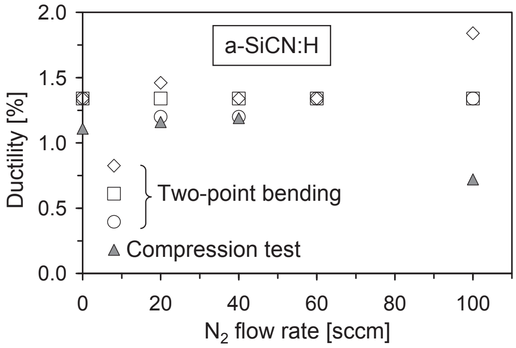

***Fig. 11:** Ductility of a-SiCN:H films as a function of N_2 flow rate measured by two-point bending (open symbols) and the cylinder compression test*

In [9] it was stated, that a-SiCN:H films show a high elongation before fracture (1% - 2%) in comparison to other insulating material. A critical failure strain of 0.7 % to 0.8 % was reported for a 0.15 µm thick a-SiN:H film deposited by Plasma CVD [4].

For the a-C:H films deposited at 2 Pa and 10 Pa, a ductility of 1.8 ± 0.1 % was measured by the two-point bending test, whereas the compression test yielded 1.4 ± 0.1 %.

In [8] uniaxial loading was used to measure the onset strain of a:CH fragmentation as function of the film thickness. These a-C:H films were also deposited from the precursor acetylene in a 13.56 MHz discharge but at a lower pressure of 1 Pa. For film thicknesses >1 µm, the onset strain of fragmentation changed only marginally. An onset strain of about 1.7 % was detected for 1 µm to 2 µm thick films [8], which is similar to the here determined results.

4 Summary

Cylindrical aluminum samples were coated with insulating a-SiCN:H and (alternatively) a-C:H layers and then compressed to simulate a joining by forming process.

The adhesive and cohesive film failures were correlated with compressive and tensile strains calculated solely from changes in sample geometry. Thus, none assumptions about material properties or laws had to be made.

It was found, that even the samples compressed without lubricant hardly deviate from a cylindrical shape. Therefore, bulging can be neglected and the strain calculation is simplified.

A high accuracy in force and punch stroke adjustment as well as the correction for elastic deformation of the tool and the forming press resulted in a good agreement of the intended strain values and the actual strains.

The dominating compressive strain, connected with the reduction of the cylinder height, causes adhesive film failure. Film rapture is promoted by plastic deformation induced surface roughening. A rough surface causes strain localization, lower forming limit, and will deteriorate also the mechanical properties of the insulating a-SiCN:H films on the aluminum webs or the piezoceramic fibers in the joining by forming process.

For comparison, the effect of tensile strain was measured by a two-point bending test, too. The measured values of the maximum tensile strain (“ductility”), up to which the films stay crack-free, match between the two methods as well as with data from literature.

The a-SiCN:H films may be strained up to about 1.3 % without cohesive failure. For the a-C:H films a ductility of 1.8 ± 0.1 % was measured by the two-point bending test, whereas the compression test yielded 1.4 ± 0.1 %.

Summarizing, the compression of coated cylinders is a useful method to simulate the mechanical effects on thin coatings during joining by forming.

Acknowledgment

This research is supported by the Deutsche Forschungsgemeinschaft (DFG) in context of the Collaborative Research Centre/Transregio 39 PT-PIESA, subproject A02 and A03.

Literature

[1] *Drossel, W.-G.; Hensel, S.; Nestler, M.; Lachmann, L.; Schubert, A.; Müller, M.; Müller, B.: Experimental and numerical study on shaping of aluminum sheets with integrated piezoceramic fibers. In: Journal of Materials Processing Technology, Volume 214, Issue 2, 2014, S. 217-228, ISSN 0924-0136*

[2] *Schubert, A.; Wittstock, V.; Jahn, S. F.; Müller, B.; Müller, M.: Joining by forming of piezoceramic macro-fiber arrays within micro-structured surfaces of aluminum sheets. In: Production Engineering - Research and Development, 2013, doi:10.1007/s11740-013-0498-7*

[3] *Peter, S.; Günther, M.; Hauschild, D.; Richter, F.: Low temperature PECVD of thin films combining mechanical stiffness, electrical insulation and homogeneity in microcavities. In: J. Appl. Phys., 2010, doi:10.1063/1.3474989*

[4] *Matthewson, M.J.; Kurkjian, C.R.; Gulati, S.T.: Strength Measurement of Optical Fibers by Bending. In: J. Amer. Ceram. Soc., 1986, doi: 10.1111/j.1151-2916.1986. tb07366.x*

[5] *Guan*, Q.; *Laven*, J.; *Bouten*, P.C.P; *de With*, G.: Subcritical crack growth in SiNx thin-film barriers studied by electro-mechanical two-point bending*, In: J. Appl. Phys.*, *2013*, *org/10.1063/1.4809542*

[6] *Fu, M.W.; Chan, W.L.: A review on the state-of-the-art microforming technologies. In: J Adv Manuf Technol, 2013, DOI 10.1007/s00170-012-4661-7*

[7] *Bernoulli, D.; Häfliger, K.; Thorwarth, K. ; Thorwarth, G.; Hauert, R.; Spolenak, R.: Cohesive and adhesive failure of hard and brittle films on ductile metallic substrates: A film thickness size effect analysis of the model system hydrogenated diamond-like carbon (a-C:H) on Ti substrates. In: Acta Materialia, 2015, doi: 10.1016/j.actamat. 2014.09.044*

[8] *Dai; Y.Z.; Chiang, F. P.: On the Mechanism of Plastic Deformation Induced Surface Roughness. In: J. Eng. Mater. Technol., 1992, doi:10.1115/1.2904196*

[9] *Gerstenberg, K.W.; Beyer, W.: Gas evolution studies for structural characterization of hexamethyldisilazane-based a-Si:C:N:H films. In: J. Appl. Phys., 1987, doi.org/ 10.1063/1.339556*

Development and characterization of piezo-active polypropylene compounds filled with PZT and CNT

Decker, R.[1]*; Heinrich, M.*[1]*; Tröltzsch, J.*[1]*; Rhein, S.*[2]*; Gebhardt, S.*[3]*; Michaelis, A.*[2,3]*; Kroll, L.*[1]

[1]*Technische Universität Chemnitz, Institute of Lightweight Structures, Department of Lightweight Structures and Polymer Technology, 09107 Chemnitz, Germany*
[2]*Technische Universität Dresden, Institute of Material Science, Chair of Inorganic Non-Metallic Materials, 01062 Dresden, Germany*
[3]*Fraunhofer Institute for Ceramic Technologies and Systems IKTS, Winterbergstraße 28, 01277 Dresden, Germany*

Abstract

Piezoactive polymer based materials enable new possibilities of functional integration in composite structures. The focus of this article is the development of a novel piezoactive material for using injection molding technology. Therefore, a thermoplastic polymer is highly filled with piezoceramic lead zirconate titanate (PZT) powder. In addition a small amount of carbon nano tubes (CNT) improves the polarization of the electromechanical PZT-compound. The objective of this work is an optimal material composition for optimized electro-mechanical properties as well as good processability in micro injection molding. Process parameters, viscosity, impedance spectrum, polarization and ferroelectric hysteresis are investigated as functions of the material composition.

1 Introduction

The development of functionalized materials in combination with integration solutions by means of polymer technologies is becoming increasingly explored. In this regard thermoplastic polymers with electrical behavior play an important role in subsequent processing such as high volume injection molding for manufacturing multifunctional lightweight structures.

Therefore, novel functionalized polymers with electro-mechanical behavior and good processability in micro injection molding for the production of semi-active and active polymer-based systems with mechatronic and electrical properties are still part of intensive investigation. Suchlike manufactured electro-mechanical systems have high potential, e.g. for using them as structural health monitoring, vibration and noise damping as well as energy harvesting in function-oriented structures [1, 2].

While piezo ceramics and polymers with intrinsic piezo effect are already state of the art, in contrast piezo ceramic composites based on a polymeric matrix system are still being investigated for a few years. In particular, thermosetting plastics, e.g. epoxy resin or polyimide filled with PZT-powder are to be applied in many fields of research activities [3, 4]. Furthermore, a representative thermoplastic system suitable for compounding with PZT-powder is for instance the polyvinylidene fluoride (PVDF) [5].

Due to the aim of a high volume content of PZT in the polymer system, that improves the electromechanical behavior, the good processability of the compound requires technologies that are limited by small series production [6]. This restriction is due to the need of exothermic reactions of thermosetting plastics or respectively of an extremely low melt flow index of the PZT-PVDF-compound.

Thus, novel piezo-electric composites based on thermoplastic polypropylene are content of the present study. Therefore, the investigation is focused on the optimized ratio between

- the polymer as matrix system, that dominates the thermoplastic processability,
- the PZT-powder with its piezo-electric properties and
- the CNT as electrically conductive filler, that increases the permittivity of the compound

to get a PZT-composite with high piezoelectric performance as well as good processability in micro injection molding.

2 Experimental

2.1 Material composition

In injection molding the steady shear viscosity at high shear rates is a crucial parameter for reliable mold filling process. For the utilization of the piezoelectric effect high amounts of PZT in the compound are necessary, thus leading to high fluidity neat polymers for the matrix system. Therefore, the initial polymer for the compound preparation was the polypropylene homopolymer Moplen HP 500V, supplied by LyondellBasell (Rotterdam, Netherlands). This high-fluidity polymer was measured with a melt flow rate (MFR) of 120 g / 10 min (ISO1133; 230 °C / 2.16 kg). It allows the production of compounds with a large amount of filler providing good processability.

The development of the piezoactive thermoplastic compound was performed in a series of experiments with various amounts of different fillers. A piezoceramic powder is used as active filler to generate the piezoelectric effect in the compound. For this purpose, the lead titanate zirconate NCE 55 (Noliac A/S, Kvistgaard, Denmark) was used. According to the supplier, this powder has a particle size between 1 µm and 3 µm and a high relative permittivity of 5,000. In order to achieve a high piezoelectric effect, a large amount of PZT is required. However, higher loadings of fillers lead to poorer processing properties due to increasing viscosity and even worse miscibility. The maximum filling level is about 80 wt% and is limited by the processability with the equipment used in the experiments. In the following analysis, PZT loadings from 50 wt% up to 80 wt% were used in order to investigate the best compromise between high piezoelectric effects and good processability.

Due to the large differences in permittivity between the polypropylene (ε_r = 2.3) and the piezoceramic powder (ε_r = 5,000), the applied electrical field is concentrated in the polymeric matrix [7]. A small amount of conductive fillers lowers the electrical resistance of the matrix material and leads to higher electrical fields in the PZT particles. This increases the dielectric displacement field in the compound, which is associated with a larger permittivity and leads to higher remnant polarization, whereby the piezoelectric effect is enhanced [4]. However, too much conductive fillers strongly reduce the electrical resistance and the electric breakdown strength of the matrix material. This leads to poor polarizability of the compound because polarization voltage must be reduced due to the lower electric breakdown strength. To investigate the optimal content of conductive fillers the PP-based masterbatch Plasticyl PP2001, with 20 wt% of multi-walled carbon nano tubes (MWCNT) supplied by Nanocyl S. A. (Sambreville, Belgium) was used. Even at low percentages these CNTs noticeably reduce the electrical resistance. The percolation threshold in PP is about 2 wt% [8]. Therefore, compounds with CNT loadings between 0 and 2 wt% were made.

2.2 Compound and sample preparation

The piezoactive compounds with different amounts of PZT and CNT were made by blending the starting materials in a HAAKE MiniLab II micro compounder (Thermo Fisher Scientific Inc., Waltham, MA USA). The melt temperature was set to 230 °C and the materials were mixed with co-rotating screws at 90 min^{-1} for 8 minutes.

To investigate the electrical properties and the electromechanical behavior of the compounds, test samples with a diameter of 28 mm and a thickness of 0.5 mm were made by using a MiniJet II micro injection molding machine (Thermo Fisher Scientific Inc.). The melt temperature was set to 230 °C and the tool temperature to 60 °C. The injection pressure was 750 bar for 3 s and the post injection pressure 400 bar for 7 s. Then, the samples were cleaned with ethanol and got an aurum electrode on each side by magnetron sputtering using an EMITECH K575XD Turbo Sputter Coater (E.M. Technologies Ltd, Ashford, UK). The chosen settings were a current of 40 mA, a sputtering time of 180 s and an argon atmosphere of 20 mbar. By using a mask this led to circular electrodes of 20 mm in diameter.

2.3 Functional characterization

The functional characterization of the polypropylene piezo ceramic carbon nano tubes (PP-PZT-CNT) compound was carried out by electromechanical impedance and ferroelectric hysteresis.

The electromechanical impedance behavior was investigated by a Hewlett Packard 4194A Impedance/Gain-Phase Analyzer (Keysight Technologies Deutschland GmbH, Böblingen, Germany).

For calculated relative permittivities a frequency of 1 kHz and a dc voltage of 1 V were set.

The ferroelectric hysteresis behavior was received with a Sawyer-Tower circuit and proprietary developed software. The influences of the electric field strength and the frequency on the hysteresis were carried out varying first between 2 kV/mm and 10 kV/mm and second from 0.5 Hz to 50 Hz.

2.4 Measurement of viscosity

The linear viscoelastic properties had been measured with a stress controlled rheometer (Haake Mars III, Thermo Fisher Scientific Inc). The parallel-plate geometry was used with a gap of 1 mm and a plate diameter of 20 mm. All tests had been carried out at 230 °C and under atmospheric air. Considering the linear region the strain amplitude for the frequency sweep was set to 0.1 for the neat polymer, whereas a lower strain amplitude of 0.0001 was set for the PZT compound.

The steady shear viscosity at higher shear rates for the PZT compounds had been obtained online in the micro compounder. It must be mentioned, that the online measured viscosity has to be considered as relatively comparative results but cannot be compared with absolute values of shear viscosity measured in plate or capillary rheometer.

3 Dielectric and piezoelectric properties

Main gain of this work is the improvement of piezoelectric properties of 0-3 compounds of PZT and polypropylene through additional admixing small amounts of MWCNT. Therewith an increase of conductivity in the matrix polymer is expected which should lead to a higher applied field at the piezoceramic powder during poling [9]. From the research of conductive polymers it is known that conductive filler can build up a network through the polymer when the volume fraction reaches the percolation threshold. As the values of electrical conductivity between CNT and polymer matrix differ strongly ($\sigma_{3,CNT}/\sigma_m = [10^{12} – 10^{20}]$) the percolation threshold should be typically somewhere between 1 wt% and 2 wt%, depending on matrix polymer and CNT used [8, 10].

This behavior could also be observed for the samples which were prepared for this report. In Fig. 1 the increasing permittivity as function of increasing CNT volume fraction is shown, whereby a significant growth of permittivity could be observed when CNT concentration exceeds 0.6 wt%. Similar results were reported by Guan et al. [9] for the system PVDF-PZT-CNT.

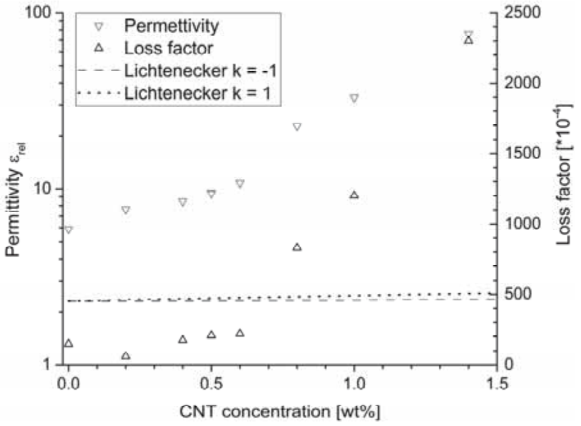

Fig. 1: *Relative permittivity ε_{rel} and loss factor tan δ of PP-PZT-CNT compounds with varying volume fraction of CNT measured at f = 1 kHz.*

The increase of permittivity seems to origin from the interaction of PZT and CNT. In Fig. 1 the theoretical increase of permittivity in the range of $0 < \omega_{CNT} < 1.4$ wt% is also displayed according to the Lichtenecker model (eq. 1) [7].

$$\varepsilon_c^k = \phi_1 \cdot \varepsilon_1^k + \phi_2 \cdot \varepsilon_2^k \qquad (1)$$

The dashed line represents the parallel and the dotted line represents the serial mixing model for the permittivity of a two phase compound. The parallel mixing model indicates the maximum achievable increase of a physical parameter in a two component compound through mixing the single phases. Conversely the serial mixing model indicates the minimal increase in permittivity. The comparison with the experimental data shows clearly that the increase in permittivity could not only result from the admixing of CNT. Thus, it seems that the CNT built up a conductive path or network between the PZT particles. However, there can be seen a relation between conductive network and thus to the percolation threshold if the dielectric losses were taken into account (Fig. 1). This means that the loss factor rises significantly after building up a conductive path by CNT through the polymer. This seems to be clear considering the Joule heating of conductive materials during cyclic operation.

As there could be reached an increase of permittivity through admixing CNT to PP-PZT compounds it should be mentioned that a clearly higher permittivity could be attained with an increase of the volume fraction of PZT. Fig. 2

displays experimental and calculated permittivity dependent on PZT concentration. Maximal and minimal possible permittivity were calculated by Lichtenecker equation (eq. 1) as well. These calculated graphs open a wide area of possible interactions of the permittivity through mixing PZT and PP which is due to the large differences in the permittivity of the single phases (ε_{NCE55} = 5,000, ε_{PP} = 2.3). The black diamonds in Fig. 2 indicate the measured sample without admixed CNT. The values range from ε_r = 3.5 to 10 for PZT concentrations between ω_{PZT} = 50 wt% and 80 wt%. Fitting the Lichtenecker equation to the experimental data induces a factor of k = -1/6. The corresponding graph is shown in Fig. 2 as well and leads to the result that higher permittivities are possible with higher PZT concentration. However, higher PZT concentrations are not possible in consideration of processability. As well, the permittivity is a parameter which can be measured easily and can give some first hints of the quality of the sample but no statements regarding the sensorial functionality could be made, which constituted the goal for this material and fabrication concept.

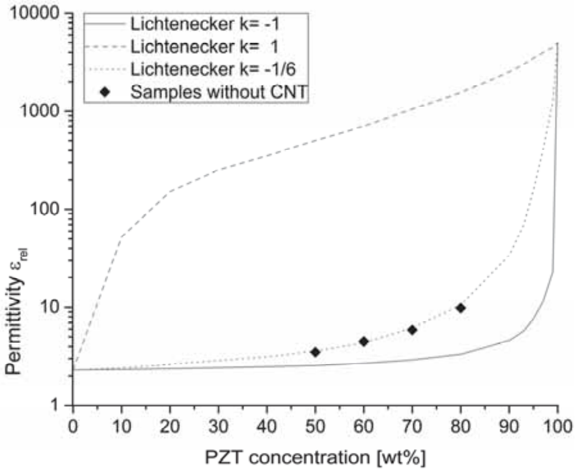

Fig. 2: *Relative permittivity ε_{rel} of polypropylene-PZT compounds with varying volume fraction of PZT measured at f = 1 kHz.*

In order to characterize the samples in terms of their application in more detail ferroelectric hysteresis were measured. For sake of clarity, no hysteresis loops are shown. Instead the results were reduced to the parameter remnant polarization P_r. The dependency of the remnant polarization regarding chemical composition, measurement frequency and electrical field strength is shown in Fig. 3. From this appears a direct proportionality to the applied electrical field and an indirect proportionality to the measurement frequency. This seems to be clear because the polarization of the originally active phase (PZT) will be better if either the applied voltage or the period of the applied field is higher. As to how far the relaxation processes of the matrix polymer influence the hysteresis behavior of the compound cannot be estimated so far.

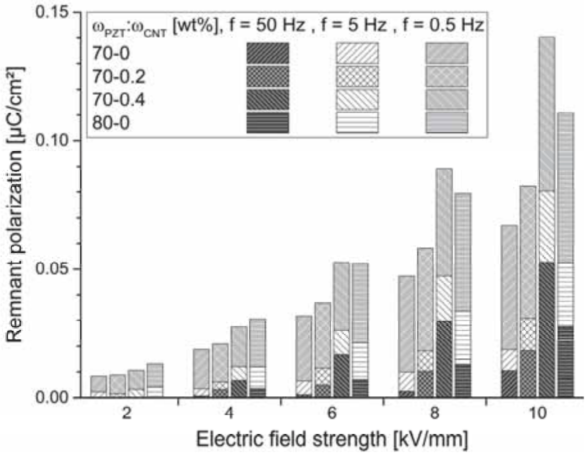

Fig. 3: *Remnant polarization P_r depending on chemical composition, applied electrical fields 2 < E < 10 kV/mm and frequencies 0.5 < f < 50 Hz.*

Referring to the influence of the chemical composition there is displayed a clear tendency to increasing polarization with CNT doped PP-PZT compounds. At an electrical field of E = 10 KV/mm there could be measured an increase in remnant polarization by a factor of 1.7 respectively 3 for the admixing of 0.2 or 0.4 wt% of CNT. Unlike the permittivities, samples with an increased concentration of PZT (ω_{PZT} = 80 wt%) could not match with the raise of P_r of CNT doped samples.

Exact data for increasing polarization values by adding CNT up to 0.6 wt% into PP-PZT70 compound are given in Tab. 1. By applying a maximum electric field of E = 5 kV/mm with a frequency of f = 5 kHz there could be reached an increase of a factor 5 by adding 0.6 wt% of CNT. The polarization voltage had to be reduced since electrical breakdown occurred at CNT concentrations of 0.6 wt% due to the higher electrical conductivity of the compound as a result of the conductive network of CNT. In this context the process related homogeneity of CNT distribution needs to be investigated in further researches.

***Tab. 1:** Maximum P_{max}, Remnant polarization P_r and coercive field E_c of PP – PZT70 – CNT compound with varying CNT concentration under an applied electric field of $E = 5$ kV/mm and a frequency of $f = 5$ Hz.*

ω_{CNT}	Maximum polarization	Remnant polarization	Coercive field E_c
wt%	10^{-2} µC/cm²	10^{-2} µC/cm²	kV/mm
0	5.24	1.13	0.77
0.2	5.88	1.48	0.84
0.4	7.21	1.58	1.05
0.5	9.40	3.37	1.80
0.6	12.61	5.91	1.96

4 Rheological properties

Due to the processability by micro compounding and micro injection molding, the characterization of the rheological properties of the PZT compound is an essential aspect. In Fig. 4 the complex viscosity |η*| as well as the storage modulus G' and the loss modulus G'' are reported for the neat polymer and with 80 wt% filled PZT compound. We note that for the unfilled polymer |η*|, G' and G'' are typical of homogeneous polymer melts. In the measured shear range the polymer behaves like a viscous fluid, G' < G'', the cross-over is expected at approx. 300 rad/s. The zero shear viscosity could be determined and was found to 100.5 Pa·s. The Cox-Merz Analogy was well verified before using additional capillary rheometer [11].

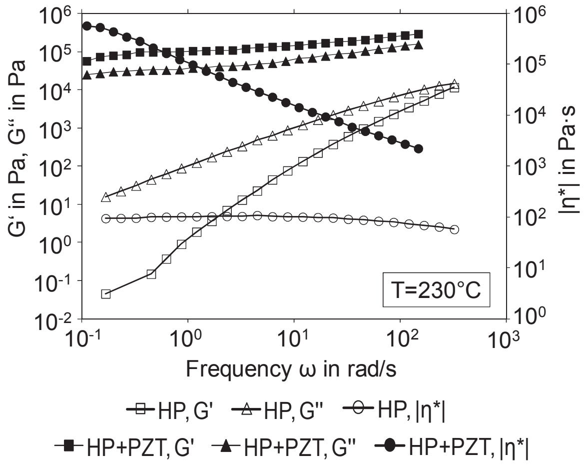

***Fig. 4:** Complex viscosity, storage and loss modulus for the neat and with 80 wt% PZT filled PP*

With incorporation of the PZT particles the fluid-like viscoelastic behavior changed to that of solid state. The storage modulus lies above the loss modulus over the whole shear range. Thus, the shown complex viscosity exhibits the behavior of an almost cross-linked rubber-like material. A zero-shear rate viscosity does not exist.

In the measured shear rate range from 200 up to 1,000 s^{-1} the typical shear thinning for thermoplastic melts can be observed for the neat PP as well as for the PZT compound (Fig. 5). The melt shows the behavior of a typical power-law-fluid. With increasing PZT content, starting from 50 wt% (HP+PZT50) up to 80 wt% (HP+PZT80), the viscosity increases significantly, however there is no uniform increase. In general an exponential increase of the viscosity can be seen, which corresponds to the narrowing of the flow passage for the polymer melt caused by the filler that is transported by the fluid and the interaction between the filler particles. In the measured shear range no convergences for high shear rates >> 1,000 s^{-1} are indicated, which normally should occur for suspensions with solid fillers. This behavior is probably caused by the geometrical shape of the particles.

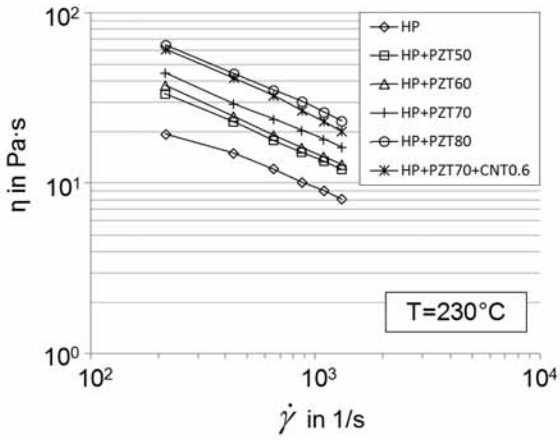

***Fig. 5:** Measured relative shear viscosity in the micro compounder for the PP with different PZT content*

It is interesting to mention, that by adding small amounts of CNT the viscosity increases rapidly. The obtained amount of 0.6 wt% CNT, which is optimal for the electrical conductivity and the remnant polarization, was added to the PP with 70 wt% PZT. The increase of the viscosity corresponds nearly to the increase when adding 10% PZT. Due to the high aspect ratio of the CNT the viscosity behavior is dominated by the amount of adding CNT in comparison to PZT. It could be speculated, that there is also some filler interaction of PZT and CNT as reported for PP compounds with CNT and Carbon Black [8], even though we do not have the same material groups.

5 Conclusion

The developed PP-PZT-CNT compound provides the ability to produce electromechanical transducer systems in large series using the micro injection molding technology. The dielectric and ferroelectric properties indicate a promising compound for procedural and structural integrated polymer based sensors. Those shown first results indicate increasing permittivity and remnant polarization by admixing CNT to the PP-PZT compound. So far best values were achieved with 0.6 wt% CNT and 70 wt% PZT. Greater levels of CNT lead to a strongly reduced electrical breakdown strength of the compound. Furthermore, higher percentages of the fillers cause a worse processability. First tests have shown that the sensorial functionality of the PP-PZT-CNT compound is given. Regarding this, there have to be done some more tests to evaluate best compositions in concerning to efficient poling, charge output under stress and homogeneity of CNT distribution in the compounds.

Acknowledgements

We gratefully acknowledge the cooperation of our project partners and the financial support of the German Research Foundation (DFG) within the Collaborative Research Center / Transregio 39 “PT-Piesa”, subprojects A01 and A06, and the Federal Cluster of excellence EXC 1075 “MERGE”.

Literature

[1] *Kräusel, V., Graf, A., Heinrich, M., Decker, R., Caspar, M., Kroll, L., Hardt, W., Göschel, A.: Development of hybrid assembled composites with sensory function. (2015) CIRP Annals - Manufacturing Technology, 64 (1), pp. 25-28*

[2] *Donoso, A.; Sigmund, O.: Optimization of piezoelectric bimorph actuators with active damping for static and dynamic loads. Z. Structural and Multidisciplinary Optimization. Bd. 38, (2009), Nr. 2, pp. 171-183*

[3] *Gómez, T. E.; Montero de Espinosa, F.; Levassort, F.; Lethiecq, M.; James, A.; Ringgård, E.; Millar, C.E.; Hawkins, P.: Ceramic powder–polymer piezocomposites for electroacoustic transduction: modeling and design. Ultrasonics, vol. 36, Issue 9, August 1998, pp. 907-923*

[4] *Ounaies, Z.; Park, C.; Harrison, J.; Lillehei, P.: Evidence of Piezoelectricity in SWNT-Polyimide and SWNT-PZT-Polyimide Composites. Journal of Thermoplastic Composite Materials, vol. 21 no. 5, September 2008, pp. 393-409*

[5] *Seol, J.-H.; Lee, J. S.; Ji, H.-N.; Ok, Y.-P.; Kong, G. P.; Kim, K.-S.; Kim, C. Y.; Tai, W.-P.: Piezoelectric and dielectric properties of (K0.44Na0.52Li0.04)(Nb0.86Ta0.10Sb0.04) O3-PVDF composites. Ceramics International, vol. 38, Supplement 1, January 2012, pp. S263-S266*

[6] *Schulze, R., Heinrich, M., Nossol, P., Forke, R., Sborikas, M., Tsapkolenko, A., Billep, D., Wegener, M., Kroll, L., Gessner, T.: Piezoelectric P(VDF-TrFE) transducers assembled with micro injection molded polymers. (2014) Sensors and Actuators, A: Physical, 208, pp. 159-165*

[7] *Goncharenko, A.V., Lozovski, V.Z., Venger, E.F.: Lichtenecker’s equation: applicability and limitations. Optics Communications 174 (2000) 1-4, S. 19-32*

[8] *Heinrich, M.; Decker, R.; Schaufuß, J.; Tröltzsch, J.; Mehner, J.; Kroll, L.: Electrical contact properties of micro-injection molded Polypropylene/CNT/CB-composites on metallic electrodes. Advanced Materials Research 1103 (2015), pp. 77-83.*

[9] *Guan, X., Y. Zhang, H. Li und J. Ou, 2013. PZT/PVDF composites doped with carbon nanotubes [online]. Sensors and Actuators A: Physical, 194, S. 228-231. ISSN 09244247. Verfügbar unter: doi:10.1016/j.sna.2013.02.005*

[10] *Deng, F., Quan-Shi, Z.: An analytical model of effective electrical conductivity of carbon nanotube composites. Applied Physics Letters 92 (2008) 071902*

[11] *Niedziela, D.; Tröltzsch, J.; Latz, A.; Kroll, L.: On the numerical simulation of injection molding processes with integrated textile fiber reinforcements. Journal of Thermoplastic Composite Materials, 26 (2013), Nr. 1, S. 74-90*

Investigations on the process chain for the integration of piezoelectric ceramics into die casted aluminum structures

Stein, S.[1,3]; Schmidt, M.[1,2,3]; Wedler, J.[4]; Körner, C.[4]; Rhein, S.[5]; Gebhardt, S.[6]; Michaelis, A.[5,6]

[1]Bayerisches Laserzentrum Erlangen, Konrad-Zuse-Straße 2-6, D-91052 Erlangen, Germany

[2]Institute of Photonic Technologies (LPT), Friedrich-Alexander-Universität Erlangen-Nürnberg, Konrad-Zuse-Str. 3-5, 91052 Erlangen, Germany

[3]Erlangen Graduate School in Advanced Optical Technologies (SAOT), Friedrich-Alexander-Universität Erlangen-Nürnberg, Paul-Gordan-Str. 6, 91052 Erlangen, Germany

[4]Friedrich-Alexander-University Erlangen-Nürnberg, Institute for Material Science, Chair of Metals Science and Technology, Martensstr. 5, D-91058 Erlangen, Germany

[5]Dresden University of Technologies, Institute of Material Science, Department of Inorganic Non-Metallic Materials, Winterbergstraße 28, D-01062 Dresden, Germany

[6]Fraunhofer Institute for Ceramic Technologies and Systems (IKTS), Winterbergstraße 28, D-01277 Dresden, Germany

Abstract

The integration of piezoelectric sensors and actuators into lightweight structural parts allows for improved functionality of these components. For integration into metal structures, aluminum die casting turned out to be suitable, since it allows to create high quality light metal goods in a high unit production [1, 2]. The paper focuses on the entire process chain for production of lightweight metal structures with sensor and actuator function starting from manufacturing of piezoceramic sensors and actuator modules over electrical and mechanical joining to the integration into aluminum matrices using die casting process.

For piezoceramic sensors and actuators so-called LTCC/PZT modules (LPM) are chosen [3]. The modules are made of low temperature cofired ceramic (LTCC) HL2000 tapes and Sonox P53 lead zirconate titanate (PZT) plates in multilayer technique. For joining outer electrodes onto the LPM a novel laser droplet based method is applied, which is based on the melting of a spherical CuSn12 braze preform. For die casting the alloy AlSi9Cu3(Fe) - 226 D is used.

1 Introduction

Almost in every branch of materials science, composite assemblies have been introduced to combine functionalities of different material classes and to improve the performance of the components.

For lightweight construction, so-called smart structures have attained much attention during the last 20 years especially for structural health monitoring (SHM), non-destructive examination (NDE) as well as noise and vibration reduction purposes. They consist of a passive structural component with applied or integrated sensors and actuators, as well as the necessary control electronics for signal processing.

One main goal and challenge in manufacturing smart structures is the integration of sensors and actuators into passive components directly during manufacturing process. The state of the art of manufacturing smart structures is attaching the actuator to the passive structure by assembling techniques like gluing or bonding in a downstream process. This causes increased process time and costs, as well as limitations in view of long time stability, positioning possibilities and environmental influences in comparison to direct integration. Consequently, direct integration of piezoelectric sensors and actuators during manufacturing of lightweight structures would be beneficial [4-6].

The approach to manufacture smart structures within this work is the integration of functional sensor/actuator modules into metal sheets using aluminum die casting. The piezoelectric modules have to withstand temperatures of T = 700 °C for short times (t = 50 ms) and mechanical pressures of around 100 MPa during the die casting process [7]. Therefore, the application of existing polymer-packaged piezoelectric modules like DuraAct™ (Invent Corp., Germany) and Macro Fiber Composites (MFC, Smart Material Corp., Germany) are limited to wall thicknesses of < 4.5 mm [8-9]. There is a pivotal demand for development of robust inorganic piezoelectric modules suitable for integration in die casted parts with greater wall thicknesses.

Piezoelectric modules consisting of stacked layers of low temperatures cofired ceramics (LTCC) and embedded piezoceramic plates offer the possibility of robust sensors and actuators suitable for integration into metallic matrices. The electrical joining of those LTCC/PZT modules (LPM) with external electrodes is challenging due to the high temperatures occurring during aluminum die casting. Thus, a joining technique called Laser Droplet Joining (LDJ) is applied and will be discussed in detail. The LDJ method is based on the melting of spherical CuSn12 braze preform via laser pulse. The aluminum die casting process excels itself due to the complexity of determining casting parameter sets, which allow the integration of LPM without damaging the ceramic matrix of the LPM. In the present paper, casting parameters will be examined and discussed regarding to their impact on the functionality of the LPM after integration.

2 Process chain and methods

2.1 Fabrication of LTCC/PZT modules

In order to achieve integrated sensor/actuator modules with frictional connection and electrical insulation to the metal matrix as well as sufficient robustness to withstand high mechanical and thermal loads during aluminum die casting, a completely inorganic LTCC/PZT module (LPM) was developed in multilayer technology. As carrier material a LTCC ceramic was chosen because of the advantages to set up 3D structures and electrical termination as well as expected good chemical adhesion to aluminum due to contained alumosilicates [10].

In order to achieve those requirements, a pre-sintered piezoelectric plate based on a PZT-PMN (CeramTec Sonox® P53) formulation was screen printed with Ag (DuPont 6160) on each side and cut to size of 26 mm x 10 mm x 0.2 mm. As carrier for mechanical stabilization, housing and electrical insulation against the metal matrix, LTCC green tape (Heraeus, HeraLock® Tape-HL2000) was chosen, due to its almost 0-shrinkage in X-Y plane. A 3-ply LTCC laminate layout which is shown as explosion image in Fig. 1 was developed and proved to be a suitable LPM design for further processing in aluminum die casting.

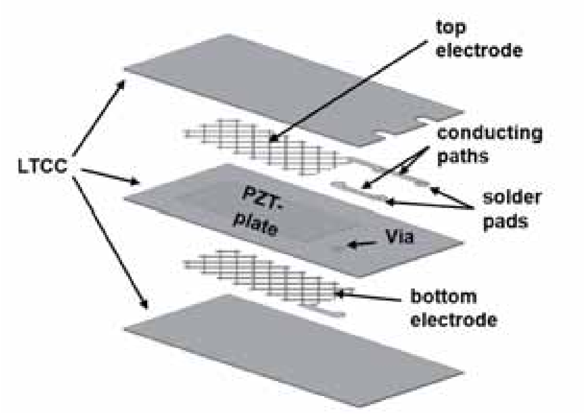

Fig. 1: Schematic layout of LTCC/PZT module (enhanced explosion image) [14].

The height of each ply was adjusted to the height of the PZT plate, resulting in a size of the LPM of 45 mm x 20 mm x 1 mm after sintering. The LTCC green tapes had to be preconditioned in a convection oven (T_{Pre} = 80 °C, t_{Pre} = 10 min) before being laminated. The top and the bottom layers got mesh-like Ag electrodes for the internal connection by screen printing. On the middle layers, vias were filled (Heraeus, TC0308) and internal wiring to the solder pads were screen printed with Ag conductor (Heraeus, TC0307). Those solder pads were screen printed in a following step using solderable Ag paste (Heraeus, TC0306). The cavities for the PZT plate in the middle layers, the cutouts for accessing the solder pads in the top layers and the separation of the LPM were done by laser trimming. After finishing the individual layers they were stacked and laminated in an isostatic lamination system (IL 4008) with p = 17 MPa at T = 75 °C for t = 10 min to assemble the LPM. The laminated LPM were sintered in a Carbolite muffle furnace RHF 15/3 as final fabrication step. A special burnout and firing profile was applied to deflagrate polymeric residues in LTCC tapes and printing pastes. Burnout was done at T_{burn} = 450 °C for t_{burn} = 2 h and firing followed at a temperature of T_{fire} = 865 °C. For the functional characterization of the LPM their dielectric (dielectric constant $\varepsilon_{33}^T/\varepsilon_0$ and dielectric loss angle tan δ) and electromechanical properties (ferroelectric hysteresis loop) were measured. The measurement was done after polarization of the samples at room temperature with an electric field of $E_{Pol} = 2$ kV/mm for $t_{Pol} = 2$ min. The dielectric properties were measured, using a Hewlett Packard 4149A Impedance Analyzer at a frequency of $f_{di} = 1$ kHz, at least one day after polarization. Ferroelectric hysteresis loops were acquired using a Sawyer-Tower circuit and proprietary developed software at electric fields of $E_{hys} = 2$ kV/mm and $f_{hys} = 50$ kHz.

2.2 Laser Droplet Joining

An essential condition for successful further processing of LPMs in the die casting process is a temperature-stable electrical connection between conductor wire and LPM. Therefore a laser based droplet joining (LDJ) method has been developed and applied to be able to achieve high thermal stability of the joining process without damaging the solder pads and electrode structure of the LPM. It is based on the melting of a defined braze volume via laser pulse. The LDJ process can be divided into four phases as shown in Fig. 2.

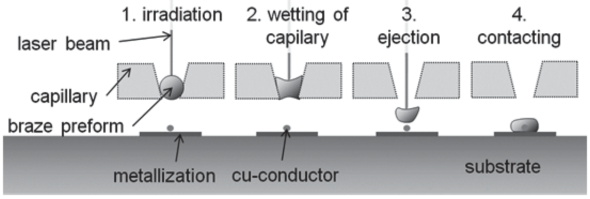

***Fig. 2:** LDJ process phases [11].*

First a spherical braze preform of CuSn12 is inserted into a capillary. Subsequently a laser pulse irradiates the braze preform and melts it throughout. After exceeding the liquidus temperature of the braze material, the braze droplet is ejected from the capillary via inert gas overpressure. After a flight phase, the molten droplet wets the solder pad of the LPM and the Cu-wire, resulting in a firm connection.

For joining, a fiber laser with a wavelength of 1070 nm is used. The maximum optical output power is 200 W. The collimated beam diameter is 6.9 mm and is being focused by a lens of 50 mm focal length which results in a theoretical spot diameter of 10.9 µm. The setup is operated at a focus offset to avoid the perforation of the braze preform by laser pulses with significant power densities.

The wire used, consisted of Cu-ETP 99.9 % with a diameter of 200 µm provided by the company Goodfellow, which was insulated with a polyimide hose. The used capillary is machined out of zirconia toughened aluminum oxide (ZTA) by means of ultra short pulse laser processing and shows superior long term performance in comparison with capillaries made from WC/Co and Graphite, which have also been investigated in [11].

Challenges arising during the joining process are mass deviations of the braze preforms, which occur due to the machining process of atomization. In order to achieve constant diameters the generated CuSn12 powder is sieved in order to select batches of preforms with relatively low diameter deviations.

The parameters for joining the LPM were kept constant. Pulse powers of 125 W and a nitrogen overpressure inside of the machining head of 110 mbar in respect to ambient pressure as well as a working distance between capillary and solder pad of 1 mm was chosen.

2.3 High pressure die casting

The contacted modules are subsequently prepared for the aluminum die casting process. First, the solder pads of the LPM were isolated by a 2K-Epoxy resin (Loctite M121HP Hysol®) as shown in Fig. 3, in order to prevent short-circuits due to aluminum melt during and after casting. To protect the braze joint of the LTCC against the influences of the die casting process (high pressure and high melt velocity) the LPM is positioned with the braze joint at the surface of the support plate. A hybrid support structure was used as insert. Detailed information about the design can be found in Körner et al. [12]. In order to ensure a planar bonding between LPM and support plate, a cut-out with a depth of 600 µm is milled into the aluminum support sheet. This cut-out allows an exact positioning of the soldered joint on top of the support plate. Screen printing technique was applied to realize a homogeneous resin thickness. Furthermore, to position the LPM on the support plate made of AlMg3, Loctite M121HP Hysol® resin is used. To avoid infiltration of melt between LPM and support plate a polyimide adhesive tape is deployed for sealing the gap. Fig. 3 exhibits an exemplary insert. A PTFE flexible hose is applied in order to protect the Cu-conductor during the casting process.

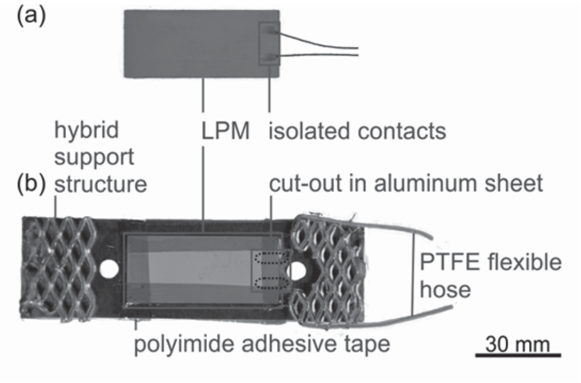

Fig. 3: Exemplary LPM after joining the wires and after the contact isolation. (b) finished insert with fixed LPM on the hybrid support.

For the fabrication of the castings a die casting unit DAK 450/54 (Oskar Frech GmbH + Co. KG, Schorndorf-Weiler) with a locking force of 458 tons is used. The castings samples have had a square base (178x178 mm²) with a variated thickness from 3 mm up to 5 mm in 0.5 mm steps. For form filling a maximum plunger speed of 2, 3, and 4 m/s was selected. The experiments are performed with the die casting alloy 226D – AlSi9Cu3(Fe) ($T_{liqidus}$ = 593 °C and $T_{solidus}$ = 521 °C [1]). The mold was tempered at 160 °C. In order to reduce gas porosity a vacuum device (Fondarex® VACUPAC – MedioP) is used, to apply a negative pressure on the mold. To show the feasibility of integrating LPMs into an Al-matrix via high pressure die casting, the samples were examined by x-ray analysis. Further, the dielectric properties after casting were investigated by an impedance analyzation.

3 Results

The selection of the substrate material for the LPM was primarily made by taking the requirements of the aluminum die casting process into consideration. In previous studies, a variety of carrier materials were tested [13]. Heraeus HeraLock®Tape-HL2000 seemed to have the best properties in terms of failure resistance during fabrication and die casting [3]. This competitive edge is mainly founded in the self-constrained behavior of the LTCC tape HL2000.

The second challenge for integrating LPMs in die casting processes is the joining process, which has to produce joining's that can withstand the occurring forces and temperatures. The laser based droplet joining approach proved to be a suitable, flux less mean for thermally stable joining's of Cu-wires on the screen printed solder pads of LPMs. As the system technology enables a pulse length control the setup is capable of counteracting deviations in braze preform volumes and thus to avoid the risk of ceramic perforations. Shear tests have been carried out before and after temperature shock tests according DIN EN 60068-2-14 (1000 cycles -40 °C /+125 °C dwell time: 10 min, transfer time: 10 s) which indicate an average shear force at failure of 22.59 ± 5.28 N (n = 10).

3.1 Radiographic inspection

Radiographic methods were applied for nondestructive characterization of the LPM after the integration of the LPM into the aluminum matrix in order to detect crack formation or processing flaws, which can occur during the casting process. The results show no influence of casting parameters regarding the formation of cracks during casting.

3.2 Functional characterization

The proper integration of the PZT plate into the LTCC carrier can be proved via functional characterization. Therefore, relative permittivity, electrical impedance spectra and ferroelectric hysteresis loops were measured of the non-embedded PZT plate, of the PZT plate in LPM, after electrical contacting by LDJ method and after integration into aluminum components by die casting. For comparison, LPMs had been poled after each process step. As figured out in prior reports [3, 14], a difference in the relative permittivity $\varepsilon_{33}^T/\varepsilon_0$ after poling between the single SP53-PZT-plate and the embedded PZT-plate in LTCC of around 300 ($\varepsilon_{33}^T/\varepsilon_{0\ (SP53\ plate)} = 2677$, $\varepsilon_{33}^T/\varepsilon_{0\ (LPM)} = 2392$; Tab. 1) can be found. This loss can be due to chemical reactions between LTCC and PZT during sintering and to mechanical clamping of the PZT plate within the LTCC matrix. Especially Pb could be detected in the initially lead free LTCC matrix structure by EDX-mapping caused by existing solid solutions in the $CaSiO_3$-$PbSiO_3$ system. These chemical reactions will alter the PZT composition and thus the material data [14]. The mechanical clamping results from deviations of the thermal expansion behavior of LTCC and PZT during cooling, after the sintering step. Therefore, mechanical stress is induced at the rim of the PZT plate and causes a decrease of permittivity [15].

Tab. 1: *Dielectric properties measured after polarization (T = RT, E = 2 kV/mm, t = 2 min) of single PZT plate, PZT plate embedded in LPM, LPM after Laser Droplet Joining and LPM integrated in aluminum.*

	$\varepsilon^T_{33}/\varepsilon_0$	*tan δ*
PZT plate SP53	*2677*	*0.0174*
PZT in LPM	*2392*	*0.0132*
LPM after LDJ	*2379*	*0.0181*
LPM in aluminum	*1922*	*0.0172*

The measurements of the electrical impedances of the initial LPM and the LDJ-contacted LPM show almost the same impedance spectra. A decrease of the permittivity was detected for LPMs, which are embedded by aluminum die casting. This might be caused by the full suppression of polarization strain. Furthermore, the embedded LPMs show a trickle of impedance amplitude at resonance. For that reason a firm bond between the LPM and aluminum matrix can be assumed.

4 Conclusion

In the scope of this paper, the feasibility of integrating LMPs in aluminum die casting processes is shown. In order to achieve this goal several challenges had to be overcome:

(1) Selection of a suitable matrix structure for embedding the piezoelectric plate, which protects those plates against damages during further processing,

(2) Development of a novel joining method, which is capable of joining the LPM with Cu conductors, without damaging the LPM and yet is able to withstand the thermal stress during die casting,

(3) Adjustment of the die casting parameters and the selection of a suitable casting alloy.

Each of the measures introduced in this paper enables a fundamental proof of feasibility to achieve the task of embedding piezoelectric sensors and actuators in aluminum die casted parts. The shear strength of the joints exceeded forces occurring during casting. Nevertheless, the forces by turbulent form filling and subsequent shrinkage of the melt are reduced by cutouts in the support structure. Also, the LDJ method proved to withstand the temperature cycles during casting while not showing influence on the functional characteristics of the LPMs. The LPM showed good performance during casting and solidification of the melt since a formation of cracks has not been observed by radiographic inspection. A variation of die casting parameters did not show an influence on the casting results Characterization of electrical data of LPM after casting process prove suitability of the set process chain to fabricate light metal structures with integrated piezoelectric sensors and actuators.

5 Acknowledgement

This research is supported by the Deutsche Forschungsgemeinschaft (DFG) in context of the Collaborative Research Centre/Transregio 39 PT-PIESA, subproject A01, A04 and B03.

6 References

[1] Brunhuber, E.: Praxis der Druckguss-fertigung. Berlin 1991.

[2] Nogowizin, B.: Theorie und Praxis des Druckgusses. Berlin 2011.

[3] Flössel M.; Michaelis A.; Gebhardt S.; Schönecker A.: Development of a novel sensor-actuator-module with ceramic multilayer technology. In: J. Ceram. Sci. Technol. Journal of Ceramic Science and Technology 1 (2010) 1, pp. 55-58.

[4] Ogando, J.: Adaptronic vibration control, Design News, 62 (2007) 9, pp. 33-37,

[5] Boller, C.: Adaptronic Systems for Aerospace Applications. In: Automatisierungstechnik 54 (2006) 6, pp. 276-83.

[6] Priya, S.; Weidenkaff, A.; An, L.; Norton, D. P.: Advances in Electronic Ceramics II. Hoboken 2009.

[7] Dargusch, M. S.; Dour, G.; Schauer, N.; Dinnis, C. M.; Savage, G.: The influence of pressure during solidification of high pressure die cast aluminium tele-communications components. In: Journal of Materials Processing Technology 180 (2006) 1-3, S. pp. 37-43.

[8] Bräutigam, V.; Körner, C.; Singer, R. F.; Kaltenbacher, M.; Meiler, M.; Lerch, R. (Hrsg.): Smart structural components by integration of sensor/actuator modules in die castings 2007.

[9] Rübner, M.; Körner, C.; Singer, R. F.: Integration of Piezoceramic Modules into Die Castings - Procedure and Functionalities. In: Advances in Science and Technology 56 (2008), pp. 170-75.

[10] Jones, W. K.; Liu, Y.; Larsen, B.; Wang, P.; Zampino, M.: Chemical, Structural and Mechanical Properties of the LTCC Tapes. In: Proceedings - SPIE the international society for optical engineering (2000) 4339, pp. 669-74.

[11] Stein, S.; Heberle, J.; Gürtler, F. J.; Cvecek, K.; Roth, S.; Schmidt, M.: Influences of Nozzle Material on Laser Droplet Brazing Joints with Cu89Sn11 Preforms. 8th International Conference on Laser Assisted Net Shape Engineering LANE 2014. In: Physics Procedia (2014) 56, pp. 709-19.

[12] Koerner, C.; Schwankl, M.; Himmler, D.: Aluminum-aluminum compound castings by electroless deposited zinc layers. In: Journal of Materials Processing Technology 214 (2014) 5, pp. 1094-101.

[13] Gebhardt, S.; Ernst, D., Bramlage, B.; Flössel, M.; Schönecker, A.: „Integrated Piezoelectrics for Smart Microsystems – a Teamwork of Substrate and Piezo“. In: Advances in Science and Technology, Switzerland: Trans Tech Publications, Vols. 77-86 (2013), pp. 1-10, doi:10.4028/www.scientific.net/AST.77.1

[14] Flössel, M.: Investigation on LTCC/PZT interface in a novel sensor-actuator-module for metal die casting. 20th IEEE International Symposium on Applications of Ferroelectrics International Symposium on Piezoresponse Force Microscopy & Nanoscale Phenomena in Polar Materials 2011.

[15] Neumeister, P.; Eßlinger, S.; Gebhardt, S.; Schönecker, A.; Flössel, M.: Effect of Mechanical Constraints in Thin Ceramic LTCC/PZT Multilayers on the Polarization Behavior of the Embedded PZT. In: International Journal of Applied Ceramic Technology 11 (2014) 3, pp. 422-30.

Experimental and numerical study on the electro-mechanical behavior of piezoceramic fibers during joining by forming

Drossel, W.-G.[1,2]; Schubert, A.[1,3]; Koriath, H.-J.[1]; Wittstock, V.[4]; Peter, S.[5]; Müller, R.[1]; Müller, M.[2]; Hensel, S.[1]; Nestler, M.[1]; Jahn, S. F.[3]; Pierer, A.[1]; Müller, B.[3]; Schmidt, M.[4]

[1]Fraunhofer Institute for Machine Tools and Forming Technology, Chemnitz, Germany
[2]Professorship for Adaptronics and Lightweight Design, TU Chemnitz, Germany
[3]Professorship Micromanufacturing Technology, TU Chemnitz, Germany
[4]Professorship Machine Tools and Forming Technology, TU Chemnitz, Germany
[5]Professorship of Technical Physics, TU Chemnitz, Germany

Abstract

A new technology enables the integration of piezoceramic fibers as functional elements into microstructured aluminum sheets by forming processes. Scope of the paper is the development of a novel method for monitoring the condition of piezoceramic fibers during the joining by forming process. For this purpose, the piezoceramic fibers are utilized as material inherent sensor during forming tests. Test samples are fabricated, electrically contacted and characterized by impedance spectroscopy. Furthermore, numerical results of the stress state and resonance characteristics of the piezoceramic/metal composites are presented. Depending on the results a novel process-control is outlined that aims on a reproducible residual preload with the surrounding metal structure without overloading the piezoceramic fibers.

1 Introduction

Structurally integrated sensors and actuators enhance lightweight composite parts with new functionalities. State of the art for application of piezoceramic patch transducers as sensor or actuators on structural components is adhesive bonding on the surface. Thus, between the component and the piezoelectric element are adhesive and other polymer layers, which lower the active power of the transducers [1].

However, new research activities enable the direct integration of lead-zirconate-titanate (PZT) fibers in the surface of metal sheets. This technology allows the integration of interconnected parallel PZT fibers into microcavities in aluminum sheets and subsequently connected in form-fit and interference-fit through joining by forming. Thereby the PZT fibers obtain a compressive preload which prevents a separation of the joining partners by tensile load on the structure. Potential areas of applications for this new technology include structural health monitoring [2] or active noise reduction [3].

In previous investigations the feasibility of the process has been demonstrated [4]. Though, the functionality of the produced prototypes was not always given. Therefore further investigations are needed to find a method for failure mode detection. By utilizing the inherent sensor function of PZT the impedance spectrum is measured during the joining operation.

A similar approach has been described in [5]. In this approach a piezoceramic ring with a diameter of 44 mm is integrated into an aluminum tube by rotary swaging. By utilizing the direct piezoelectric effect the generated charge has been detected. Based on experimental and simulated results the process design has been hedged and a non-destructive integration was ensured.

However, in this paper the electro-mechanical behavior is intensively studied to develop an in-situ monitoring method for components, which should be transferable for a high-volume production of piezoceramic/metal composites. The focus lies on a reproducible residual preload for the fibers with the surrounding metal structure but also the option of setting an application-dependent preload. Furthermore, short circuit or sensor error can be detected with this method.

2 Manufacturing of piezoceramic/metal composites

2.1 Design

Piezoceramic/metal composites consist of PZT fibers with geometrical dimensions of $12 \times 0.56 \times 0.46\ \mathrm{mm}^3$, which are placed in a 1.5 mm thick microstructured aluminum sheet. This microstructure comprises five cavities with dimension of $10 \times 0.6 \times 0.6\ \mathrm{mm}^3$. The web between two cavities is 400 µm wide. The design for integrated PZT fibers in metal sheets is illustrated with Fig. 1

The assembly gap of 20 µm results from the dimensions of the connecting parts on both sides of a fiber and the cavity walls. This gap is necessary for the assembly of the fibers and is closed by a joining by forming process. After this process step the fibers are form-fitted, interference-fitted and preloaded in the aluminum sheet as shown in Fig. 2. Hence, the PZT fibers are coupled with the metal and without any elastic interlayers.

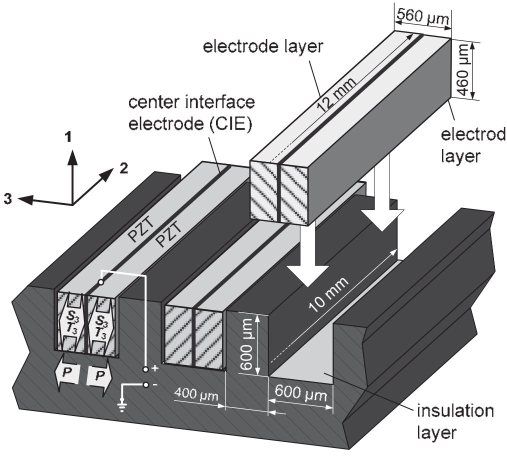

***Fig. 1:** Design of piezoceramic/metal composite*

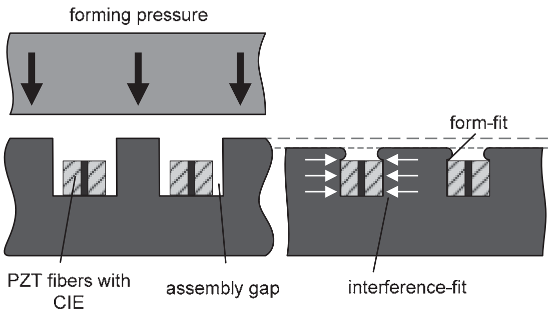

***Fig. 2:** Joining by forming process*

Fig. 1 and Fig. 2 show the structure of the fibers with a central interface electrode (CIE). This is necessary to employ the piezoelectric longitudinal (d_{33}) effect, which is used for the sensor function presented in this paper. The signal is generated between the CIE and the aluminum sheet forms as ground electrode. Magnetron sputtered electrode layers on both sides of the fibers establish the electrical connection between the fibers and the metal sheet. Furthermore, an electrical insulation is demanded between the bottom of the cavities and the CIE. A description for using this principle with piezoelectric d_{33} effect as sensor can be found in [6].

2.2 Principle of force measurement by electrical impedance spectroscopy

In the vicinity of a mechanical resonance, the electrical impedance of piezoelectric ceramics can be approximated with the simplified equivalent circuit model with lumped parameters by Van Dyke shown in Fig. 3. Thereby the capacitance C_0 represents the true electrical capacity and R_0 the true electrical contact resistance to the piezoceramic. The parallel RLC-branch embodies the mechanical impedance of the first mechanical resonance mode. In which the parameters R_2, C_2 and L_2 are equivalent to the mechanical stiffness, inertial mass and mechanical damping.

Tilmans [7] derived following proportionalities between the lumped parameters of the equivalent circuit and mechanical coupling factor α, whereas the coupling factor α indicates the effectiveness of the piezoelectric conversion between electrical energy W_{el} and mechanical energy W_{mech}:

$$C_2 \sim \alpha^2, L_2 \sim \frac{1}{\alpha^2}, R_2 \sim \frac{1}{\alpha^2}, \alpha^2 = \frac{W_{mech}}{W_{el}} \qquad (1)$$

As shown in equation (1), the electrical impedance of the piezoelectric ceramic can be changed by a variation of the coupling factor α. Based on this dependency, Lesieutre and Davis [8] proposed a method to affect the coupling factor by axial loads which cause destabilization or stiffening of a piezo patch.

In a simulative study, the coupling factor α is normalized to the preload and stepwise varied between 0.1 % and 100 %. The lumped parameters of the simulated equivalent circuit where estimated at a compressive preload of 10 N in d_{33}-direction of a single fiber from characteristic points of the impedance spectrum based on the experimental method of DeAngelis and Schulze [9].

The simulation yields an increase of the electrical impedance by decrease of the electrical coupling factor as depicted in Fig. 4 and demonstrates the feasibility of force measurement by impedance spectroscopy.

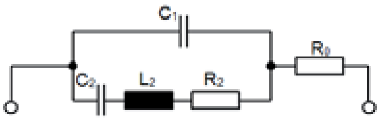

Fig. 3: *Equivalent electrical circuit of a piezoceramic in vicinity of the first resonance mode as schematic*

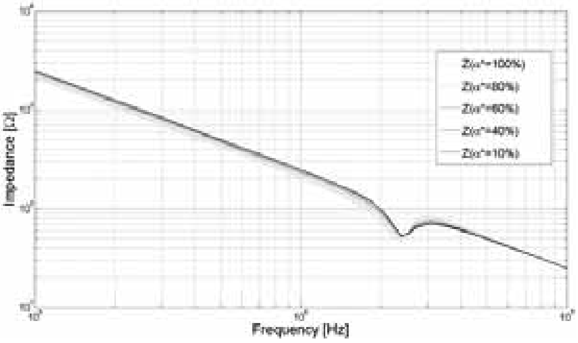

Fig. 4: *Simulated shift of impedance spectrum in dependency of mechanic coupling where α^* is the normalized coupling factor*

3 Experimental

3.1 Specimens

All experimental investigations were conducted on piezoceramic fibers with CIE. The active material is a PZT-ceramic type M1100 from Johnson Matthey. The manufacturing of the fibers was accomplished by soldering two PZT Plates of 250 µm thickness each and with a S-Pb60Sn40 solder. The CIE has a thickness of 60 µm. Afterwards the double plates are divided by a cutting process in fibers with a height of 460 µm. The microstructure of the aluminum sheet with five cavities was produced by micro-milling. Wires were attached to each CIE and the metal sheet. For insulating the CIE against the sheet metal two approaches were investigated. In the first approach the bottom section of the cavities was insulated. In the second approach the sheet metal was not insulated. Instead the fibers were coated with an insulation layer. The insulation layer was deposited in a Plasma-CVD system MicroSys400 (Roth&Rau) from a mixture of 10 sccm trimethylsilane (3MS) with 100 sccm nitrogen and 20 sccm argon. The capacitively coupled 13.56 MHz discharge was operated at a RF power of 60 W and a chamber pressure of 10 Pa. Before deposition of the hydrogenated silicon carbonitride film (SiCN:H) the samples were in-situ cleaned in an Ar-H2-plasma.

3.2 Force calibration

In order to enable the piezoceramic joining partner as material inherent sensor during the forming process, a correlation between acting force and electrical impedance is needed. Therefore compression tests of single fibers were conducted. During the compression tests a network analyzer, based on the gain and phase detector AD8302 from Analog Device, recorded the impedance spectrum at different force levels. Fig. 5 exemplarily demonstrates a sequence of impedance spectra at different compression forces. At a frequency of 2 MHz the impedance shows a good sensitivity and monotone characteristic to the applied force. Force values were recorded up to 1.7 kN until the fibers broke. This is equivalent to a compressive stress of 304 MPa. The experimental results lead to the calibration curve depicted in Fig. 6. A regression analysis yields the following calibration formula, where F_{33} is the applied force in d_{33} direction and Z_{2MHz} the magnitude of electrical impedance at 2 MHz:

$$F_{33} = 4 \cdot 10^{-37} N \cdot \left(\frac{Z_{2MHz}}{1\Omega} \right)^{12.946} \tag{2}$$

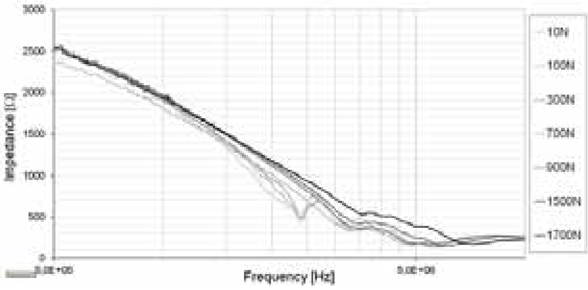

Fig. 5: *Measured impedance spectra of a single piezoceramic fiber with CIE at different compressive forces in d_{33}-direction*

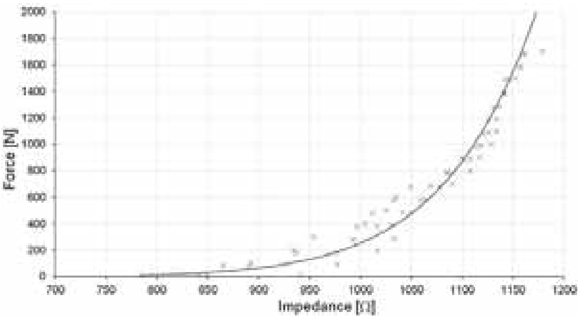

Fig. 6: *Calibration curve of compressive force F_{33} at fiber over electrical impedance at 2 MHz*

3.3 Joining by forming tests

For the joining tests, the fibers were assembled in the microstructure and electrically connected to the network analyzer as presented in Fig. 7(a). The flat upper joining tool was insulated with polyimide tape (Kapton KL-KAPT) to prevent short-circuiting of the CIE against aluminum sheet. Experiments were performed on a material testing machine. During the joining operation the upper tool moved downwards and applied stepwise a rising force up to 20 kN to the webs of the microstructure. Hence the fibers were continuously clamped through narrowing of the cavities. At every load step the movement of the upper tool stopped and the impedance of the fibers were recorded and converted into a compressive force F_{33} and stress T_{33} according to the found calibration formula eq. (2). After joining, microscopic inspection showed no visible cracks for plenty fibers in the range of the cavities as depicted in Fig. 7(b). Incipient cracks are detected merely on individual fibers. Nevertheless, they are fully functional, because the CIE is completely remained intact.

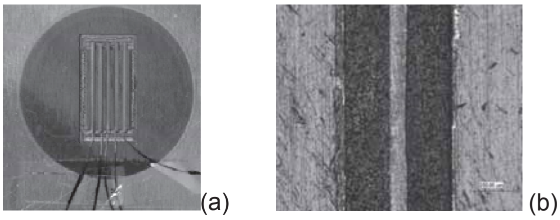
(a) (b)

Fig. 7: *Wired fibers assembled into cavities before joining (a), microscopic image fiber and microstructure after joining operation (b)*

For the aluminum sheets with insulated cavities good joining results were achieved. As exemplarily shown in Fig. 8, the compressive stress of fiber steadily rose after the beginning of the web's plastic deformation at 8 kN, which corresponds to a compressive stress of 130 MPa. The stress moved up to a first plateau of 475 MPa at 11 kN joining force which corresponds with the later presented simulative results. The subsequent rise from 475 MPa up to 765 MPa at 20 kN does not fit with the simulative results.

The second approach with uninsulated aluminum sheet was not successful. During the forming a short-circuiting of the CIE against the sheet metal occurred. This indicates a damaging of the insulation film of the CIE. Nevertheless, the proposed impedance analysis proved its feasibility for failure mode detection during the joining process in this case.

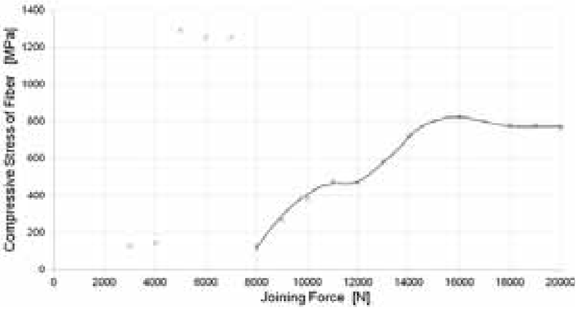

Fig. 8: *Calculated compressive stress T_{33} of a single fiber in metal structure over joining force applied by material testing machine*

4 Simulation

Within a numerical study the joining process of piezoceramic/metal composites was investigated. The geometry model is based on a 2-dimensional cut through the micromilled aluminum sheet, tools and fibers, but excludes the outer sheet metal regions for reasons of computation efficiency (Fig. 9). The section model consists of 2-dimensional plane strain elements in LS-Dyna (Release 7.1.1 Winx64, SMP, double precision, implicit solver).

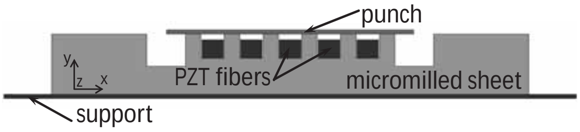

Fig. 9: *Geometry model for the joining simulation*

The punch moves force-controlled against the aluminum structure located on a fixed support. The nodes on the left and right boundaries of the sheet metal are constrained to account for the 3-dimensional nature of the problem (micro-structured cavities have a limited extent while the pure plane strain state would model cavities of infinity length). Tab. 1 summarizes the elastic mechanical properties of the PZT fiber material and aluminum. The polarization direction of the piezoceramic material equals the *x*-direction pictured with the coordinate system of Fig. 9. The plastic hardening behavior of the aluminum material was derived from pressure tests and approximated with eq. 3 (yield stress σ , true plastic strain φ). The materials of punch and support are assumed to be rigid.

Table 1: *Elastic material properties*

material	***property***	***value***
piezo fiber [10]	*Young's moduli [GPa]*	*E_x=52.6,* *E_y=E_z=59.4*
	Shear moduli [GPa]	*E_{xy}=E_{zx}=19.6,* *E_{yz}=22.5*
	Poisson ratios [-]	*v_{yx}=v_{zx}=0.422,* *v_{zy}=0.335*
aluminum	*Young's modulus [GPa]*	*E_x=70.0*
	Poisson ratio [-]	*v_{xy}=0.31*

$$\sigma = 429\varphi^{0.261}\,\text{MPa} \tag{3}$$

Fig. 10 and Fig. 11 show the equivalent v. Mises stress of the aluminum material and the stress in polarization direction (*x*-direction in Fig. 9) of the PZT fibers after joining. The latter mirrors the clamping force situation of the PZT fibers. The clamping forces decrease from the maximum of the center fiber to the minimum of the outer aligned PZT fibers.

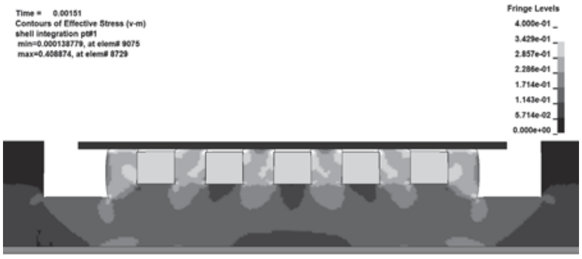

Fig. 10: *V. Mises plastic equivalent stress in GPa of the aluminum sheet metal after joining*

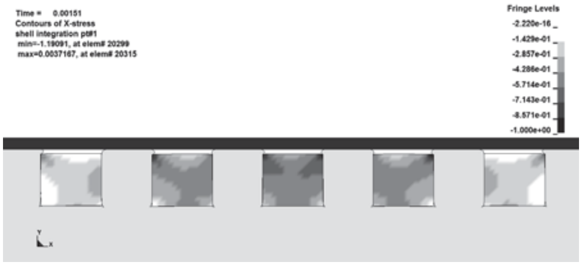

Fig. 11: *PZT fiber stress in polarization direction (horizontal dir.) in GPa of the fibers after joining*

Fig. 12 correlates the joining punch forces for rising punch positions with the associated averaged piezo fiber strains of the center fiber in polarization direction (clamping stress).

The maximum joining force of 20 kN causes a center fiber clamping stress of -550 MPa. The simulated maximum amounts only 69 % of the experimentally determined maximum of -800 MPa. Further deviations exist between the principal curve slopes of experiment and simulation. Possible reasons are the unknown exact friction conditions between sheet metal and tool surfaces, uncertainties caused by milling of the aluminum sheet and dicing of the piezoceramic fibers as well as a possible change of the electromechanical coupling during the forming. A detailed study is planned within future research to examine the reasons.

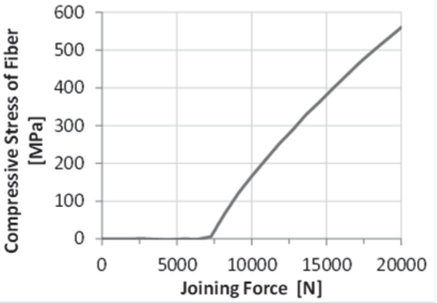

Fig. 12: *PZT fiber compressive stresses in polarization direction vs. joining process punch forces*

Finally the dynamic behavior of the model was investigated. Three joining simulations with the different final punch displacements *s*=(0.06, 0.09, 0.12) mm were carried out with the implicit solver LS-Dyna. Each of them was followed by a fully transient explicit simulation stage, in which the PZT fiber actuation was modelled according to the experiments (punch position fixed but punch force-loaded). The actuation was simulated with thermal analogy (piezoelectric strains are numerically induced by a temperature equivalent via thermal expansion [11]). A stepped actuation frequency profile (constant for a given time period) was used within the vibration stage. With an algorithm the answer frequencies of the structure and the phase shift angle, as comparison between input (piezoelectric fiber strain) and output (mechanical aluminum answer) signals, was determined for one aluminum-sheet element. Fig. 13 shows the mechanical strain answer of the aluminum element over frequencies of the frequency sweep. The change of the resonance frequencies can be clearly identified. Hence, the model can be used to evaluate the influence of geometric tolerances on the inherent sensor ability in future research.

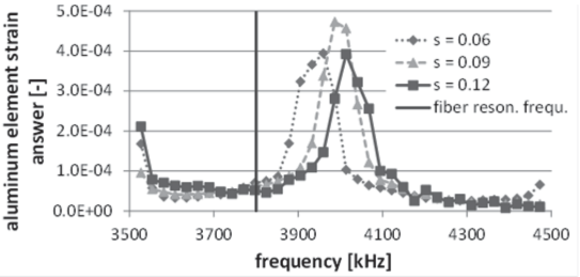

Fig. 13: *Frequency shift of the structure answer for several punch displacements s*

5 Conclusion

In this paper, the new approach with directly integrated PZT fibers in metal sheets has been investigated with respect to the electromechanical behavior. The scope of the study was to develop a method for monitoring the components during the joining by forming process to achieve a reproducible residual preload and detection of sensor errors. For this purpose, single PZT fibers with a CIE were prepared and inserted into microstructured aluminum sheets. During the subsequent forming operation the components were electrically connected to a network analyzer for recording the impedance spectrum. The impedance analysis demonstrated its applicability as in-situ method for monitoring preload and failure mode detection during joining by forming operations of piezoceramics. Within a numerical study the PZT fiber stresses were evaluated dependent on the joining load level. Deviations exist between experiment and simulation. Moreover, the model was tested regarding the dynamic behavior. Further work deal with the study of the electromechanical behavior of direct integration of interconnected parallel PZT fibers.

Acknowledgement

This research is supported by the Deutsche Forschungsgemeinschaft (DFG) in context of the Collaborative Research Centre/Transregio 39 PT-PIESA, subprojects A02, A03 and B01.

References

[1] Sumedha, M.; Bhalla, S.: Influence of adhesive bond layer on power and energy transduction efficiency of piezo-impedance transducer. In: Journal of Intelligent Material Systems and Structures 2015, Vol. 26, p. 247-259

[2] Duan, WH, Wang Q, Quek ST. Applications of Piezoelectric Materials in Structural Health Monitoring and Repair: Selected Research Examples. In: Materials 2010, 3, p. 5169-94.

[3] Aridogan, A.; Basdogan I.: A review of active vibration and noise suppression of plate-like structures with piezoelectric transducers. In: Journal of Intelligent Material Systems and Structures, Vol. 26, 2015, p. 1455-1476

[4] Drossel, W.-G.; Hensel, S.; Nestler, M.; Lachmann, L.; Schubert, A.; Müller, M.; Müller, B.: Experimental and numerical study on shaping of aluminum sheets with integrated piezoceramic fibers. In: Journal of Materials Processing Technology 214, p. 217-228

[5] Brenneis, B.; Groche, P.: Integration of Piezoceramic Tube under Prestress into a Load Carrying Structure. In: Advanced Materials Research Vols. 966-967, 2014, p. 651-658

[6] Schubert, A.; Wittstock, V.; Koriath, H.-J.; Jahn, S. F.; Peter, S.; Müller, B.; Müller, M.: Smart metal sheets by direct functional integration of piezoceramic fibers in microformed structures. In: Microsystem Technologies Vol. 20, 2014, p. 1131-1140

[7] Tilmans, H.A.C.: Equivalent circuit representation of electromechanical transducers: II. Distributed parameter systems. In: Journal of Micromechanics and Microengineering. 7, 1998, p. 285-309

[8] Lesieutre, G., Davis, C.: Can a coupling coefficient of a piezoelectric device be higher than those of its active material?. In: Journal of Intelligent Material Systems and Structures 8, 1997, p. 859-867

[9] DeAngelis D. A., Schulze, G. W.: Optimizing piezoelectric crystal preload in ultrasonic transducers. In: 38th Ann. Symp. of the Ultrasonic Industry Assoc. (UIA), Canada, 2009

[10] Hosseini-Hashemi, S.; Es'haghi, M., Taher, H. R. D.: An exact analytical solution for freely vibrating piezoelectric coupled circular/annular thick plates using Reddy plate theory. In: Composite Struct., 92(6), 2010, p. 1333-1351

[11] Dong, X.-J.; Meng, G.: Dynamic analysis of structures with piezoelectric actuators based on thermal analogy method, J. of Adv. Manufacturing Technol., 27, 2006, p. 841-844

Inverse Method for determining piezoelectric material parameters of piezoceramic fiber composites

Weiß, M.[1]; Ilg, J.[1]; Hohlfeld, K.[2]; Gebhardt, S.[3]; Rupitsch, S.[1]; Lerch, R.[1]; Michaelis, A.[2,3]

[1] *Chair of Sensor Technology, Friedrich-Alexander University of Erlangen-Nürnberg, Germany*
[2] *Chair of Inorganic Non-Metallic Materials, Institute of Materials Science/TU Dresden, Germany*
[3] *Fraunhofer Institute for Ceramic Technologies and Systems IKTS, Dresden, Germany*

Abstract

We present an Inverse Method for determining decisive material parameters of piezoceramic fiber composites. Due to their complex structure and manufacturing process, the characterization of such fiber composites through standard methods is not feasible in a satisfying way. The Inverse Method is based on the minimization of deviations between measurements and simulation results. The effective material parameters (i.e., tensor of elasticity, permittivity and piezoelectric coupling) are determined by means of an optimization algorithm.

To estimate the adhesive's influence on the composite behavior (e.g., frequency resolved electrical impedance, mechanical displacement), we compare simulation results based on detailed and simplified finite element models of the specimens. Thereby, material parameters of the used SONOX® P505 and Araldite® 2020 are determined separately. In addition, the surface displacements, which were simulated numerically and measured by a laser scanning vibrometer, are compared.

1 Introduction

Precise material parameters are required to predict the suitability of piezoceramic materials for specific applications. The characterization of inhomogeneous materials, such as piezoceramic fiber composites, has special demands. In this contribution, an approach based on simulations and measurements - the Inverse Method - is exploited to identify the aimed material parameters.

Section 2 deals with manufacturing and properties of piezoceramic fiber composites. Section 3 addresses the characterization of composites by means of the Inverse Method. In addition, effective material parameters of the composite are given. Sections 4 and 5 contain the validation of determined material parameters through laser scanning vibrometer measurements and macro model simulations. Finally, Sec. 6 discusses achieved outcomes and capabilities.

2 Piezoceramic fiber composites

The piezoceramic fiber composites are built up from lead zirconate titanate (PZT) fibers with 290 µm diameter. The piezoceramic fibers are manufactured by means of a quasi-continuous fiber spinning facility based on a phase inversion process. PZT powder (SONOX® P505, CeramTec GmbH, Germany) is mixed with a binder solution and additives to form a homogeneous slurry. The slurry contains 87.0 wt.-% PZT powder, 10.6 wt.-% N-Methylpyrrolidone as solvent, 2.0 wt.-% polysulfone binder and 0.4 wt.-% additives. It is extruded through a nozzle into an aqueous precipitation bath. Therein the binder coagulates, by which rigid green fibers are formed. The green fibers are dried for four hours at 80°C and sintered subsequently in a lead oxide-enriched atmosphere for two hours at 1060°C. The fabrication process of piezoceramic fibers, especially the adjustment of fiber diameter, is described in detail in [1].

The fibers are aligned in a mold and infiltrated with epoxy (Araldite® 2020, Huntsmen Advanced Materials GmbH, Switzerland). After curing for at least 24 hours at 20°C, the composites are cut and grinded into plates of approximately 10 × 5 × 1 mm^3. Within the resulting piezoceramic fiber composites, the PZT fibers are closely packed in a random order, as can be seen from Figure 1.

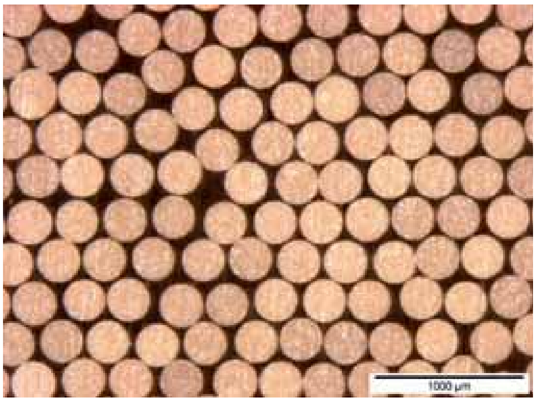

***Fig. 1:** Cross-section of a piezoceramic fiber composite test sample*

Further, the active phase of the composite, represented by the fibers, is continuous only in the thickness direction of the composite. Thin electrodes (Au, 50-100 nm) are deposited by sputter coating on both composite surfaces perpendicular to the thickness direction. Subsequent poling is performed with an electrical field strength of 2 kV/mm for 5 minutes at 80°C. Table 1 lists the measured values (average and standard deviation in %) of fiber diameter, dimensions, density and PZT volume fraction for the eight investigated piezoceramic fiber composite test samples.

***Table 1:** Average and standard deviation (in %) of fiber diameter, dimensions, density and PZT volume fraction of the investigated piezoceramic fiber composite test samples.*

property	***average***	***standard deviation***
Fiber diameter in µm	*290*	*1.7*
Length in mm	*10.47*	*0.1*
Width in mm	*4.99*	*0.7*
Thickness in mm	*1.00*	*0.3*
Density in g/cm³	*5.77*	*2.2*
PZT volume fraction	*0.718*	*2.7*

3 Characterization

Usually, piezoceramic materials are characterized on basis of the CENELEC [2] or IEEE standard [3]. In doing so, four samples that differ in their geometry and direction of polarization are required. For inhomogeneous materials, e.g., piezoceramic fiber composites, it is unfeasible to manufacture different sample geometries with identical material properties. On account of this fact, we use an alternative procedure.

Inverse Method The Inverse Method is able to identify all ten independent material parameters (plus one loss factor) of piezoceramics by means of only two sample designs: a thickness mode sample (T1) and a thickness shear mode sample (T2) [4], [5], [6]. In the case of piezoceramic fiber composites, we reduced the required number of test specimen to one by removing the electrodes of the T1 specimen and applying them according to T2 design (Fig. 2). Thus, both sample designs exhibit identical material.

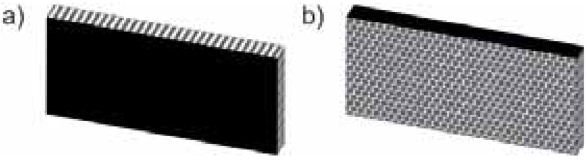

***Fig. 2:** Required test samples: a) thickness mode sample (T1), b) thickness shear mode sample (T2) with laterally applied electrodes; gray: piezo fibers; white: epoxy; black: electrodes*

Fig. 3 shows the principle of the Inverse Method. It is based on the minimization of deviations between measurements (2) and simulation results (5) of physical quantities by an appropriate optimization algorithm (e.g., Gauß-Newton, Levenberg-Marquardt) [6]. After each simulation step, the deviations between measurements and simulation results around the resonance frequencies are determined (6) and the subsequent parameter set is calculated (7). In doing so, the tensor of elasticity

$$\boldsymbol{c}^E = \begin{bmatrix} c_{11}^E & c_{12}^E & c_{13}^E & 0 & 0 & 0 \\ & c_{11}^E & c_{13}^E & 0 & 0 & 0 \\ & & c_{33}^E & 0 & 0 & 0 \\ S & & & c_{44}^E & 0 & 0 \\ & Y & & & c_{44}^E & 0 \\ & & M & & & \frac{c_{11}^E - c_{12}^E}{2} \end{bmatrix}, \tag{1}$$

the tensor of permittivity

$$\boldsymbol{\varepsilon}^S = \begin{bmatrix} \varepsilon_{11}^S & 0 & 0 \\ 0 & \varepsilon_{11}^S & 0 \\ 0 & 0 & \varepsilon_{33}^S \end{bmatrix} \tag{2}$$

and the tensor of piezoelectric coupling

$$\boldsymbol{e} = \begin{bmatrix} 0 & 0 & 0 & 0 & e_{15} & 0 \\ 0 & 0 & 0 & e_{15} & 0 & 0 \\ e_{31} & e_{31} & e_{33} & 0 & 0 & 0 \end{bmatrix} \tag{3}$$

are identified iteratively. Commonly, manufacturer data is used as an initial parameter set (4). In this case, the material set is not available and, consequently, one has to find an initial guess parameter set manually. Different abort criterias (8) are checked after each iteration step (e.g., convergence). If all criterias are fullfilled, the material parameter set is identified.

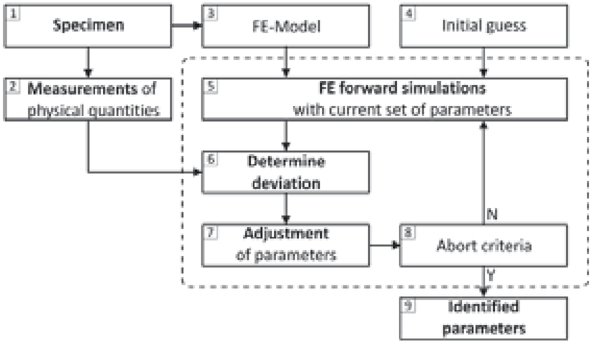

Fig. 3: Principle of the Inverse Method

Measurement setup Similar to the CENELEC standard [2], the frequency-resolved electrical impedance is used as physical quantity. For this, both samples are measured by means of an impedance analyzer (HP 4194A, Hewlett Packard) at a temperature of 20°C. Two spring pins connect and fix the sample (16034 test fixture, Hewlett Packard). As already mentioned, we only use one specimen, which is measured two times with different electrode arrangements (see Fig. 2).

FEM Simulations The numerical finite element method (FEM) simulations are realized by the tool CFS++ (Coupled Field Simulations). Three different homogenous FEM models are required for the Inverse Method: (i) a 3D model (length and width modes), (ii) a 2D model (thickness mode) of sample T1, and (iii) a 2D model (thickness shear mode) of sample T2. The simplification of using 2D models for simulations of the thickness modes is valid because the length direction has a negligible influence on the electric impedance at higher frequencies. This was verified through simulation-based studies.

Results Fig. 4 shows exemplary measurements and simulation results of the electric impedance at thickness mode of sample T1. It can clearly been seen that the Inverse Method leads to a very good fit between actual and simulated electric behavior of the piezoceramic fiber composites. The simulations are performed with the identified parameter set (see Table 2). The piezoelectric entity e_{15} is assumed to be zero due to a very small piezoelectric coupling of thickness shear mode.

***Table 2:** Average and standard deviation (in %) of identified parameters for eight piezoceramic fiber composites at 20 °C; c^E_{xy} in N/m^2; ε^S_{xy} in F/m; e_{xy} in C/m^2; density in kg/m^3.*

parameters	***average***	***standard deviation***
c^E_{11}	*27.79 · 10^9*	*6.31*
c^E_{12}	*12.86 · 10^9*	*12.40*
c^E_{13}	*14.04 · 10^9*	*7.13*
c^E_{33}	*54.74 · 10^9*	*3.01*
c^E_{44}	*5.29 · 10^9*	*9.13*
ε^S_{11}	*343.27 · 10^{-12}*	*0.01*
ε^S_{33}	*4.45 · 10^{-9}*	*2.30*
e_{31}	*- 967.59 · 10^{-3}*	*13.06*
e_{33}	*10.69*	*2.77*
e_{15}	*0*	*0*
damping α	*41.30 · 10^{-3}*	*4.41*
density ρ	*5770*	*2.22*

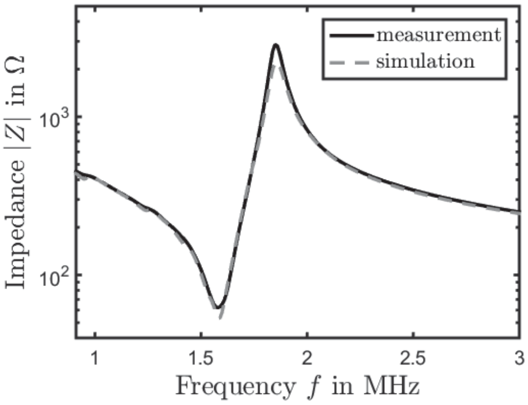

***Fig. 4:** Exemplary electric impedance curves for measurements and simulations of sample T1 thickness mode*

4 Displacement measurements

To verify the effective material parameters determined in Sec. 3, we compare simulated (average parameter values, see Table 2) and measured displacements of specimens. In doing so, the surface displacement is determined through a laser scanning vibrometer (Polytec PDV-300) at thickness mode of sample T1. Both graphs in Fig. 5 differ remarkably due to inhomogeneities of the piezoelectric fiber composite. Especially damping has a large influence on simulations of displacements near resonance, whereby small deviations of the identified loss factor could lead to significant differences between simulations and measurements at resonance. Consequently, it is not possible to replicate the mechanical behavior of piezoelectric fiber composites. However, numerical simulations lead to a good estimation of the mean surface displacement.

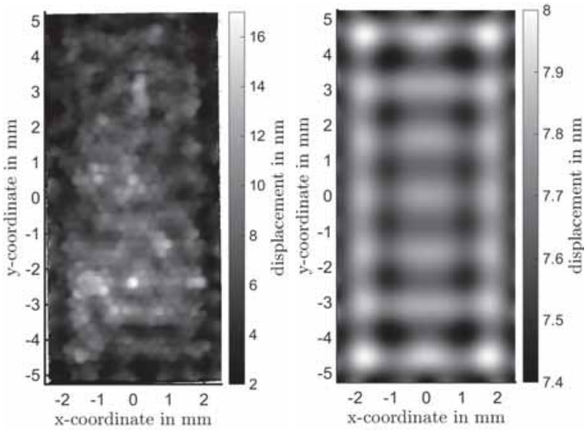

Fig. 5: *Measurement (left) and simulation (right) of surface displacement of sample T1 at thickness mode; frequency: 1.58 MHz; electrical excitation: V_{pp} = 8 V; mean displacement: 6.2 nm (measurement), 7.8 nm (simulation)*

5 Macromodel simulation

The influence of the matrix material on the composite's performance is of particular interest. To simulate the electrical and mechanical behavior, a macromodel is utilized which considers the specific structure of piezoceramic fiber composites. For this, precise material parameters of the involved materials SONOX® P505 and Araldite® 2020 are required. Plastics show a frequency dependent mechanical behavior, known as viscoelasticity. The frequency dependent elasticity modulus and damping are determined by means of an adapted Inverse Method [6,7].

Characterization of SONOX® P505 Similar to the characterization of piezoceramic fiber composites, the material parameters of SONOX® P505 are determined by means of the Inverse Method. Two bulk material samples (15 × 5 × 1 mm³) are produced from pressed PZT blocks and sintered under similar conditions like the piezoceramic fibers. Table 3 shows the material parameters of the characterized SONOX® P505 bulk material. Since the manufacturing process of bulk material and piezoceramic fibers differ, the determined parameters only approximate the real fiber material parameters.

Table 3: *Identified parameters for SONOX® P505 bulk samples at 20 °C; $\boldsymbol{c}_{xy}^{E}$ in N/m²; $\boldsymbol{\varepsilon}_{xy}^{S}$ in F/m; $\boldsymbol{e}_{xy}$ in C/m²; density in kg/m³ (* = density of thickness shear mode sample).*

parameters	***value***
c_{11}^{E}	*115.61 · 10⁹*
c_{12}^{E}	*67.07 · 10⁹*
c_{13}^{E}	*72.95 · 10⁹*
c_{33}^{E}	*119.58 · 10⁹*
c_{44}^{E}	*19.58 · 10⁹*
ε_{11}^{S}	*7.58 · 10⁻⁹*
ε_{33}^{S}	*5.66 · 10⁻⁹*
e_{31}	*-4.34*
e_{33}	*13.48*
e_{15}	*12.34*
damping α	*15 · 10⁻³*
density ρ	*7150 / 7710**

Characterization of Araldite® 2020 Due to the viscoelastic behavior of plastics, the frequency dependent material parameters of the used Araldite® 2020 has to be determined to achieve satisfactory simulation results. The Hooke's law describes the mechanical behavior of passive materials. The elasticity tensor for isotropic materials

$$\boldsymbol{c} = \begin{bmatrix} \frac{1}{E} & -\frac{\upsilon}{E} & -\frac{\upsilon}{E} & 0 & 0 & 0 \\ & \frac{1}{E} & -\frac{\upsilon}{E} & 0 & 0 & 0 \\ & & \frac{1}{E} & 0 & 0 & 0 \\ S & & & \frac{1}{G} & 0 & 0 \\ & Y & & & \frac{1}{G} & 0 \\ & & M & & & \frac{1}{G} \end{bmatrix} \tag{4}$$

$$G = \frac{E}{2(1+\upsilon)} \tag{5}$$

possesses two independent material parameters: elasticity modulus E and Poisson's ratio ν. In addition, a damping ratio ξ is defined.

To determine frequency dependent material parameters, we applied an adapted Inverse Method, which is based on measurements and numerical simulations of the mechanical transfer function [7]. Since the adapted Inverse Method was already introduced in further publications (e.g., [7], [8]), the method is described very shortly. Fig. 6 shows the measurement setup of the vibration transmission analyzer (VTA). An electromechanical shaker oscillates the one-sided clamped material sample harmonically. The frequency is varied stepwise from 5 Hz up to 4 kHz. Simultaneously, two laser Doppler vibrometers measure the velocity in oscillation direction near clamping v_R and free end v_M of the specimen. Thereby, the velocity transfer function

$$H(\omega) = \frac{v_M}{v_R} \tag{6}$$

is calculated. Similar to the Inverse Method for characterization of piezoceramics, the material parameters for the FEM simulations are updated iteratively until measured and simulated transfer functions are matching.

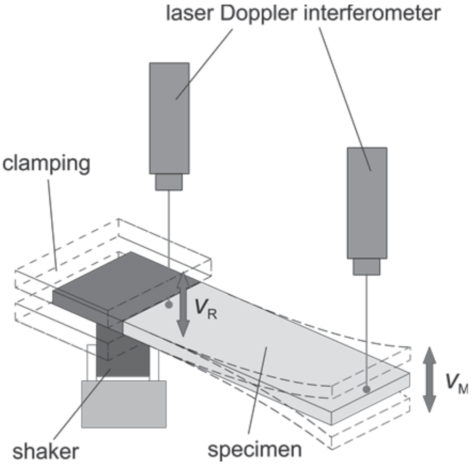

Fig. 6: *Measurement setup of Vibration Transmission Analyzer (VTA) [7]*

To consider viscoelasticity, the frequency dependent real and imaginary parts of elasticity modulus

$$E_{\mathrm{Re}}(\omega) = E_0 \frac{1+(d+1)\cos(\alpha\pi/2)\omega_{\mathrm{n}}^{\alpha}+d\omega_{\mathrm{n}}^{2\alpha}}{1+2\cos(\alpha\pi/2)\omega_n^{\alpha}+\omega_{\mathrm{n}}^{2\alpha}}, \tag{7}$$

$$E_{\mathrm{Im}}(\omega) = E_0 \frac{(d-1)\sin(\alpha\pi/2)\omega_n^{\alpha}}{1+2\cos(\alpha\pi/2)\omega_{\mathrm{n}}^{\alpha}+\omega_{\mathrm{n}}^{2\alpha}} \tag{8}$$

are introduced [9]. Therefore, the frequency dependent damping ratio becomes [9]

$$\xi(\omega) = \frac{E_{\mathrm{Im}}(\omega)}{2\cdot E_{\mathrm{Re}}(\omega)} = \frac{1}{2}\frac{(d-1)\sin(\alpha\pi/2)\omega_{\mathrm{n}}^{\alpha}}{1+(d+1)\cos(\alpha\pi/2)\omega_{\mathrm{n}}^{\alpha}+d\omega_{\mathrm{n}}^{2\alpha}}. \tag{9}$$

The Poisson's ratio is assumed to be constant over the whole frequency range. Fig. 7 shows the frequency dependent elasticity modulus and damping. Outside the measured frequency range (5 Hz – 4 kHz), the curves are only an estimation of the real values.

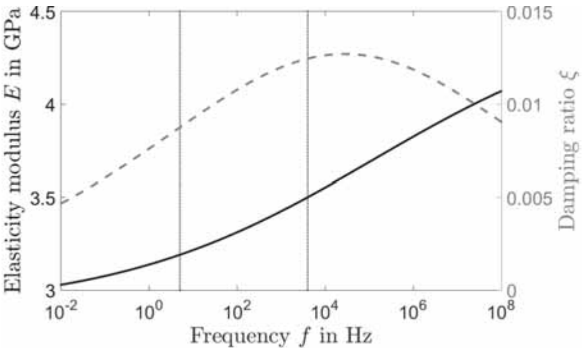

Fig. 7: *Frequency dependent elasticity modulus (black) and damping ratio (gray) of Araldite® 2020; vertical lines: measured frequency range; Poisson's ratio ν = 0.4*

Simulation with macro model

A detailed model of the piezoelectric fiber composite is required to reproduce the actual complex piezoelectric performance. In doing so, the fibers are aligned offset to one another (see Fig. 8). Only a quarter model is necessary due to symmetry. In addition, electrodes are attached orthogonally to the fibers.

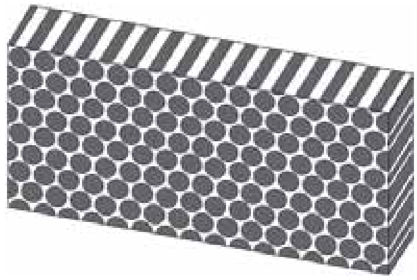

Fig. 8: *Detailed quarter macro model of piezoelectric fiber composite; gray: piezo fibers; white: epoxy; electrodes are not visible in this graph*

Fig. 9 compares the electrical impedance of the measurement and macro model simulations. It can clearly be seen that the macro model captures the real electrical behavior very well. Due to the homogeneous fiber arrangement of the macro model and without consideration of imperfections, both curves do not match exactly.

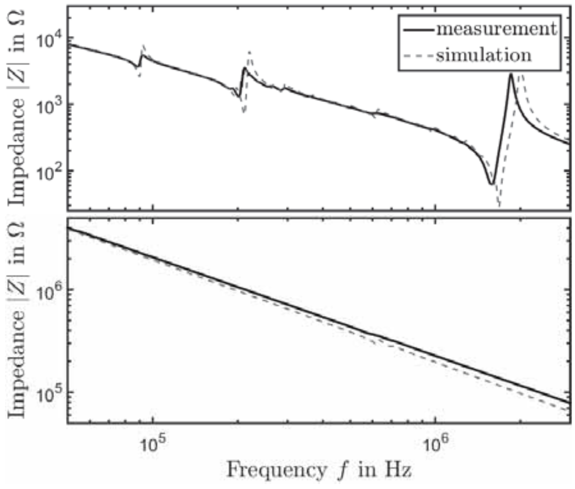

Fig. 9: *Comparison between measurements and simulation results of macro model. Frequency dependent electrical impedance of thickness mode sample T1 (top) and shear mode sample T2 (bottom)*

6 Conclusion and outlook

The Inverse Method enables a reliable identification of effective material parameters for piezoelectric fiber composites despite two involved materials and inhomogeneity. The results show a close match of simulated and measured electrical impedance curves and mean mechanical displacements. Future investigations will be conducted to determine the practicability of numerical simulations for various applications. At this, the frequency dependency of the effective material parameters of piezoelectric fiber composites will be included.

To replicate the detailed electrical and mechanical behavior of piezoelectric fiber composites, we simulated the electrical impedance by means of a macro model. For this, the involved active and passive materials were characterized separately. The frequency dependent material parameters for the passive material were determined through an adapted Inverse Method. The results show a very good match between simulations and measurements. In future work, these macro model simulations will be used in combination with the Inverse Method to optimize piezoelectric composites.

Literature

[1] Hohlfeld, K.; Gebhardt, S.; Schönecker, A.; Michaelis, A.: PZT components derived from polysulphone spinning process. In: Advances in Applied Ceramics 2015; Vol. 114(4), p. 231-237

[2] CENELEC Standard Piezoelectric properties of ceramic materials and components, EN 50324-2:2002

[3] IEEE Standard on Piezoelectricity, ANSI/IEEE Standard 176 - 1987

[4] Rupitsch, S. J.; Ilg, J.; Lerch, R.: Enhancement of the Inverse Method enabling the material parameter identification for piezoceramics. In: 2011 IEEE International Ultrasonics Symposium, p. 357-360, 2011

[5] Rupitsch, S. J.; Sutor, A.; Ilg, J.; Lerch, R.: Identification Procedure for Real and Imaginary Material Parameters of Piezoceramic Materials. In: IEEE International Ultrasonics Symposium Proceedings, p. 1214-1217, 2010

[6] Rupitsch, S. J.; Ilg J.: Complete Characterization of Piezoceramic Materials by Means of Two Block-Shaped Test Samples, In: IEEE Transactions on Ultrasonic and Frequency Control, Vol. 62. No. 7, p. 1403-1413, July 2015

[7] Ilg, J.; Rupitsch, S. J.; Lerch, R.: Determination of frequency and temperature dependent mechanical material properties by means of an Inverse Method, In Materials Characterization, Transactions on Engineering Science, 77, 2013

[8] Ilg, J.: Bestimmung, Verifikation und Anwendung frequenzabhängiger mechanischer Materialkennwerte, Verlag Dr. Hut, 2015

[9] Pritz, T.: Five-parameter fractional derivative model for polymeric damping materials, In: Journal of Sound and Vibration 265, 2003

Application of the Thermal Pulse Method to Evaluate the Polarization State of Piezoceramics

Eydam, A.; Suchaneck, G.; Gerlach, G.

TU Dresden, Institut für Festkörperelektronik, Dresden

Corresponding Author: Agnes Eydam, agnes.eydam@tu-dresden.de

Abstract

In this work, we introduce a thermal pulse method for non-destructive evaluation of the polarization state of integrated piezoceramics. Heating the sample with a pulsed laser leads to a pyroelectric current recorded in time domain within a very short measuring time. Two analytical models of the temperature distribution in the sample are presented. They match very well with a transient thermal analysis performed using the FEM package ANSYS. The pyroelectric current correlates directly with the mean temperature. Due to a too small signal-to-noise ratio of the measuring set-up, the experimental results do not yet agree completely with the modeling results.

1 Introduction

The fabrication of smart structures with integrated piezoelectric transducers requires control of the polarization state due to mechanical and thermal loads appearing during device fabrication.

Non-destructive methods for obtaining polarization profiles rely on an external excitation of the material leading to a local change of material properties [1]. A thermal excitation in terms of thermal waves or thermal pulses gives rise to a pyroelectric current which carries information on the polarization profile. In frequency domain, the Laser Intensity Modulation Method (LIMM) is well-established. Thereby, thermal waves travelling into the sample are generated by a periodically modulated laser beam heating the top electrode [2]. Recently, we have applied the LIMM to evaluate the polarization state of piezoceramic plates or fibers embedded in low temperature co-fired ceramics (LTCC) [3, 4], in thermoplastic structures [5], in aluminum die-casted modules [6], and in macro-fiber composite (MFC) actuators [3, 4].

In order to get a larger pyroelectric signal within a shorter measuring time, we have developed a thermal pulse measurement set-up [7]. Thermal pulses are applied with a pulsed laser and the signal is recorded in time domain [8].

In this work, we present analytical and FEM models describing the thermal pulse response and compare them to measurement results.

2 Theory

The pyroelectric current is described by a fundamental relation:

$$I(t) = \frac{A}{d}\int_0^d p(z)\frac{\partial}{\partial t}\Theta(z,t)dz\ , \tag{1}$$

where $p(z)$ is the pyroelectric coefficient depth profile (corresponds to the polarization distribution), $\Theta = T - T_0$ is the temperature difference to the environment, d and A are the thickness and the heated area of the piezoelectric plate, respectively.

Assuming a homogeneous polarization $p(z)=p_0$=const., eq. (1) simplifies to:

$$I(t) = \frac{A}{d}p_0\int_0^d \frac{\partial}{\partial t}\Theta(z,t)dz = Ap_0\frac{d\Theta_m}{dT}\ , \tag{2}$$

where $\Theta_m(t)$ is the temperature averaged across the sample. In this work, we use three models – two analytical and one numerical – with different levels of abstraction to determine the temperature distribution $\Theta(z, t)$.

2.1 Analytical models

The first model is a one-dimensional transient heat transfer model introduced by Bloß and DeReggi [9]. It considers an infinitely short laser pulse and accounts for the thermal mass of the electrode and the heat loss to the environment.

The assumptions that there is no heat loss from the top surface to the air and that the sample's backside is thermally coupled to an ideal heat sink result in:

$$\Theta(\xi,\tau)=\sum_{k=0}^{\infty}2\frac{\sin\left[x_k(1-\xi)\right]}{(1+r+r^2x_k^2)\sin x_k}\times\exp\left(-x_k^2\tau\right) \tag{3}$$

$\xi = z/d$ and $\tau = at/d^2$ are dimensionless variables of depth and time, respectively, a is the thermal diffusivity and r the ratio of the thermal mass of the electrode to that of the pyroelectric element. x_k are the solutions of a transcendent equation which is solved numerically. Inserting eq. (3) in eq. (2) yields for the time-dependent pyroelectric current:

$$I(\tau)=-Ap_0\frac{2a}{d^2}\sum_{k=0}^{\infty}\frac{x_k(1+\cos x_k)}{(1+r+r^2x_k^2)\sin x_k}\times\exp(-x_k^2\tau) \tag{4}$$

The second model uses the pulse-transient approach of Camia [10]. It presupposes the same approximations as for the first model: infinitely short laser pulse, top thermally insulated, back thermally coupled to an ideal heat sink, but it does not take into account the thermal mass of the electrode. The temperature distribution is then given by an infinite series of exponential terms:

$$\Theta(\xi,\tau)=\sum_{m=0}^{\infty}2\cos\left[\frac{(2m+1)\pi}{2}\xi\right]\times\exp\left[-\frac{(2m+1)^2\pi^2}{4}\tau\right] \tag{5}$$

Inserting eq. (5) in eq. (2) yields here for the pyroelectric current:

$$I(\tau)=-Ap_0\frac{a}{d^2}\sum_{m=0}^{\infty}(2m+1)\pi\cdot(-1)^m\times\exp\left[-\frac{(2m+1)^2\pi^2}{4}\tau\right] \tag{6}$$

2.2 Numerical Simulation

The third model is a FEM model solved by ANSYS 15.0.

The transient thermal analysis was performed by applying a heat flux on the top of the sample (in the area of the laser spot) for the duration of the laser pulse. The pulse width amounted to 500 ns. The backside of the sample was assumed to be an ideal heat sink. The initial temperature of the device was set to 20°C. The material properties are listed in table 1.

Table 1: *Material properties of the PZT plate [11].*

Density, g/cm³	***Thermal conductivity, W/mK***	***Specific heat, J/kgK***
7.8	*1.1*	*350*

3 Experimental Methods

Thermal pulse measurements were carried out by heating the samples with a pulsed laser diode (LC905D1S3J09UA, Laser Components, Olching, Germany) at a wavelength of 905 nm with an optical power of 65 W, a pulse width of 150 or 500 ns and a repetition frequency of 1 Hz. The pyroelectric current was transformed to a voltage by a current amplifier (DLPCA-200, Femto Messtechnik, Berlin, Germany) and the signal was recorded by a Waverunner® Xi-A oscilloscope (LeCroy, Chestnut Ridge, USA).

In the first step a simple PZT plate was studied. It had a size of (10 x 7 x 0.2) mm³ and was covered by a nickel-chromium electrode.

Afterwards measurements with integrated piezoceramics were performed on thermoplastic-compatible piezoceramic modules (TPM). They consisted of a metalized PZT functional layer (fiber arrays or monolithic wafers) which was positioned between two transparent thermoplastic carrier films of Polyamide 6 (PA6) comprising a meandered electrode.

4 Results and Discussion

4.1 Modeling results

The mean temperature of the sample and the resulting pyroelectric current were determined for the PZT plate with the three models mentioned above.

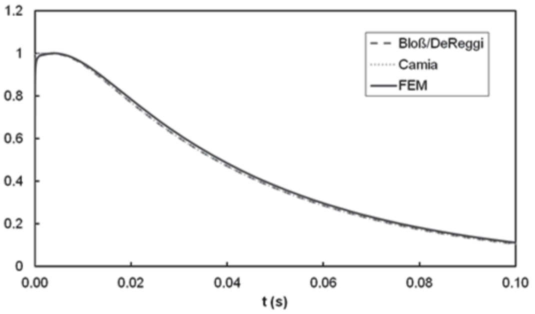

(a)

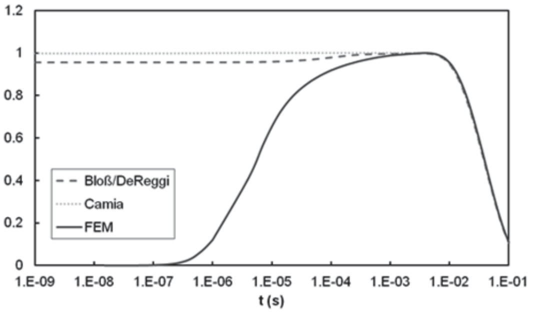

(b)

***Fig. 1:** Mean temperature of a PZT plate, determined by three different models (cf. section 2) with (a) linear and (b) logarithmic time axis.*

Fig. 1 illustrates the mean temperature over a time period of 0.1 seconds. The first model shows an initial slight increase of Θ_m, whereas the second model starts at the temperature maximum. The origin of this difference is the consideration of the electrode´s thermal mass in the first model, but not in the second one. The electrode acts as a thermal buffer, i.e., it absorbs the laser pulse first and slowly transfers the thermal energy to the pyroelectrics [9]. The FEM model shows the increase of the temperature from room temperature to a maximum value since the laser pulse has a given time duration of 500 ns. At longer times, the temperature decreases exponentially to room temperature.

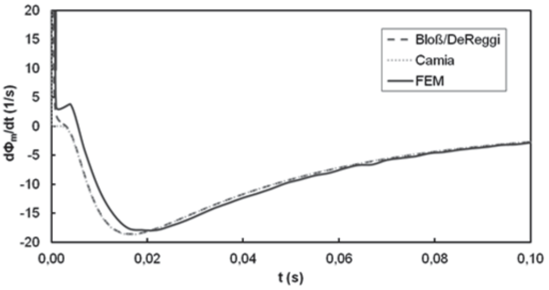

(a)

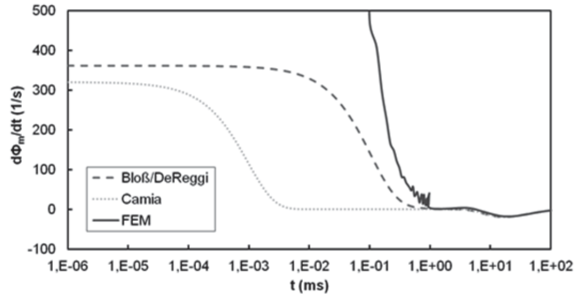

(b)

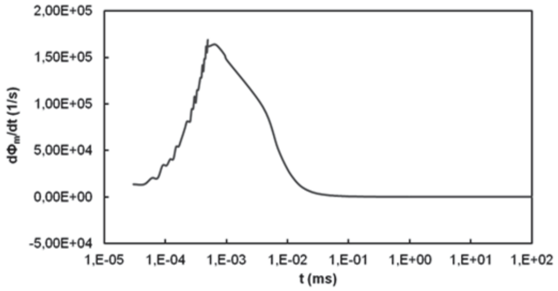

(c)

***Fig. 2:** Time derivative of the mean temperature (proportional to the pyroelectric current) of a PZT plate, determined by three different models (cf. section 2) with (a) linear and (b) logarithmic time axis. (c) shows once again the curve for the FEM model, but with another scaling of the ordinate.*

The pyroelectric current presented in fig. 2 is proportional to the time derivative of the mean temperature of the sample (cf. eq. (2)). In the analytical models, the current starts at a very high positive value due to initial heating and falls down almost immediately to a negative value since cooling corresponds to a negative current. After reaching a minimum the current slowly returns to zero, i.e. the sample returns to steady-state conditions. The FEM model in fig. 2(c) illustrates additionally the rise of the positive current during the laser pulse duration defining the heating period.

The three models are in very good qualitative agreement among one another.

4.2 Experimental Results

Fig. 3 and 4 illustrate the measured pyroelectric current for a simple PZT plate and for an embedded PZT plate (TPM). There is a very short initial negative peak followed by a large positive signal.

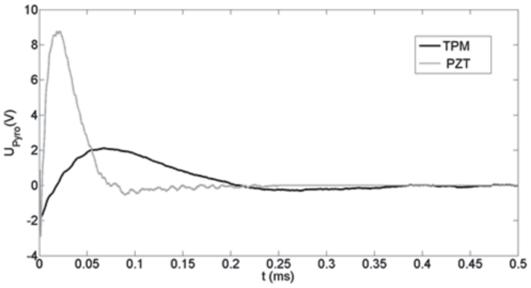

Fig. 3: *Time dependence of the output voltage of the current amplifier (10^8 V/A, 7 kHz bandwidth) for the PZT plate and the TPM for a pulse width of 150 ns.*

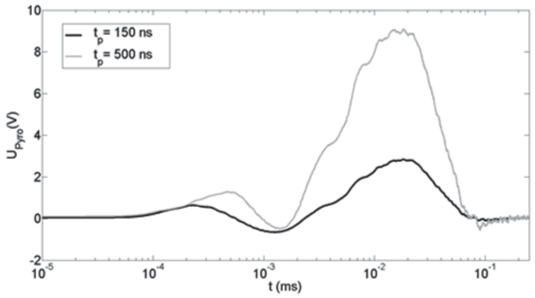

Fig. 4: *Time dependence of the output voltage of the current amplifier (108 V/A, 7 kHz bandwidth) for the PZT plate for a pulse width of 150 ns and 500 ns, respectively.*

In fig. 3, the time shift of the maximum signal for the embedded piezoelectric patch is a measure of the time delay caused by the heat transfer time through the thermoplastic top layer. PA6 is translucent in the near-infrared range so that the laser pulse is mostly absorbed by the top electrode of the integrated PZT plate. In our case, the time delay of 48 µs corresponds to an effective thickness of the PA6 layer of 8 µm with regard to the heat transfer time. The attenuation of the absorbed heat in the top PA6 layer results in a smaller maximum of the pyroelectric signal.

Fig. 4 illustrates that a longer pulse width leads to a higher heat input and thus a larger signal. The experimental data in fig. 4 is in qualitative agreement with the simulation in fig. 2c. Consequently, the experimental results manifest the initial heating of the piezoelectric plate. However, there is still a time shift between the signal maxima of the model and the experiment which is subject of further research.

On the other hand, the signal of the cooling period at longer times is still too noisy for a quantitative analysis. The time duration of the pyroelectric signal amounts to more than 100 ms in all three models. The thermal diffusion length:

$$\delta = \sqrt{2at} \qquad (7)$$

corresponds to the sample thickness for a time value of 5 ms. That means that the heat has reached the backside only after 5 ms and then it can be emitted to the heat sink. For measurement times of more than 1 ms mainly noise is present in the measured signal. It is dominated by 50 Hz noise. For further measurements, a 50 Hz notch filter will be used to reduce this noise contribution.

5 Conclusions

The temperature distribution in a PZT plate and the resulting pyroelectric current have been successfully described by two analytical models. The results have been confirmed by a FEM analysis. Further improvement of the thermal pulse set-up is required to reduce the signal-to-noise ratio. In the next step, a Fourier transform will be performed to analyze the signal in the frequency domain. This enables the application of the previously developed LIMM models to the thermal pulse method.

Acknowledgement

This research is supported by the Deutsche Forschungsgemeinschaft (DFG) in context of the Collaborative Research Centre/Transregio 39 PT-PIESA, subproject C8.

Literature

[1] Mellinger, A. et al.: Zerstörungsfreie Tomographie von Raumladungs- und Polarisationsverteilungen mittels Wärmepulsen (Non-destructive Space-charge and Polarization Tomography with Thermal Pulses). In: Technisches Messen 74, 2007, p. 437-444.

[2] Lang, S.B.; Das-Gupta, D.K.: Laser-intensity-modulation method, a technique for determination of spatial distributions of polarization and space charge in polymer electrets. In: J. Appl. Phys. 59, 1986, p. 2151-2160.

[3] Suchaneck, G.; Eydam, A.; Hu, W.; Krantz, B.; Drossel, W.-G.; Gerlach, G.: Evaluation of polarization of embedded piezoelectrics by the thermal wave method. In: IEEE Tran. Ultrason. Ferroelectr. Freq. Control 59 (12), 2012, p. 1950-1954.

[4] Eydam, A. et al.: Polarization characterization of PZT disks and of embedded PZT plates by thermal wave methods. In: AIP Conf. Proc. 1627, 2014, p. 31-36.

[5] Suchaneck, G.; Eydam, A.; Gerlach, G.; Gude, M.; Weber, T.; Winkler, A.: Evaluation of the pyroelectric response of embedded piezoelectrics by means of a Nyquist plot. In: Conf. Proc., IEEE- IUS, Prague (Czech Republic), July 21-25, 2013, p. 1969-1972.

[6] Eydam, A.; Suchaneck, G.; Schwankl, M.; Gerlach, G.; Singer, R.F.; Körner, C.: Evaluation of polarisation state of light metal embedded piezoelectrics. In: Adv. Appl. Ceram. 114(4), 2015, p. 226-230.

[7] Eydam, A.; Suchaneck, G.; Gerlach, G.: Characterization of the Polarization State of Embedded Piezoelectric Transducers by Thermal Waves and Thermal Pulses. In: Conf. Proc., AMA Conferences 2015 – SENSOR 2015, Nuremberg (Germany), May 19-21, 2015, p. 147-150.

[8] Collins, R.E.: Measurement of charge distribution in electrets. In: Rev. Sci. Instrum. 48, 1977, p. 83-91.

[9] Bloß, P.; DeReggi, A.S.: Electric-field profile and thermal properties in substrate supported dielectric films. In: Phys. Rev. B 62(12), 2000, p. 8517-8530.

[10] Camia, F.M.: Traité de Thermocinétique impulsionelle, Dunod, Paris, 1967.

[11] PI Ceramic GmbH: Werkstoffdaten, Spezifische Parameter der Standard-materialien, Datenblatt.
URL: http://www.piceramic.de/download/PI_Ceramic_Werkstoffdaten.pdf

Towards a Model-based High-resolution Ultrasonic Measurement System for Non-destructive Testing

Wüst, M.; Nierla, M.; Rupitsch, S. J.

Chair for Sensor Technology, Friedrich-Alexander-University of Erlangen-Nuremberg
Email: michael.wuest@fau.de

Abstract

This contribution is concerned with a technique to measure the physical dimensions of flaws in a multi-layered structure by using an ultrasonic system for non-destructive test (NDT). In order to achieve appropriate spatial resolution, an acoustic microscope working with a synthetic aperture focusing technique (SAFT) has to be established. However, standard SAFT algorithms are not matched with the individual geometry of the specimen perfectly. Therefore, a custom spatial filter kernel needs to be generated instead. For this purpose, a semi-numerical approach (SIRFEM) predicts the microscope output signals. Sound propagation in fluid media is modeled by using the spatial impulse response (SIR). Against that mechanical waves within the solid specimen are simulated by a higher-order finite element method (FEM). SIRFEM provides reliable output signals, which are then used to design the custom spatial filter kernel. We apply the technique to a water area containing point scatterers. An estimation of the system's spatial resolution will be given and the imaging results will be compared with those of the standard B-mode.

1 Ultrasound Imaging – General Problems

Common ultrasound (US) imaging systems usually have a lower spatial resolution compared to x-ray imaging system. But in special applications, i.e., NDT in high-density materials, x-ray imaging is very limited.

For high-resolution US imaging, focused transducers are available to obtain a sharp image around the focal length. These focused transducers have a lobe width, which depends on the axial distance to the focus area. The best lateral resolution in the image can be found at depth *F* where the focal zone is located. A point scatterer lying out of focus would be detected at several neighboring scan positions because of the expanded sound lobe. This leads to a blurred hyperbolic shape in the resulting raw image. Figure 1 shows a pulse-echo mode scan of a volume, which contains a point scatterer out of focus. The point's image is a blurred shape.

2 Delay-and-sum Algorithm

A well-known way to increase spatial resolution of an US image is to use the delay-and-sum (DAS) algorithm. Passmann and Ermert [1] introduced DAS for US imaging to overcome resolution limitations in the image. DAS corrects the signals of the single scans by an appropriate time delay and sums them up over *x*. This is executed for each point *P(x,t)* of the image.

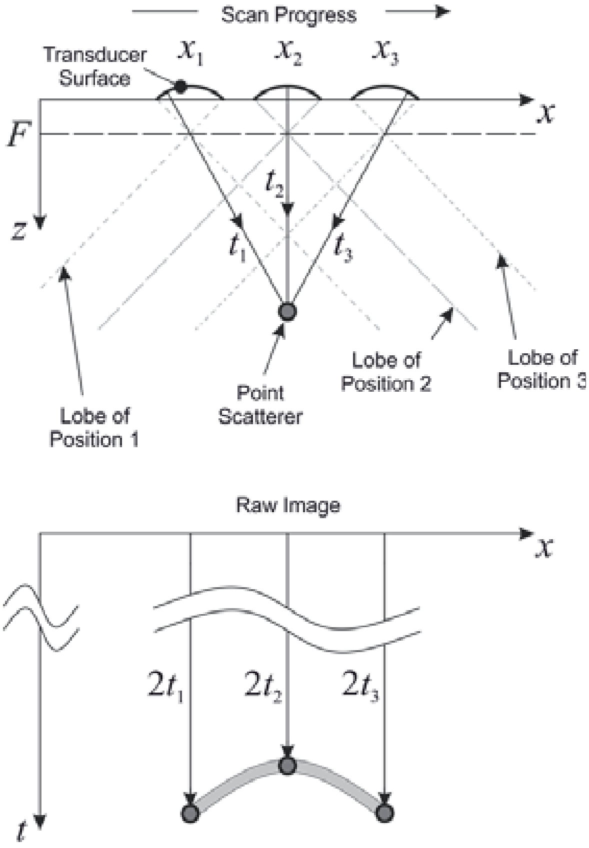

Fig. 1: *Scan and its resulting raw image of a point scatterer out of the transducer's focus. The distance from different transducer positions lead to different time-delays of the echo.*

The main equation for DAS SAFT reads as

$$A(t) = \sum_i w_i S_i(t - \Delta t_i) \tag{1}$$

where S is the time signal and w an apodization weight, which can be used to weight the signal amplitude over a point's lateral position in the image [2]. Equation 1 is evaluated for each point *P(x,t)* and the processed data is plotted as an image.

The main disadvantages are that DAS-SAFT considers neither the inner geometry of the specimen nor the shape of the transducer signal. A comparison to the model-based approach will be given in section 5.

3 Principle of Model-based SAFT

Imaging systems have a characteristic behavior, which can be described by the specific point spread function (PSF). For example, a camera's PSF is a characteristic quantity of the lens system and explains its sharpness. The resulting image *s(x,z)* can be interpreted as a 2D spatial convolution of the original reflectivity distribution *r(x,z)* with the system's PSF $h_{\mathrm{PSF}}(x\text{-}x',z',z)$ as shown in Fig. 2. The calculation at a given point *P(x,z)* is described by Eq. 2 [3]. The 2D spatial convolution at *P(x,z)* is a spatial integration over the complete image. Thus, the image coordinates *x'* and *z'* are introduced.

$$s(x,z) = \iint r(x',z') \cdot h_{\mathrm{PSF}}(x - x', z', z)\, \mathrm{d}x' \mathrm{d}z' \tag{2}$$

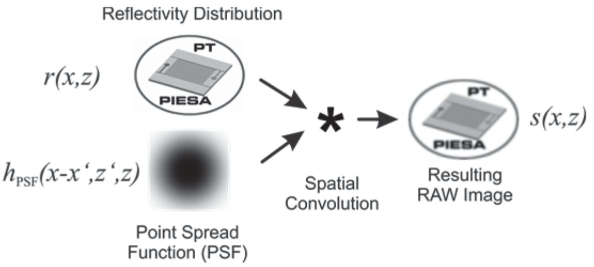

Fig. 2: *Spatial convolution of the target's reflectivity distribution r(x,z) and the imaging system's PSF* $h_{\mathrm{PSF}}(x\text{-}x',z',z)$ *leads to a blurred image s(x,z).*

The reverse way is a deconvolution of the raw image data with a simulated set of depth-dependent PSF signals $h_{\mathrm{PSF}}{}^*(x\text{-}x',z',z)$ [4]. This can be used for post-processing measured raw data (see Fig. 3). For noisy signals, deconvolution is an ill-posed problem which has to be solved via regularization approaches [5]. It should be noted that in this paper only simulated RF signals without any noise are examined to show the reliability of the implemented SAFT algorithm. So there is no need to regularize the dataset in this case. The image reconstruction based on Eq. 3 is named PSF SAFT.

$$r^*(x,z) = \iint s(x',z') \cdot h^*_{\mathrm{PSF}}(x - x', z', z) \mathrm{d}x' \mathrm{d}z' \tag{3}$$

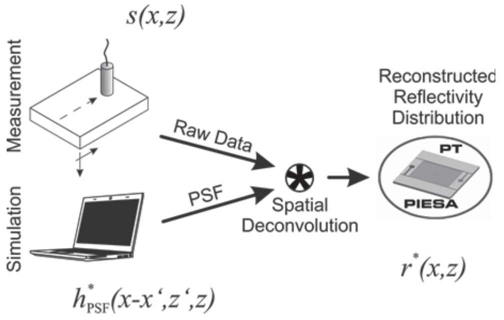

Fig. 3: *Spatial deconvolution of s(x,z) with the simulated PSF* $h_{\mathrm{PSF}}{}^*(x\text{-}x',z',z)$ *gives the reconstructed reflectivity distribution r*(x,z).*

4 Semi-numerical Simulation Approach

For simulating the system's PSF, we use a hybrid semi-numerical simulation approach called SIRFEM.

It is a combination of the spatial impulse response (SIR) method with the finite element method (FEM). SIR is applied in a fluid coupling medium (water) for pure longitudinal waves. The sound pressure can be calculated at each position for each time-step analytically. The base equations will be introduced later. FEM is used to model wave propagation in a solid medium where longitudinal as well as shear waves occur.

SIRFEM procedure

SIRFEM has been introduced by Rupitsch and Nierla in 2014 [6]. It is able to simulate the whole measuring process of an US measurement system from pulse transmission to echo detection. The setup contains a transducer, a fluid coupling medium and a specimen.

Frequencies up to about 50 MHz are feasible depending on the size of the geometry. The simulated measurement chain is presented by Fig. 4. The perfectly matched layer on top of the specimen area in Fig. 4 is used for wave damping to avoid spurious reflections at the boundaries of the model.

The following proceedings have to be performed (see also labels in Fig. 4):

- Set up an excitation boundary and its excitation signal. (1)
- Calculate sound propagation within the fluid coupling medium analytically by using the SIR. (2)
- Set up a special boundary for coupling SIR and FE. Use coupling points as excitation for the FE area. (3)
- Execute FE simulation to determine wave propagation within the solid specimen. Evaluate the resulting echoes at the surface of the specimen. (4)
- Take the evaluation points on the surface of the specimen and use them to excite the SIR area again. (5)
- Calculate the backward step SIR. (6)
- Write out the RF signal output. (7)

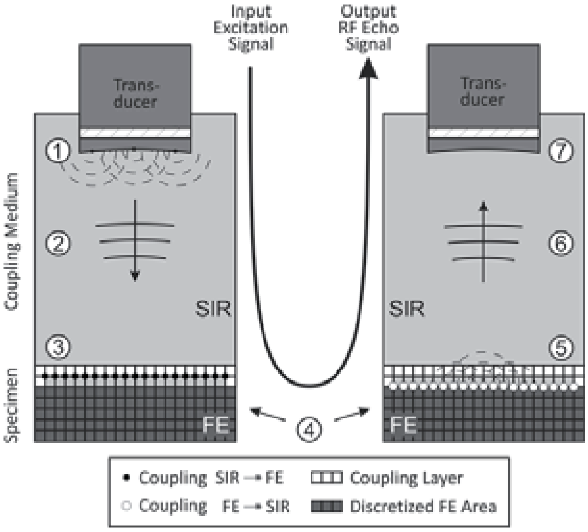

Fig. 4: *Simulation of the output signal using SIRFEM approach.*

There are some simplifications that have to be made to solve the problem:

- We only simulate 2D problems. 3D simulation is not practicable at the moment because of computing capacity. The required fine discretization of the finite elements for sufficient modelling of wave propagation is still too complex for efficient numerical simulation.
- We use a curved line to model the active transducer area and do not take the transducer's inner geometry into account at the moment.
- We assume that the active transducer area is a set of point sources like illustrated in Fig. 5.

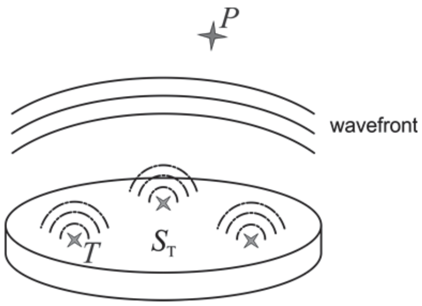

Fig. 5: *The active transducer area S_T is assumed to consist of point sources T, which emit spherical waves. The wavefront is the result of all point sources emitting waves.*

Derivation of SIR method

SIR method is based on the Rayleigh integral

$$\Phi(\mathbf{r}_P, t) = \int_{S_T} \frac{v\left(t - \frac{|\mathbf{r}_P - \mathbf{r}_T|}{c_0}\right)}{2\pi|\mathbf{r}_P - \mathbf{r}_T|} \mathrm{d}S_T(\mathbf{r}_T). \tag{4}$$

$\Phi(\mathbf{r}_P, t)$ is the acoustic potential and $v(t)$ the surface normal velocity of the active transducer area. $\mathbf{r}_P$ and $\mathbf{r}_T$ denote the position vectors of the points T and P, respectively. c_0 is the speed of sound in the surrounding fluid.

The corresponding sound pressure at P becomes

$$p_E(\mathbf{r}_P, t) = \rho_0 \frac{\partial}{\partial t} \Phi(\mathbf{r}_P, t) \tag{5}$$

where ρ_0 stands for the density of the surrounding fluid. Equation 5 can be rewritten as a convolution of $v(t)$ with the time derivative of the spatial impulse response h_S

$$\begin{aligned} & p_E(\mathbf{r}_P, t) \\ & = \rho_0 v(t) * \frac{\partial}{\partial t} \int_{S_T} \frac{\delta\left(t - \frac{|\mathbf{r}_P - \mathbf{r}_T|}{c_0}\right)}{2\pi|\mathbf{r}_P - \mathbf{r}_T|} \mathrm{d}S_T(\mathbf{r}_T) \\ & = \rho_0 v(t) * \frac{\partial}{\partial t} h_S(\mathbf{r}_P, t)\ . \end{aligned} \tag{6}$$

Generation of the PSF filter kernel

The procedure shown in Fig. 4 can be used to simulate a whole scan. For that, the relative position of the transducer to the specimen has to be modified step by step with a defined scan increment.

Moreover, we may simulate the PSF for setting up a filter kernel for SAFT. Figure 6 exemplifies the setup for obtaining a set of time signal data, which represents the depth-dependent PSF.

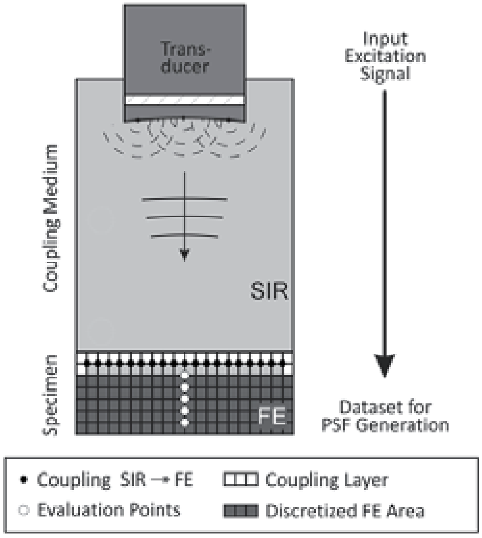

Fig. 6: *Basic simulation for generating the PSF filter kernel for PSF SAFT.*

The density oscillation at the evaluation points (marked white in Fig. 6) within the solid medium is used to calculate the PSF data. As there is no scatterer within the solid medium, we do not obtain directly the PSF data as transducer output signals. The PSF has to be generated by a two times convolution of the signal input with the time derivative of the SIR (see Eq. 7).

$$p_{\mathrm{out}}(\mathbf{r}_{\mathrm{P}},t) \propto \rho_0 v(t) * \frac{\partial}{\partial t} h_{\mathrm{S}}(\mathbf{r}_{\mathrm{P}},t) * \frac{\partial}{\partial t} h_{\mathrm{S}}(\mathbf{r}_{\mathrm{P}},t) \qquad (7)$$

5 Comparison between Raw Image, DAS and PSF SAFT as well as Estimation of Lateral Resolution

In order to demonstrate the advantages of PSF SAFT, we use a simple geometry without applying FEM for the first. PSF SAFT will be compared to the standard DAS SAFT and the raw image. The raw data is generated by a simulated scan. Thereby, the setup consists of water as fluid medium with five point scatterers in it, which are arranged along a line in depth direction. They have a distance of 2.5 mm in between. A 50 MHz transducer with the focal zone at a distance of 15 mm is assumed. It transmits a damped sine burst with length of three periods. A scan increment in *x* direction of 0.1 mm is used. Figure 7 displays the simulated B-mode raw image. The image of the point scatterers has the well-known hyperbolic characteristic. The lateral width is increasing with distance to the focal zone because of lobe width.

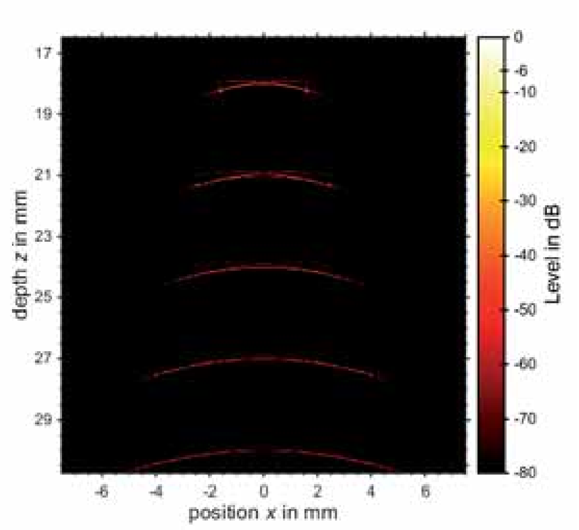

Fig. 7: *Raw image of the investigated scan.*

In Fig. 8, the DAS SAFT post-processed image of the five scatterers is given. Unfortunately, it is quite difficult to conduct a quantitative evaluation of the target sizes in axial as well as in lateral direction. In contrast, we have PSF SAFT in Fig. 9. It can be seen that the point scatterers are reconstructed very well. There are still artifacts in the near of the transducer's focal zone, but even their signal levels are quite low (-20 dB and lower). The integrated zoom windows make it clear that the reconstruction of the point is possible within the chosen lateral scan increment. In axial direction, there is a very short (about 0.02 mm) gaussian-like distribution with its maximum at the position of the scatterer. This might a consequence of both spatially and time-discrete sampling, but it has to be approved in later investigations.

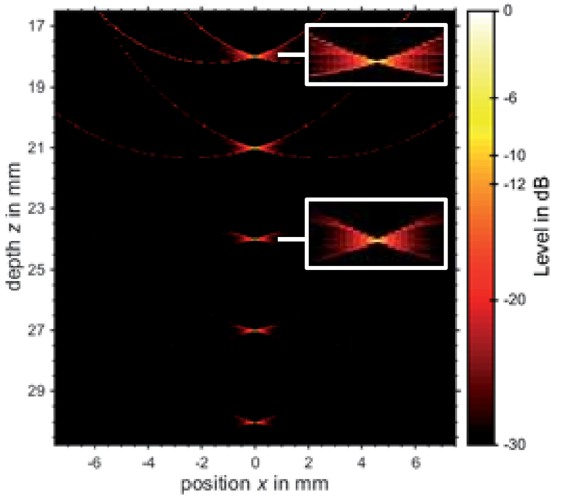

Fig. 8: *DAS SAFT image of the investigated scan.*

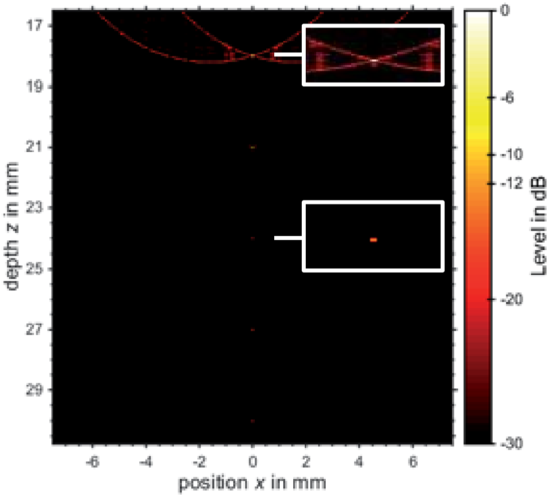

Fig. 9: *PSF SAFT image of the investigated scan.*

6 Conclusion and Outlook

We have presented an advanced SAFT approach for US non-destructive testing. It is a model-based algorithm that provides a matched filter kernel for the given specimen by simulating the PSF. To achieve this, we use a hybrid semi-numerical simulation approach for an US imaging system, called SIRFEM. SIRFEM is able to provide simulated output signals for a given geometry and an arbitrary transmit signal.

The post-processed SAFT image shows a optimized lateral and very high axial resolution. This is clear as we have a perfectly matched filter kernel for the presented simulated scan.

In a next step, we will build up an application, where a SIRFEM model is used as a filter kernel for measured RF data. The specimen will be investigated at a high-precision US scanning measuring station (Fig. 10), which was realized at the University of Erlangen. To establish a matched PSF, appropriate knowledge of the specimen's inner structure as well as of the excitation pulse's waveform is required.

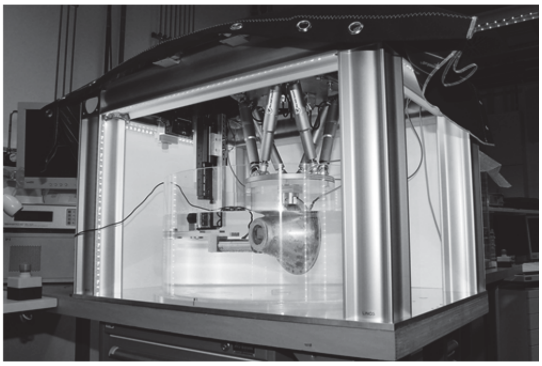

Fig. 10: *High-precision US scanning measuring station at the chair of sensor technology.*

Literature

[1] Passmann, C., Ermert, H.: A 100 MHz ultrasound imaging system for dermatologic and ophthalmologic diagnostics. IEEE Trans. Ultrason., Ferroelect., Freq. Contr., 1996, vol. 43, pp. 545-552.

[2] Frazier, C.H., O'Brien, W.D.: Synthetic Aperture Techniques with a Virtual Source Element. IEEE Trans. Ultrason., Ferroelect., Freq. Contr., 1998, vol. 45, pp. 196-207.

[3] Soumekh, M.: Synthetic Aperture Radar Signal Processing. Wiley-Interscience, New York 1999, pp. 7-17

[4] Opretzka, J., Vogt, M., Ermert, H.: A Model-Based Synthetic Aperture Focusing Technique for High-Frequency Ultrasound Imaging. EUSAR 2010, pp. 430-432.

[5] Rupitsch, S.J., Kindermann, S., Zagar, B.G.: Estimation of the Surface Normal Velocity of High Frequency Ultrasound Transducers. IEEE Trans. Ultrason., Ferroelect., Freq. Contr., 2008, vol. 55, pp. 225-235.

[6] Rupitsch, S.J., Nierla, M.: Efficient numerical simulation of transducer outputs for acoustic microscopes. IEEE Sensors 2014, pp. 1656-1659.

Fabrication of single fiber based piezocomposite transducers for 3D USCT

Hohlfeld, K.[1]; Zapf, M.[2]; Shah, G.[2]; Gebhardt, S.[3]; Gemmeke, H.[2]; Ruiter, N. V.[2]; Michaelis, A.[1,3]

[1]Technische Universität Dresden, Institute of Material Science, Chair of Inorganic Non-Metallic Materials, 01062 Dresden, Germany

[2]Karlsruhe Institute of Technology, Institute for Data Processing and Electronics, Hermann-v.Helmholz-Platz 1, 76344 Eggenstein-Leopoldshafen Germany

[3]Fraunhofer Institute for Ceramic Technologies and Systems IKTS, Winterbergstraße 28, 01277 Dresden, Germany

Corresponding author: Kai Hohlfeld, kai.hohlfeld@ikts.fraunhofer.de

Abstract

At Karlsruhe Institute of Technology (KIT) a 3D Ultrasound Computer Tomography (USCT) medical imaging system for early detection of breast cancer is under development. The 3D USCT II prototype operates with a multistatic setup of 2041 ultrasound transducers. Currently used transducers fabricated by dice-and-fill technique show approximately 2.5 MHz center frequency, 1 MHz bandwidth and 36° opening angle at 3 dB. To increase the region of interest (ROI) for a next USCT generation, the opening angle of a future transducer design should be increased to approx. 60° while other characteristics should be preserved or even improved. Piezocomposites based on single PZT fibers are investigated as promising cost-effective alternative to dice-and-fill transducers allowing for devices with increased opening angle. Moreover, high uniformity of a multitude of transducers made of same starting materials is expected.

1 Introduction

Early detection of breast cancer increases the chance of a cure. A diagnostic method for regular examinations should be as harmless as possible. 3D Ultrasound computer tomography (USCT) has the potential to detect tumors at an early stage. As indicated in figure 1, high specificity in the diagnosis of cancerous tissue is reached by analyzing information of three modalities (reflectivity, attenuation and speed of sound). Furthermore, ultrasound imaging avoids unintended side-effects, as caused by radiation (mammography) or contrast agents (magnet resonance tomography).

A 3D Ultrasound Computer Tomography (USCT) medical imaging system for early detection of breast cancer is developed [2, 3]. 2041 ultrasound transducers are arranged in a multistatic setup ensuring three-dimensional imaging. Currently, the transducers are fabricated by dicing fully electroded and poled piezoceramic wafers [4, 5, 6]. Always a set of four piezoceramic elements is connected to outer contact pads by attaching electrical wires by soldering. Each set of four piezoceramic elements works as one ultrasonic transducer (see figure 2). The gaps in-between the piezoceramic elements are subsequently filled with polyurethane polymer. The so manufactured transducers show approximately 2.5 MHz center frequency, 1 MHz bandwidth and 36° opening angle at 3°dB.

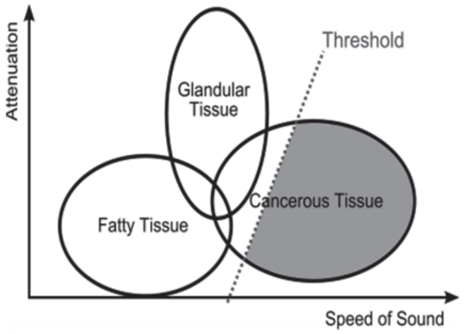

***Fig. 1:** Schematic of tissue type identification by means of acoustic characteristics, simplified from Greenleaf et al. [1]*

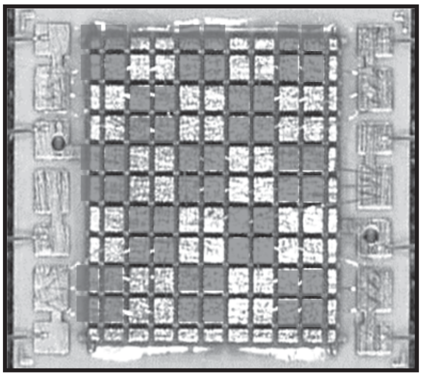

Fig. 2: *Structured piezoceramic wafer: always a set of four elements work as one transducer (active elements visualized by grey shading)*

First results from a pilot study with ten patients proved the capability of the developed 3D USCT prototype (see fig. 3) for 3D imaging of female breast [7]. Therewith, demands for optimizing the transducer design could be derived. The opening angle of the transducer has to be increased to approximately 60° to extend the region of interest (ROI) of the USCT system. To improve the acoustic behavior, a fabrication technique would be beneficial which allows an irregular arrangement of the transducers in order to inhibit spurious modes. Further, the acoustic properties shall differ as less as possible from one transducers to another.

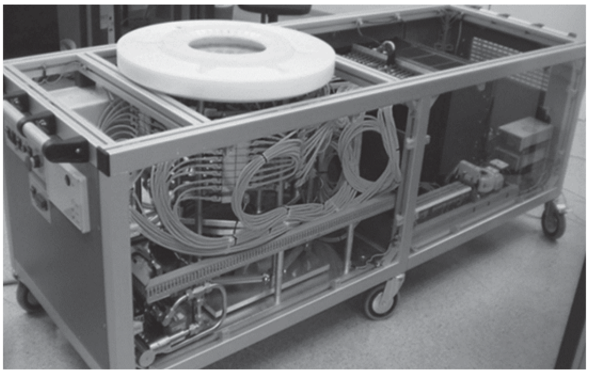

Fig. 3: *KIT 3D USCT prototype II, with open chassis exposing internals*

To meet these requirements, a new approach for the transducer fabrication is presented. It is based on piezocomposites made from single PZT fibers. The fiber diameter and the pattern of the arrangement are determined by means of acoustic simulations. First results on measured properties of the manufactured test samples are discussed with regard to fabrication accuracy and acoustic functionality.

2 Transducer design

A custom MATLAB written 3D simulation, based on Huygens waves, is used to characterize potential transducer designs. Dimensions and shape of the transducer are varied and analyzed with regard to the homogeneity and relative level of sound pressure, introduced phase-shifts as well as the frequency response over elevation and horizontal angle.

Results of sound pressure simulations are listed in table 1. An increased opening angle can be achieved by reducing the transducer dimensions. Reduction of the emission area of a rectangular transducer from 0.81 mm^2 to 0.16 mm^2 leads to an opening angle of 54° (3 dB at 2.5 MHz). A round transducer performs better in regard to pressure homogeneity over elevation and horizontal angles. Unfortunately, the smaller emission area causes a reduction of the sound pressure to 25 % [8] for both, rectangular and round transducers.

Table 1: *Opening angle and sound pressure depending on transducer specification*

Transducer size [mm]	*Area [mm^2]*	*Opening angle (3dB@2.5MHz)*	*Sound pressure*
0.9 (rect)	*0.81*	*22°*	*100 %*
0.4 (rect)	*0.16*	*54°*	*25 %*
0.456 (round)	*0.16*	*58°*	*25 %*

According to the simulation results, a technique is needed, which allows for the fabrication of round piezoceramic transducers with an active area of 0.16 mm^2. Piezoceramic fibers offer the possibility to fabricate round piezoceramic transducers with different diameters. For the considered design piezoceramic fibers with a diameter of about 460 µm are necessary. Additionally, inspired by compressive sensing ideas, piezoceramic fibers can be arranged in an irregular pattern (see fig. 4) to improve the signal-to-noise ratio (SNR) in resulting images by preventing periodic artifacts. Therefore, a technique to produce piezoceramic transducers with a specific arrangement of piezoceramic fibers has to be developed.

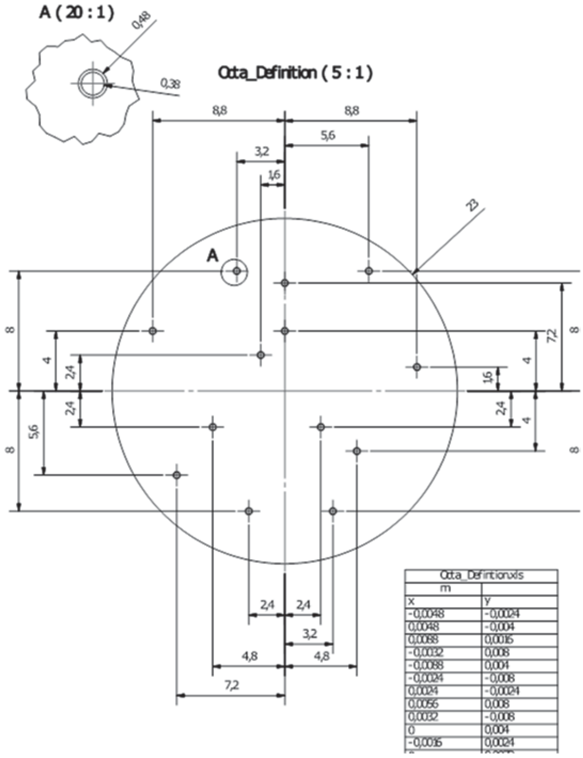

Fig. 4: Fiber arrangement: irregular distribution pattern

3 Test sample fabrication

A fiber spinning method based on a phase inversion process is used to produce dense piezoceramic fibers [9, 10]. Lead zirconate titanate (PZT) (SONOX® P505, CeramTec GmbH, Germany) is applied as piezoceramic material basis. The fiber diameter can be precisely set through adjusting the process parameters: nozzle diameter, extrusion velocity and running velocity [11]. By doing so, round PZT fibers with about 460 µm are derived.

Piezocomposite fabrication is schematically shown in figure 5. The PZT fibers are arranged in the required pattern with the aid of masks (1) and embedded into epoxy (EPO-TEK® 301-2, John P. Kummer GmbH, Germany) polymer (2). After curing for at least two days at 23°C, the composite block is diced into thin wafers (3). Electrodes (Au, 100-200 nm) are deposited on both sides of the resulting piezocomposites by means of sputter coating. Thereby, patterned electrodes are applied to one side to achieve individual addressable fibers (see fig. 6). An electrical field of 2 kV/mm is applied for 15 minutes to the electrodes for poling at room temperature.

For the acoustic evaluation, the piezocomposites are integrated into a cylindrical housing (see fig. 7). Electrically conductive polymer (Heraeus PC 3000 Epoxid, Ag 83% ± 1.5%) is used for contacting and insulating polymer (Vosschemie Flexovoss PU or Wacker Silgel 612A) for backfilling.

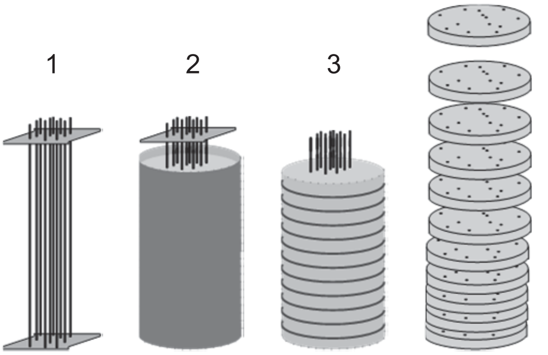

***Fig. 5:** Schematic of piezocomposite fabrication: 1) positioning of single piezoceramic fibers into specific positions defined by masks, 2) molding with matrix material; 3) cutting into discs with defined thickness according to operating frequency.*

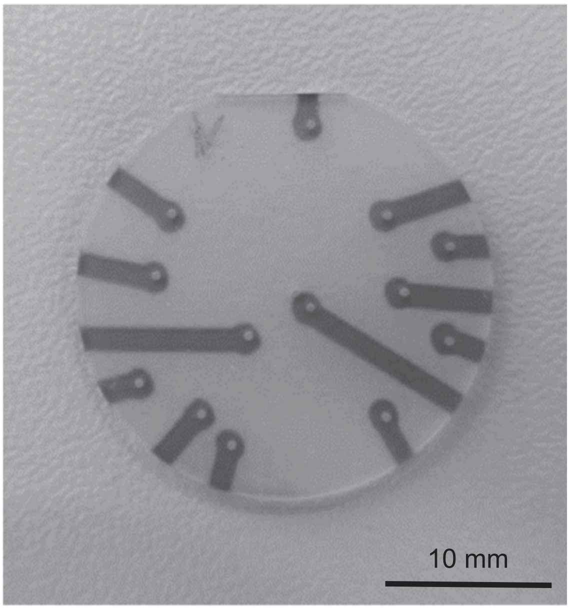

***Fig. 6:** Piezocomposite containing 13 individual addressable piezoceramic fibers, backside is common ground*

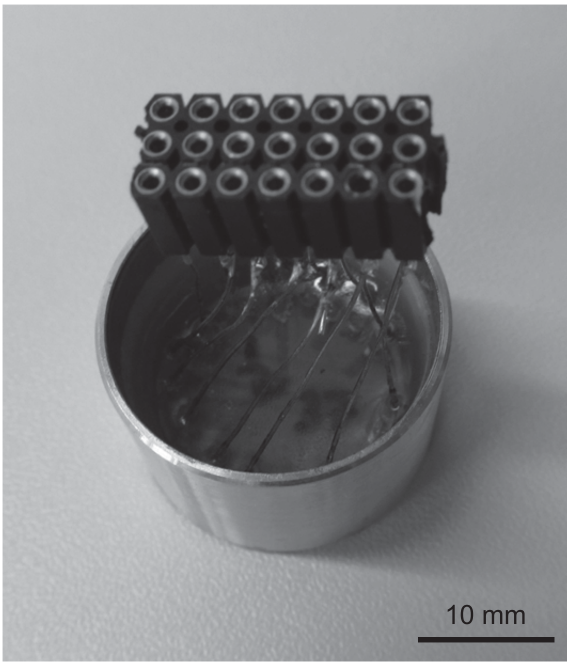

Fig. 7: *Test device #37 with integrated piezocomposite for acoustic measurement*

4 Results

The diameter of the fabricated PZT fibers is measured with 460 µm ± 2% (average and standard deviation), which represents a good match to the required transducer size and uniformity.

Table 2 lists the actual thicknesses of the fabricated piezocomposites in comparison to the targeted thickness. Ten samples were manufactured for each target thickness. Sample thickness was always measured at ten random positions. A very small deviation from target thickness as well as a good homogeneity is reached for the diced piezocomposite disks.

Table 2: *Target thickness and actual thickness (average ± standard deviation) of fabricated piezocomposites*

Target thickness [µm]	*Actual thickness [µm]*
450	*453 ± 2*
500	*501 ± 7*
550	*552 ± 4*
600	*605 ± 10*

First measurements of electrical impedance and acoustic pressure confirm the function of the single fibers as electromechanical transducers. They could be applied for sending and receiving ultrasonic waves. Furthermore, some of the fiber based transducers show an increased opening angle of about 60°. Unfortunately, the expected uniformity in acoustic properties from one transducer to the other could not be observed. Beside that, the fiber transducers produce a sound pressure below the expected 25 %. Several individual transducers even exhibit particularly weak or no response at all. A preliminary microscopy analysis showed no cracks or other indications of mechanical damage.

Since the underlying reasons for the variation of the acoustic properties are not identified by now, this is the focus of following investigations. Therefore, PZT fiber homogeneity as well as assembly and packaging technology will be examined in detail. Quantitative results regarding to transducer behavior will be presented in [12].

5 Conclusions

Piezoceramic composites with specific arrangement of PZT fibers allow for an effective and efficient manufacture of arbitrary planar positioned 2D transducer apertures, overcoming limitations of the conventional dice-and-fill process. Transducer size and thickness can be easily adjusted to customs needs. An excellent spatial reproducibility was achieved for both, fiber transducer diameter and piezocomposite thickness among the produced samples.

Nevertheless, some of the hopes for benefits do not materialize. Although for some fiber transducers the required and expected increased opening angle could be shown, the expected uniformity with regard to further ultrasound characteristics could not be observed. The underlying reasons have to be cleared. Furthermore, options for improvement are advanced matching and backing for greater bandwidth and opening angle as well as an optimized fiber material selection which can increase the sound pressure level of the individual transducers.

In further, the contacting of the individual piezocomposites are critical process aspects. While individual contacting and backing using polymers worked in principle for the test samples, these process steps lack high scale processability and general reliability. Here, additional improvements are needed to increase reliability and effectiveness of these fabrication steps.

Acknowledgement

This research is supported by the Deutsche Forschungsgemeinschaft (DFG) in context of the Collaborative Research Centre/Transregio 39 PT-PIESA, subproject A01.

Literature

[1] James F Greenleaf, J. F.; Bahn. R. C.: Clinical Imaging with Transmissive Ultrasonic Computerized Tomography. In: IEEE Transactions on Biomedical Engineering BME-28.2 (1981)

[2] Ruiter, N. V.; Zapf, M.; Dapp, R.; Hopp, T.; Gemmeke, H.: First in vivo results with 3d USCT. In: Proc. IEEE International Ultrasonics Symposium, 2012.

[3] Ruiter, N. V.; Schwarzenberg, G. F.; Zapf, M.; Gemmeke, H.: Conclusions from an Experimental 3D Ultrasound Computer Tomograph. In: IEEE NSS MIC, Dresden, 2008.

[4] Schwarzenberg, G.; Zapf, M; et al.: Aperture optimization for 3D ultrasound computer tomography." In Proc. IEEE UFFC Symp, 2007.

[5] Ruiter, N. V.; Göbel, G.; Berger, L.; Zapf, M.; Gemmeke, H.: Realization of an optimized 3D USCT. In: Proc. SPIE 7968, Medical Imaging 2011: Ultrasonic Imaging, Tomography, and Therapy, 796805 (March 24, 2011); doi:10.1117/12.877520

[6] Göbel, G.: Entwicklung von Ultraschall-sensorarrays mit miniaturisierten Komponenten. Diplomarbeit: Institut für Prozessdatenverarbeitung und Elektronik (IPE) Forschungszentrum Karlsruhe, 2002

[7] Ruiter, N.V.; Zapf, M.; Dapp, R.; Hopp, T.; Gemmeke, H.: First Results of a Clinical Study with 3D Ultrasound Computer Tomography. In: IEEE Ultrasonics Symp., 2013.

[8] Zapf, M.; Dapp, R.; Hardt, M.; Henning, P. A.; Ruiter, N. V.: Fast k-Space based evaluation of imaging properties of ultrasound apertures. In: Proc SPIE Medical Imaging, 2011.

[9] Scheithauer, U.; Seffner, L.; Gebhardt, S.; Schönecker, A.; Michaelis, A,: Verfahren zur reproduzierbaren Herstellung keramischer Formkörper. Patent DE 10 2008 056 721, 22 June 2011

[10] Hohlfeld, K.; Gebhardt, S.; Michaelis, A.: Piezoelectric transducers on the basis of free-formed PZT components. In: 2013 IEEE International Symposium on the Applications of Ferroelectric and Workshop on the Piezoresponse Force Microscopy (ISAF/PFM), 21-25 July 2013, p. 279-282, doi: 10.1109/ISAF.2013.6748675

[11] Hohlfeld, K.; Gebhardt, S.; Schönecker, A.; Michaelis, A.: PZT components derived from polysulphone spinning process. In: Advances in Applied Ceramics 2015; Vol. 114(4), p. 231-237

[12] Zapf, M.; Hohlfeld, K.; Shah, G.; Ruiter, N. V.; Gebhardt, S.; Michaelis, A.: Evaluation of piezo composite based omnidirectional single fibre transducers for 3D USCT. In: Proceeding IEEE IUS 2015 (abstract accepted)

Ultrasound Computer Tomography for early breast cancer diagnosis

Ruiter, N. V.; Zapf, M.; Hopp, T.; Gemmeke, H.

Karlsruhe Institute of Technology, Karlsruhe, Germany

Abstract

Ultrasound Computer Tomography (USCT) is a promising new medical imaging modality for early breast cancer diagnosis. The main advantages of USCT are simultaneous recording of reflection, attenuation and speed of sound images, high image quality and fast data acquisition. Building such a device for clinical practice is very demanding due to many thousand ultrasound transducers, hundreds of parallel channels for fast DAQ and computationally very demanding reconstruction algorithms. Currently, the first 2D systems have become available for clinical evaluation. At KIT we developed and tested the first full 3D USCT system and are conducting clinical studies.

1 Introduction

A promising candidate for sensitive imaging of breast cancer is ultrasound computer tomography (USCT). The possible benefits of USCT have been known for a long time. First publications in this field date back to the 70s, e.g. by Schomberg [1]. The main advantages of such USCT systems are simultaneous recording of reflection, attenuation and speed of sound images, high image quality, and fast data acquisition. Due to the defined patient positioning and no breast deformation, the volume images of the female breast are reproducible.

Building such a device for clinical practice was for a long time not successful - mostly due to the huge data rate and the time-consuming image reconstruction. Currently, the first 2D and 2.5D systems have become available for clinical evaluation [2,3]. Usually modern USCT systems implement unfocused ultrasound emission and reception to reconstruct optimally focused reflection images by synthetic aperture post-beamforming. However, in most systems post-beamforming is only applied in one imaging plane. This leads to large slice thickness with limited depth of field, loss of out-of-plane reflections, and large number of movement steps to acquire a stack of images of the whole volume [3]. 3D USCT, using spherical wave fronts for imaging, overcomes these limitations.

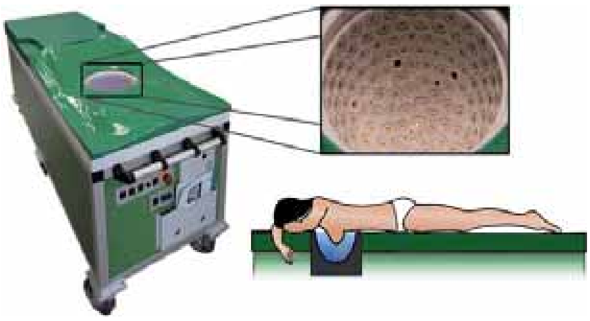

Fig. 1: *3D USCT with patient bed (left), transducer aperture (top right) and patient position (bottom right).*

2 3D USCT System

The prototype has a semi-ellipsoidal aperture with 628 emitters and 1413 receivers. Approx. spherical wave fronts are generated by emitting with a single emitter at 2.5 MHz (approx. 50% bandwidth). Rotational and translational movements, so-called aperture positions, of the complete transducer aperture create further virtual positions of the ultrasound transducers. The aperture in form of a semi-ellipsoid was optimized in respect to the isotropy of the 3D point spread function (PSF), the image contrast and the illumination [4]. The data acquisition is carried out with an FPGA based system, which can store up to 40 GB of A-scans. The digitalization is performed by 480 parallel channels (12 bit @ 20 MHz), enabling data acquisition at one aperture position in ten seconds.

After digitization, the parallel data streams are processed by the FPGAs of the data acquisition hardware. The signals are band pass filtered (1.67 to 3.33 MHz @ -60 dB) and the data rate is reduced by a factor of 6, performing a band pass undersampling. The reduced data is then stored in the internal 80 GB memory buffer.

Table 1: *Specification of KIT's 3D USCT*

Parameter	***Value***
No. of parallel channels	480
Digitization	20 MHz at 12 bit
On-board memory	80 GBytes
Multiplex factor	3
No. TAS	157
No. emitters	628
No. receivers	1413
Diameter TAS	28 mm
Emitters / TAS	4
Receivers / TAS	9
Area individual transducer	(0.9 mm)^2
Opening angle	38.2° at -6 dB (SD ± 1.5°)
Resonance frequency	2.7 MHz (SD ± 0.08 MHz)
Bandwidth	1.5 MHz at -6 dB (SD ± 0.15 MHz)
Sound pressure	5.9 kPa at 12 cm (SD ± 0.63 kPa)

Using this approach it is possible to store up to 47 data sets at different aperture positions in one data acquisition process. The whole device is embedded in a patient bed as shown in Fig. 1.

Sound pressure is generated and received using lead zirconate titanate (PZT) composites. One quadratic module of PZT composite contains nine receivers and four emitters. Each transducer head is embedded in the Transducer Array Systems (TAS) casing including its pre-amplifier and control electronics. Each transducer has a quadratic area of (0.9 mm)^2 which is composed of a two by two structure of 400 µm times 400 µm sub-elements. The gap between the sub-elements is 100 µm. The transducer array with attached electronics is then positioned within the TAS casing.

Each TAS contains a temperature measurement device for tracking the temperature distribution and shift at 157 positions during measurements. Additionally, two calibrated PT100 temperature sensors are embedded in the TAS holder to enable increased accuracy. The measured temperature distribution can be applied during the image reconstruction to estimate the distribution of the speed of sound in the contact medium water. Table 1 summarizes the system parameters.

3 Image Reconstruction

The applied reconstruction algorithm for reflectivity images is the 3D synthetic aperture focusing technique (SAFT), which can be described by the following equation:

$$R(\vec{x}) = \sum\nolimits_{j,k} \hat{a}(\vec{x}, \vec{e}_j, \vec{r}_k) T(A_{j,k}(\vec{x})) \tag{1}$$

where R denotes the reconstructed qualitative volume of local impedance differences at the reconstruction point $\vec{p}$. T comprises the preprocessing steps, $A_{j,k}$ is the A-scan acquired at emitting position $\vec{e_j}$ and receiving position $\vec{r_k}$. Norton and Linzer [5] showed for ideal conditions, i.e. continuous aperture, isotropic point scatterers, no attenuation, that SAFT solves the inverse problem of calculating the local impedance differences.

The time t is related to the point $\vec{p}$ by

$$t(\vec{p}) = \frac{\|\vec{p}-\vec{e_j}\| + \|\vec{p}-\vec{r_k}\|}{\hat{c}(\vec{p},\vec{e_j},\vec{r_k})} \tag{2}$$

For the simplest reconstruction the harmonic mean of the speed of sound may be assumed to be constant $\hat{c}(\vec{p},\vec{e_j},\vec{r_k}) = \hat{c}$, e.g. the speed of sound in water at the temperature measured during image acquisition. For high resolution imaging the mean speed of sound on the path from the emitter to the imaged point and from the imaged point to the receiver needs to be calculated from the simultaneously acquired speed of sound map of the breast. The factor $\hat{a}(\vec{p},\vec{e_j},\vec{r_k})$ can be applied to correct for the attenuation on the path. It is estimated from the attenuation map of the breast [6].

Acquiring unfocused ultrasound facilitates new possibilities for signal preprocessing, as the data can be accessed before the focus of emission is generated. The A-scans are preprocessed using a matched filter, followed by envelope transformation, detection of the local maxima and convolution with an optimal pulse [7].

The computing system for reconstruction consists of a reconstruction PC (4 x AMD Opteron Octacore, 2.3 GHz, 256 GB RAM) and an external GPU crate (One Stop Systems) connected via a second generation PCI-Express bus. The external GPU crate is equipped with four Nvidia Geforce GTX 590 cards, with two GF100 GPUs per card. This results in a total number of eight separate CUDA devices for image reconstruction [8].

The speed of sound and attenuation volumes are reconstructed using a ray-based approach. The transmission signals are detected and the time-of-flight and relative signal energy, respectively, are applied in an algebraic reconstruction technique (ART) to calculate the resulting images. A compressive sensing algorithm, i.e. 3D adaption of TVAL3, using total variation minimization is employed for optimization. Refer to [9] for a more detailed description.

The resulting USCT reflectivity, speed of sound and attenuation images can be viewed separately, directly overlaid or overlaid with an applied threshold. The direct overlay codes the speed of sound or attenuation in a color map and the reflectivity as grey values. The overlay is done by adding the color-coded image to the grey image with an adjustable degree of transparency. The thresholded-fused image follows the method in [10], where a color image only marks image areas where the speed of sound and attenuation are above given thresholds, and then is overlaid on top of the reflectivity volume.

4 Results

We evaluated our KIT-3D USCT in a pilot in-vivo study. The primary aim of this study was to test the USCT device on ten patients in respect to

1. Data acquisition and image reconstruction protocols
2. Fused display of the multimodal USCT images
3. Process of data acquisition and its optimization
4. First indications of breast image quality for different tissue types, implants and cancer

All necessary permissions to carry out a clinical study have been acquired. The patients included in the study were acquired during the standard MRI examination at the University Hospital Jena. In all MRI examinations a standardized protocol according to international guidelines was used. The applied magnetic field strength was 1.5 Tesla (Magnetom Avanto; Siemens Medical, Erlangen, Germany). It started with 2D dynamic T1w spoiled gradient echo scans before and after intravenous application of Gd-DTPA (Magnevist, Bayer/Schering, Leverkusen, Germany). For standardized injection power injector devices were used (Medrad, Spectris, Medrad, Pittsburgh, USA). Additionally, a T2w TSE scan in identical slice position was acquired. The MRIs are sliced transversally, the in-plane resolution is 0.9 mm, and the slice thickness is 3 mm without gap.

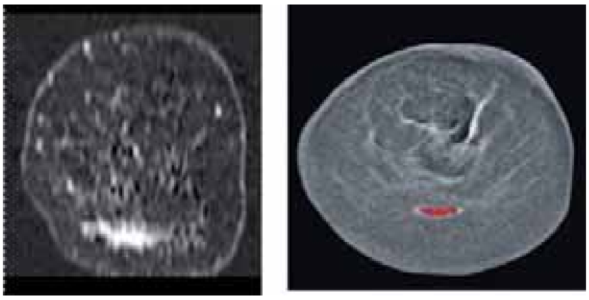

Fig. 2: *74 year old patient with large breast cancer in the left breast. Left: Frontal MRI subtraction slice. Right: USCT slice at approx. the same position as tresholded-overlay.*

The patients first had their scheduled MRI examination and were then - if they met the inclusion criteria - asked to participate in the study. If they agreed, the USCT image acquisition was carried out directly after the MRI, so that the MRI images could be used as ground truth for comparison to the USCT volumes.

For emission a linear frequency coded chirp was employed with 2.5 MHz center frequency, 1 MHz bandwidth and 12.8 µs duration. The main lobe of the optimal pulse was set to 2 µs, which corresponds to a Full Width Half Maximum (FWHM) of the point spread function of approx. 1.5 mm, and thus is comparable to the MRIs.

For most patients the breast diagnosed with lesions was imaged with ten aperture positions. The contralateral breast was also imaged using four aperture positions.

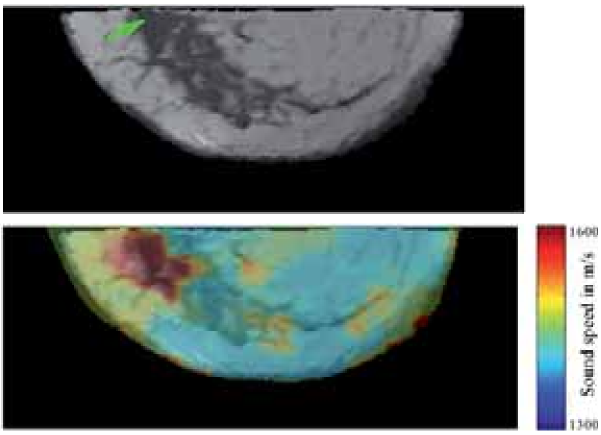

Fig. 3: *Transversal slice image of a patient with an inflammatory carcinoma (green marker) in the registered T1 MRI image (top) and fused image of the MRI with the USCT sound speed image (bottom). The sound speed information is color-coded and rendered semi- transparently on the MRI slice.*

For two patients, who were diagnosed with large cancer masses, only the breasts with lesions were imaged with 13 aperture positions. Fig. 2 and 3 show two exemplary results.

For comparison of the reconstructed USCT images to an established modality, MRI images were used. In MRI the breast is positioned pendulous in prone position within a dedicated breast coil. However, due to buoyancy in USCT and deformations of breast when contacting the MRI coil, direct voxel to voxel comparison is not possible. Due to immersing the breast into a water bath, it buoys up resulting in a shortening of approx. 15% in anteroposterior direction. Complex interactions within the breast result in nonlinear deformations of tissue structures.

After reconstructing all USCT modalities, a registration and image fusion was applied to achieve comparable images and visually evaluate the USCT images against the ground truth MRI (Fig. 3) [11].

5 Future System

The aims of the pilot study could be fully reached and the results led to further optimization of the system. We learned that the breast shape in USCT and MRI of the same breast was for most patients very different. This is mainly due to the buoyancy of the breast in water and partly due to deformation of the large breasts by the MRI coil. Central positioning of the breasts in the USCT is crucial, yet this was hard to realize during the clinical study. Misplacements led to inhomogeneous illumination of reflectivity volumes outside the ROI. The speed of sound volumes seem to be most specific for breast cancer diagnosis, at least for the small number of imaged patients with mainly large lesions. The current ray-based reconstruction for transmission tomography limits the resolution to 12 mm. Furthermore, the current aperture design reduces their image quality by introducing artifacts into the images [12].

The aim for a future system was to design a new aperture extending the properties for reflection tomography of the current aperture to a larger ROI fitting the buoyant breast and minimizing the artifacts in transmission tomography. The method should be generic in such a way that for given design parameters and hardware limitations, e.g. number of channels for data acquisition and diameter of aperture, an approximately optimal aperture can be generated and compared quantitatively to other apertures. The optimization method [13] resulted in a larger opening angle of the transducers, a larger diameter of the aperture and an approximately homogeneous distribution of the transducers, with locally random distances.

The transducers will act as emitter and receiver. In order to distribute the individual transducers more uniformly on the aperture we chose 128 TAS with 4.3 cm diameter and 18 transducers each. Thus 1.6 times more transducers will be available. Only two aperture positions will be necessary to acquire the same amount of data compared to 12 aperture positions in the current system leading to reduced measurement time. Fig. 4 und 5 show resulting TAS and aperture in comparison to the current system.

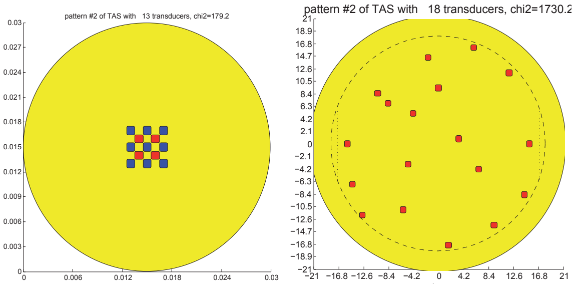

__Fig. 4:__ Distribution of transducers on each TAS for the current and future USCT; their diameter is 28 mm (left) nd 43 mm (right).

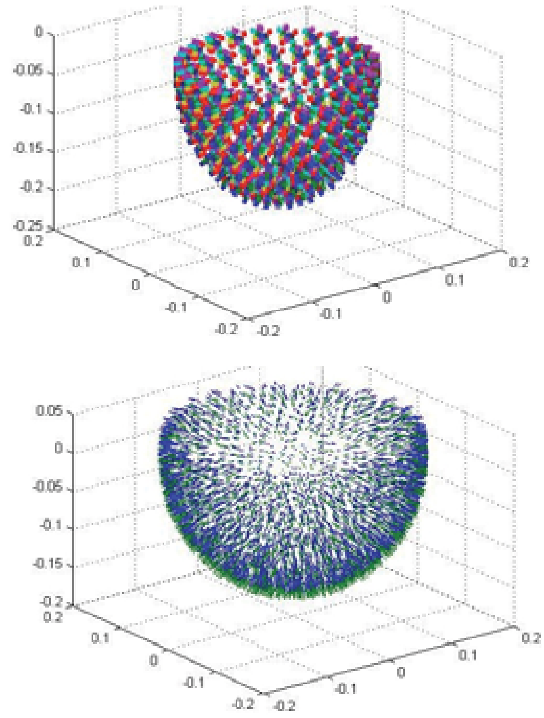

__Fig. 5:__ Comparison of the transducer distribution of the current USCT (top) with 12 aperture positions and the future USCT (bottom) with only two positions, resulting in the same number of A-scans (10^7).

6 Conclusion

We developed an optimized unfocused 3D USCT with approximately isotropic 3D PSF in a breast shaped ROI and presented first patient data which demonstrate the performance of the system. We realized a sparse 3D USCT setup, which implements an optimized transducer distribution, resulting in homogeneous illumination, and nearly isotropic 3D PSF.

Results of a first pilot study with the KIT 3D USCT with ten patients have been presented. The aims of the pilot study could be fully reached: Ten patients were successfully imaged with the 3D USCT. The process and protocols of the data acquisition could be evaluated. The image reconstruction and image fusion could be tested.

All these steps where successful and their results will lead to further optimization of the system.

First patient images show promising results. It seems that speed of sound is at the current state the most indicating modality for cancer. Yet, this needs further evaluation and also more complex reconstruction methods have to be tested.

Literature

[1] *Schomberg, H.: An improved approach to reconstructive ultrasound tomography. In J. Phys. D: Appl. Phys. 11, 1978.*

[2] *Duric, N.; Littrup, P.; et al.: In-vivo imaging results with ultrasound tomography: Report on an ongoing study at the Karmanos Cancer Institute. In Proc. SPIE Med. Imag., 2010.*

[3] *Wiskin, J.; Borup, D.; et al.: Inverse scattering and refraction corrected reflection for breast cancer imaging. In Proc. SPIE Med. Imag., 2010.*

[4] *Schwarzenberg, G.; Zapf, M; et al.: Aperture optimization for 3D ultrasound computer tomography." In Proc. IEEE UFFC Symp, 2007.*

[5] *Norton, S.; Linzer, M.: Ultrasonic reflectivity imaging in three dimensions: Reconstruction with a spherical array. In Ultrasonic Imaging 1, 1979.*

[6] *Kretzek, E.; Dapp, R.; et al.: Evaluation of phase aberration correction for a 3D USCT. InProc. IEEE UFFC Symp, 2013.*

[7] *Ruiter, N.V.; Schwarzenberg, G.F.; et al.: Improvement of 3D ultrasound computer tomography images by signal pre-processing. In Proc. IEEE UFFC Symp., 2008.*

[8] *Kretzek, E.; Zapf, M.; et al.: GPU based acceleration of 3D USCT image reconstruction with efficient integration into MATLAB. In Proc. SPIE Med. Imag., 2013.*

[9] *Dapp, R.; Ruiter, N.V.; et al.: Geometry independent speed of sound reconstruction for 3D USCT using apriori information. In Proc IEEE IUS, 2011.*

[10] *Ranger B.; Littrup P.J.; et al: Breast ultrasound tomography versus magnetic resonance imaging for clinical display of anatomy and tumor rendering: Preliminary results. AJR American journal of roentgenology. 2012;198(1).*

[11] *Hopp, T; Dapp, R.; et al.: Registration of 3D ultrasound computer tomography and MRI for evaluation of tissue correspondences. In Proc SPIE Medical Imaging 2015,.*

[12] *Dapp, R.: Abbildungsmethoden für die Brust mit einem 3D-Ultraschall-Computertomographen, PhD thesis, KIT, 2014.*

[13] *Ruiter, N.V; Zapf, M.; et al.: Optimization of the aperture and the transducer characteristics of a 3D Ultrasound Computer Tomography System. In SPIE Med. Imag., 2014.*

Material-integrated Intelligent Systems – Notes on State of the Art and Current Trends

Lehmhus, D.

ISIS Sensorial Materials Scientific Centre, University of Bremen, Bremen

Abstract

The present text provides an overview of so-called material-integrated intelligent systems. Following an explanation of the concept behind this term, specific challenges associated with this approach are named and technological solutions and research paths highlighted that are aimed at tackling them. In doing so, both hard- and software aspects are considered. In a conclusion, an attempt is made to identify specific issues that from the author's point of view for one thing require additional research efforts and besides should generally move further into the focus of the scientific community dealing with this kind of systems. Among these is the topic of data evaluation, the emphasis on which once again stresses the multi-disciplinary nature of material-integrated intelligent systems.

1 Introduction

Material-integrated intelligent systems represent a concept that includes, but extends beyond material-integrated sensors. To explain this notion, tactile sensing has often and successfully been referred to: Our own tactile experience can be shown to be composed of several different sensory contributions fused together by local data pre-processing, including signals related to temperature, pressure as well as the latter's first and second derivative. Thus if tactile sensing, and the skin and associated nervous system that it is based on, are conceived as model of material-integrated intelligent systems, this implies that in its technical counterpart, besides sensors, signal and data processing and evaluation must also become an integral part of the material, and to make use of information gathered, communication capabilities on an internal, material level and towards external system components are mandatory. Finally, since materials integration limits access to the embedded system, energy autonomy is more than useful and has to be guaranteed through scenario-dependent combinations of energy harvesting and storage, accompanied by an intelligent management of resources which includes the consumer side in its considerations by measures such as context-dependent depth of data evaluation, saving energy through accepting cutbacks in accuracy and reliability of results where safety is not at stake. Summing up, what constitutes a material-integrated intelligent system is a move of functionality into the material which basically has its end when a complete energy-autonomous intelligent sensor network is incorporated in a host material which in turn may be processed into different kinds of products just like any semi-finished material. The appeal of the latter aspect lies in the assumption that such flexibility in application may help to lower cost of material-integrated intelligent system through economy of scale effects.

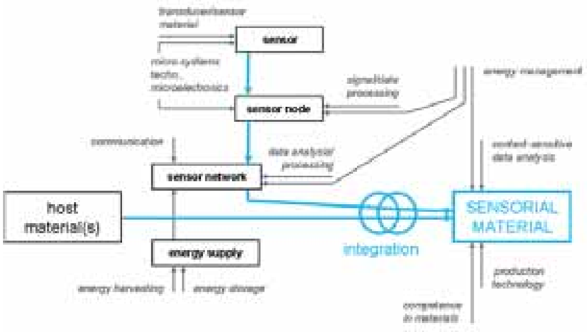

Fig. 1: *Components of a "sensorial material" [2].*

Systems of this kind (see Fig. 1) have been discussed repeatedly in the literature: "Sensorial materials" as described by Lang et al. and Lehmhus et al. are among the examples [1-3]. Mekid et al. have addressed this concept again lately [4, 5], while a recent study by McEvoy and Correll explicitly points at the potential of adding actuator functionalities, coining the term "robotic material" for the concept thus suggested [6]. For increased ease of formulation, in the following text, the term "sensorial materials" will be used synonymously with material-integrated intelligent systems.

Even though a full-fledged realization of sensorial materials is not in commercial use today, it is not hard to envisage future areas of application:

These include robotics, where the tactile sensing originally employed to outline the concept is one of the aims addressed in “smart skin”-related research [7], structural health monitoring and control in civil [8] or aerospace engineering [9], up to autonomous “fly-by-feel” concepts in the latter field [10]. Still less prominent, but potentially more disruptive ideas include new kinds of (tangible) user interfaces for all sorts of consumer products from everyday objects all the way up to future generation automotive user interfaces [11].

2 Challenges: Overview

The main challenges sensorial materials face can be derived from the observation that integration must not have adverse effects on the systems primary functions. Similarly, the added functionality must live up to the product’s fundamental levels of quality, reliability, lifetime etc.

In short, requirements include

- no adverse effect of integration on the host material’s or the system’s own performance,
- fault- and damage-tolerance, incl. self-evaluation capability,
- reliability in signal- and data processing,
- long-term stability under service conditions,
- energy autonomy,
- low to no maintenance requirements and
- finally, competitive costs.

Fig. 2 summarizes this list by grouping and further detailing the aforementioned aspects.

Fig. 2: *Sensorial materials main challenge.*

In the following text, selected challenges will be discussed in more detail. The focus is first on mechanical and thermal stability and compatibility, followed by issues of data processing.

3 Mechanical and thermal stability and compatibility

Intelligent systems to be integrated in the volume of a host material need to withstand loads associated with the production process and the receiving component’s service life.

Production processes differ greatly in terms of the thermal and mechanical loads they exert. Light metal casting is typically done above 700°C, with pressure levels in high pressure die casting (HPDC) easily exceeding 1000 bar. In contrast, conditions in polymer processing are mild: In plastic injection moulding, temperatures usually remain below 300°C, while injection and packing pressure fall short of 1000 bar (Fig. 3).

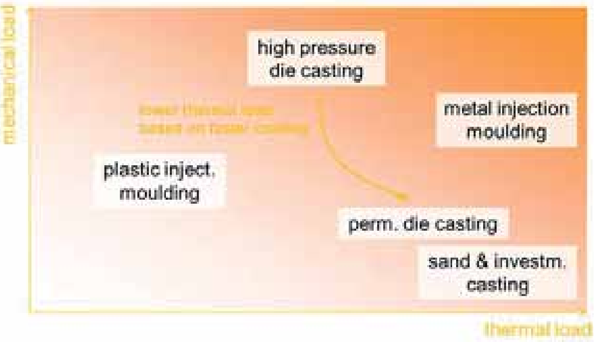

Fig. 3: *A rough, qualitative comparison of host material processing conditions’ severity.*

A distinction has to be made here between mechanical stability and compatibility: The former describes the capability to sustain loads without damage, while evaluation of the latter addresses the combined performance of host material and embedded system: Thus the main problem with compatibility is that materials required for their functional properties usually differ greatly from the host materials in terms of their mechanical and thermal characteristics. Besides, the complex built-up of microsystems usually necessitates stacking several layers of different functional materials, with significant implications for local stress levels under a simple global load: Dumstorff et al. have demonstrated this on a generic level using FEM simulation techniques to demonstrate stress level concentrations in and around a silicon microchip embedded in theoretical materials characterized by Young’s moduli in ranges below and above that of silicon, with the structure as a whole under tensile and bending load [12]. Lecavelliers des Etangs-Lavellois et al. have looked at the same problem in even more detail, down to the level of the aforementioned individual functional layers [13]. In a similar way, shifting a hybrid material or structure made of components with deviating coefficients of thermal expansion (CTE) to temperatures beyond an assumed, stress-free ground state will introduce mechanical stress within such systems: If a low CTE material is embedded in a high CTE one, it will suffer tensile stresses when heated, and vice versa. For polymer-embedded microsystems, Heber et al. have discussed such effects for a ceramic, PZT-type piezoelectric in a PA6 and PEEK matrix, respectively [14].

Basically, three generic concepts are used to obtain mechanical stability and/or compatibility, on slightly different levels (see Fig. 4).

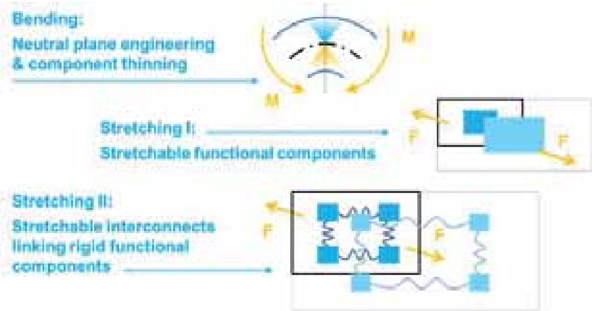

Fig. 4: *Potential paths towards stability and compatibility: Flexible, bendable and stretchable components.*

Neutral Plane Engineering makes use of the fact that the central layer of a planar structure, when bent around an axis in the plane, experiences neither strain nor stress. Since the theoretical thickness of this central layer is zero, components that need to exploit the effect to the full need to be extremely thin themselves. Considered individually, the thinner a structure is, the lower is the maximum strain it experiences when bent to a given radius - as a rule of thumb, a ratio of 1:1000 is observed between thickness and tolerable radius of curvature, though the exact value depends on Young's modulus and yield strength of the material in question, too, as both together govern the limits of purely elastic deformation [15]. In practice, what seems an attractive bypass w.r.t. many problems of material integration, has a number of pitfalls to offer: First of all, infinitely low thickness is not really achievable, the more so if several functionalities and thus subcomponents together with their wiring are the subject of the attempted planar integration: For compactness, most SiF concepts are multi-layer themselves, with alternating functional and wiring layers, thus constituting a system being indeed thin, but for sure not infinitely so. Besides, real-world sheet metal structures are likely to see loads that differ from the simple case – as already Dumstorff et al. have shown, naturally, in-plane tensile stress cancels out the concept's benefits [12]. Finally, for some part of the intelligent sensor system, namely the sensor itself, a stress-free state is not what is aimed at, at least if it is mechanical loads that are to be detected.

Stretchable functional components, in contrast, are for most host materials a solution that comes at a cost – that is, the cost of computing power. Non-silicon sensors and electronic devices can be based on a number of organic substances, like PEDOT-PSS or pentacene. As organic materials, they show both Young's moduli and CTEs that better match polymer substrates or host materials. At the same time, they tend to be well suited for large-area, low cost manufacturing processes – which is why the terms organic and printed electronics are sometimes used almost synonymously -, and thus show promise in view of the economic aspects of sensorial materials. However, they fall short of silicon electronics' performance by several orders of magnitude, first, because the achievable integration density on an area basis is lower by a fact of roughly 10^6, secondly, because switching times similarly fail to reach those of their inorganic counterparts. Nevertheless, organic electronics will likely prove to be of interest for low cost applications, or for clearly defined data processing subtasks e.g. in sensorial material concepts based on SiF-like configurations. Table 1 below outlines the main differences in overall profile between organic and inorganic electronics.

Table 1: *Organic vs. inorganic electronics.*

feature	***org./printed electronics***	***Si/convent. electronics***
switching times	--	++
integration density	--	++
large area solution	++	--
flexibility	++	- (UTCP)
ease of fabrication	++	--*
fabrication costs	++	--*

* True for cost-of-area perspective, different for performance-related cost.

Stretchable interconnects are a reasonable way of maintaining many of the advantages that go with stretchability in general, but still keep sensor and electronics performance. Functional components are allowed to be stiff, almost rigid, in this case, while the interconnects between them are designed in a conformable manner, through choice of materials, and/or adapted geometries.

Lang et al. have recently reviewed several ways of achieving stretchability of interconnects [16]. Meander shapes in the substrate plane are the most common solution. Recent optimization attempts have addressed the reduction of local stresses in the conductive path at a given strain of substrate and interconnect, leading to a horse-shoe geometry [17]. However, structures of this kind were shown to experience stresses perpendicular to the substrate, too, which depend in their magnitude on the aspect ratio between path width (in-plane) and thickness (out-of-plane). To reduce the effect, use of several parallel paths, each of a more favourable aspect ratio, has been suggested [17]. An interesting alternative, though somewhat harder to realize on larger area, makes direct use of CTE mismatches: Here, a metallic conductive layer is deposited on a polymer at temperatures raised above the operating range. When cooling to the latter, the higher CTE of the polymer induces compressive stresses in the thin metal layer, which folds into a complex relief pattern, but due to its low thickness, does not fail. In-plane stretching of substrate and metal layer will flatten out the pattern [18]. A comparable approach uses mechanical pre-stretching of the substrate [19]. Both studies report notable strain levels of 3.8 and even 22%, respectively, without loss of conductivity and with the added benefit of allowing biaxial stretching.

Typically, systems that have stretchability designed into them also build on thinned components to limit rigidity to in-plane loads. Ultra Thin Chip Packaging (UTCP) and Ultimate Thinning and Transfer Bonding (UTTB) are processing sequences that reduce microchip thickness to levels of a few micrometers through sequential mechanical (grinding, lapping) and chemical steps (wet/dry etching) [13]. This is possible because wafer thickness is not controlled by functional requirements, but by the need to allow handling. Thus practically, by reducing material volume to the absolutely necessary, this technique is related to the concept of *Function Scale Integration* proposed by Lang et al. for material-integrated sensors and electronics in general: The message is that the footprint of a material-integrated system may be conceived as wound within the host material, potentially compromising its properties, and should thus be limited in size to the utmost – beyond thickness reduction, this may also mean moving from planar to net-like substrates, so-called functional nets [16]. Related are techniques that do away entirely with the substrate at least for the sensor part of the embedded system. This has been demonstrated by Hufenbach et al. for fibre reinforced composites having thermoplastic matrices: The substrate material carrying the sensor is chosen to match the thermoplastic matrix, thus during processing, the interfaces between both system components disappear [20].

4 Data processing challenges

Data processing and information retrieval represents a major, distinguishing feature of sensorial materials as defined here, because in classical sensor-equipped structures, though the tasks are there, they are very often realized in a centralized manner, and handled outside the material or structure itself. This notion is explicitly reflected in several concepts for aerospace SHM systems, which are designed to gather data in flight and pass it on to ground control for finding some sense in the sum of the signals sent [21].

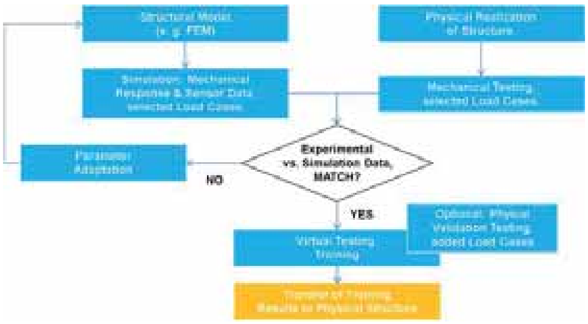

Fig. 5: *Example of the fundamental structure of an SHM data evaluation system employing machine learning techniques.*

In contrast, if an SHM system is to provide safety at runtime, among others, it needs true real-time capabilities: In case of damage, the evaluation of its consequences and of protective measures to take must be at hand immediately after its occurrence. But this is not all that is to be wished for: An additional, but very important aspect among the data evaluation topoi is nicely illustrated by a robotic system, developed at Cornell University, which is programmed to autonomously identify its own configuration and independently develop strategies to achieve certain goals, like “walk a distance” without any previous instruction about how to actually perform the act of walking. Besides this learning capacity, the system is able to detect changes of state, which could e. g. be damage, and adapt its internal self-model accordingly [22].

The link between this starfish robot and the aforementioned SHM system is the fact that one has, the other desperately needs a system identification capability: Being damaged, the SHM-supported structure must not only be able to analyze what happened, but beyond this, it needs to retain its self-evaluating and predictive capabilities in its new state – or at least it must realize that it has actually lost them, if damage is too severe.

Practical approaches towards self-evaluating and fast data processing have e.g. been discussed by Lehmhus et al., Bosse and Lechleiter and Bosse [23-25]: Bosse and Lechleiter present hybrid data evaluation concepts that combine machine learning and multi-agent based systems as examples of Artificial Intelligence (AI) methodologies with inverse FEM methods for fast, but basically static, identification and reconstruction of loads acting on the monitored structure to start with [24, 25]. In this concept, when triggered by a characteristic signal or event, the role of the software agents is to migrate through the sensor network to detect patterns associated with fault or damage and if required initiate the inverse FEM calculation.

Not yet covered by this procedure are the starfish's capabilities: The inverse methods employed imply a fixed system model. Similarly, machine learning techniques, sometimes designated as model-free, typically base their gathering of knowledge on a static representation of the system. So the question is how a change of system state may be detected and characterized. For the starfish robot, the answer is a subdivision of the system in simplified components (multi-body dynamics) with a set of possible connections: Based on its knowledge of components in the undamaged state, the starfish generates a hypothesis, i.e. a possible system model, and tests it by initiating simple actions (movements) and contrasting the resulting sensor signals with the respective expectations derived from the system model. If assumed and measured values deviate, a new hypothesis is put to the test in exactly the same manner.

In transferring this capability to the sensor-equipped structure, self-evaluation is among the critical issues: What is required is a defined signal. Practically, this could be a typical background signal, a recurring operational state, or a purposefully generated excitation: What this latter option entails is an extension of the sensor network to include active components - actuators. In effect, a system capability like this would lead to a change on software level once hardware is compromised: Nothing, then, is constant but change [2]. Keeping track of such changes, and associating them with an overall safety level that includes soft- and hardware will become a major challenge.

5 Summary, Conclusion and Outlook

The present text could only briefly touch upon certain aspects of material-integrated intelligent systems and cast a spotlight on current development trends in these specific areas. The decision which of these challenges to highlight has been with the author and might be challenged itself. Here, the choice in this respect has been on mechanical and thermal stability and compatibility, and besides these, some specific issues of data evaluation.

In conclusion, the notion is that while many of the more hardware, process and materials engineering-oriented problems still deserve attention, data evaluation is among the areas not to be neglected, with the focus in this respect to be set on real-time capabilities and adaptive methods that allow integration of findings from recurring system identification procedures. Thus the flexibility on the mechanical side exemplified by bend- and stretchability is to be accompanied by a similar flexibility on the software side that accommodates changing system states without compromising safety. Most likely, realization of such capabilities will require actuation in addition to sensing. The actual system state thus becomes more and more fluid: To cope with such effects already during system layout, new development environments as well as simulation and optimization tools are required, not the least providing extensive – and acknowledged - virtual testing facilities. On a grander scale, as further trend, a shift to pervasive and ubiquitous computing including sensor clouds and cloud computing is observed, integrating smart materials and structures in ambient networks, driven e. g. by new advances in multi-agent system technologies [26].

Literature

[1] Lang, W. et al.: Sensorial Materials – A vision about where progress in sensor integration may lead to. Sensors and Actuators A: Physical 171 (2011) 1-2.

[2] *Lehmhus, D. et al.: When nothing is constant but change: Adaptive and sensorial materials and their impact on product design. J. Int. Mat. Sys. and Struct. 24 (2013) 2172-2182.*

[3] *Lehmhus, D.; Bosse, S.; Busse, M.: Sensorial Materials. In: Lehmhus, D.; Busse, M.; Herrmann, A.S.; Kayvantash, K. [Eds.]: Structural Materials and Processes in Transportation. Wiley-VCH, Weinh. 2013.*

[4] *Mekid, S.; Kwon, O. J.: Nervous Materials: A New Approach for better Contriol, Reliability and Safety of Structures. Science of Advanced Materials 1 (2009) 276-285.*

[5] *Mekid, S.; Saheb, N.; Khan, S. M. A.; Qureshi, K. K.: Towards sensor array materials: Can failure be delayed? Science and Technology of Advanced Materials 16 (2015) 034607 (15pp).*

[6] *McEvoy, M. A.; Correll, N.: Materials that combine sensing, actuation, computation and communication. Science 347 (2015) 1261689-1 to -8.*

[7] *Dahiya, R. S. et al.: Directions toward effective utilization of tactile skin: A Review. IEEE Sensors J. 13 (2013) 4121-4138.*

[8] *Stajano, F. et al.: Smart bridges, smart tunnels: Transforming wireless sensor networks from research prototypes into robust engineering infrastructure. Ad Hoc Networks 8 (2010) 872-888.*

[9] *Diamanti, K.; Soutis, C.: Structural health monitoring techniques for aircraft composite structures. Progress in Aerospace Science 46 (2010) 342-352.*

[10] *Salowitz, N.; Chang, F.-K.: Bio-inspired intelligent sensing materials for fly-by-feel autonomous vehicles. IEEE Explore, 2012, doi: 10.1109/ICSENS.2012.6411534.*

[11] *Celentano, A.; Dubois, E.: Metaphors, analogies, symbols: in search of naturalness in tangible user interfaces. Proc. Computer Science 39 (2014) 99-106.*

[12] *Dumstorff, G.; Paul, S.; Lang, W.: Integration without disruption: The basic challenge of sensor integration. IEEE Sensors Journal 14 (2014) 2102-2111.*

[13] *Lecavelliers des Etangs-Lavellois, A. et al.: A converging route towards very high frequency, mechanically flexible, and performance stable integrated electronics. J. of Applied Physics 113 (2013) ID 153701.*

[14] *Heber, T.; Gude, M., Hufenbach, W.: Production process adapted design of thermoplastic-compatible piezoceramic modules. Compos. Part A 59 (2014) 70-77.*

[15] *Wagner, S.; Bauer, S.: Materials for stretchable electronics. MRS Bulletin 37 (2012) 207-213.*

[16] *Lang., W. et al.: From Embedded Sensors to Sensorial Materials – the road to function scale integration. Sensors and Actuators A: Physical 171 (2011) 3-11.*

[17] *Gonzalez, M. et al.: Design of metal interconnects for stretchable electronic circuits. Microel. Rel. 48 (2008) 825-832.*

[18] *Choi, W. M. et al.: Biaxially Stretchable "Wavy" Silicon Nanomem-branes. Nano Letters 7 (2007) 1655-1663.*

[19] *Lacour, S. P.; Wagner, S.; Huang, Z.; Suo, Z.: Stretchable gold conductors on elastomeric substrates. Applied Physics Letters 82 (2003) 2404-2406.*

[20] *Hufenbach, W.; Gude, M.; Heber, T.: Development of novel piezoceramic modules for adaptive thermoplastic composite structures capable for series production. Sens. Act. A156 (2009) 20-27.*

[21] *Meyendorf, N.; Frankenstein, B.; Hentschel, D.; Schubert, L.: Acoustic Techniques for Structural Health Monitoring. IV Conferencia Panamericana de END, Buenos Aires, Brazil, October 2007.*

[22] *Bongard, J.; Zykov, V.; Lipson, H.: Resilient Machines Through Continuous Self-Modeling. Science 314 (2006) 1118-1121.*

[23] *Lehmhus, D. et al.: Simulation techniques for the description of smart structures and sensorial materials. J. of Biol. Physics and Chem. 9 (2009) 143-148.*

[24] *Bosse, S.; Lechleiter, A.: Structural Health and Load Monitoring with Material-embedded Sensor Networks and Self-organizing Multi-Agent Systems. Procedia Technology 15 (2014) 668-690.*

[25] *Bosse, S.: Distributed Agent-based Computing in Material-Embedded Sensor Network Systems with the Agent-on-Chip Architecture. IEEE Sensors Journal 14 (2014) 2159-2170.*

[26] *Bosse, S.: Unified Distributed Computing and Co-ordination in Pervasive/Ubiquitous Networks with Mobile Multi-Agent Systems using a Modular and Portable Agent Code Processing Platform. Proc. Comp. Science 40 (2015), doi:10.1016/j.procs.2015.08.312.*